High-Capacity Multi-Core Fibers for Space-Division Multiplexing

Ye, Feihong; Morioka, Toshio; Peucheret, Christophe

Publication date:
2015

Document Version
Publisher's PDF, also known as Version of record

High-Capacity Multi-Core Fibers for Space-Division Multiplexing

Ph.D. Thesis

Feihong Ye

December 31, 2015

DTU Fotonik
Department of Photonics Engineering

DTU Fotonik
Department of Photonics Engineering
Technical University of Denmark
Ørsteds Plads 343
DK-2800 Kgs. Lyngby
Denmark

Preface

The work presented in this thesis was carried out as part of a Ph.D. project "Ultrahigh-capacity photonic transport beyond Pbit/s" in the period of October 1st, 2012 to December 31st, 2015. The work took place at the Department of Photonics Engineering, Technical University of Denmark and at NTT Device Technology Laboratories, NTT Corporation, Japan (three months external stay).

The Ph.D. project was financially supported by Technical University of Denmark and an EU-Japan coordinated R&D project on "Scalable And Flexible optical Architecture for Reconfigurable Infrastructure (SAFARI)" by the European Commission Horizon 2020 and the Ministry of Internal Affairs and Communications (MIC) of Japan and supervised by:

- Toshio Morioka (main supervisor 10/2012-12/2015), Professor, DTU Fotonik, Technical University of Denmark, Kgs. Lyngby, Denmark
- Christophe Peucheret (co-supervisor 10/2012-09/2013), Professor, FOTON Laboratory (CNRS UMR 6082) - ENSSAT - University of Rennes 1, Lannion, France

Abstract

The transmission capacity of the present optical fiber communication systems based on time-division multiplexing (TDM) and wavelength-division multiplexing (WDM) using single-mode fibers (SMFs) is reaching its limit of around 100 Tbit/s per fiber due to the fiber nonlinearities, fiber fuse phenomenon and the optical amplifier bandwidth. To meet the ever increasing global data traffic growth and to overcome the looming capacity crunch, a new multiplexing technology using new optical fibers is urgently needed. Space-division multiplexing (SDM) is a promising scheme to overcome the capacity limit of the present SMF-based systems. Among the proposed SDM schemes, the one based on uncoupled multi-core fibers (MCFs) having multiple cores in a mutual cladding has proven effective in substantially increasing the transmission capacity per fiber with least system complexity as demonstrated in several state-of-the-art high-capacity transmission experiments beyond Pbit/s.

In order to increase the transmission capacity of MCFs, the total number of cores needs to be increased while keeping the inter-core crosstalk (XT) among neighboring cores low as it degrades the optical signal-to-noise ratio (OSNR) of data signals, limiting the usable modulation formats (i.e., spectral efficiency, hence transmission capacity) and the transmission distance. One of the most powerful and practical XT reduction techniques in an MCF is a trench-assisted (TA) structure, where each core is surrounded by a trench and such MCFs are called trench-assisted MCFs (TA-MCFs). The traditional approach for TA-MCFs design has relied on numerical simulations, which make deriving relationships between XT and fiber structural parameters difficult and non-intuitive. As it is important to be able to understand the effects of various fiber structural parameters on XT performance in designing high-count, low-XT TA-MCFs, an analytical model for XT estimation and XT properties analysis in TA-MCFs has been greatly needed.

In this thesis, a novel analytical model for designing low-XT and high-count homogeneous TA-MCFs is described where all the cores have the same refractive index profiles. Based on the model,

the XT values in TA-MCFs as well as XT properties, including wavelength-dependent XT, XT reduction amount versus trench width, trench depth and XT dependence on core pitch are easily analyzed. It has also been shown that the XT in MCFs depends not only on the fiber structural parameters, but also on the core layout in the fiber cross section. Based on the model, a core layout structure with much lower XT has been found by core positions movement starting from a non closely-packed structure, i.e., one-ring structure (ORS).

In addition to the analytical model for XT in TA-MCFs, backward propagated XT in MCFs for a bidirectional transmission scheme in different cores named "propagation-direction interleaving (PDI)" has been formulated where a new core layout structure that can utilize the XT reduction benefits of PDI is investigated, which turns out to be a square-lattice structure (SLS). Based on the analytical model for XT in TA-MCFs and the XT formulation in PDI, homogeneous square-lattice structured MCFs with a number of cores of 24 and 32 are designed under unidirectional and PDI transmission schemes. As the worst XT in the homogeneous 32-core MCF is higher than the required value of -20 dB over 1000 km for QPSK modulation formats (-30 dB over 100 km for 32QAM), a 32-core fiber with a heterogeneous core arrangement adopting PDI transmission scheme is designed. It is concluded that without adopting PDI, a heterogeneous core arrangement with more than 2 types of non-identical cores which have different refractive index profiles are needed, for instance, 3 or even 4 types of cores.

Finally, a novel XT measurement method in MCF fan-in/fan-out (FI/FO) devices based on Fresnel reflection at the MCF-to-air interface has been studied because the XT of FI/FO devices may limit the performance of MCF transmission systems and hence it is of importance to characterize their XT properties. The new method has great advantages that the MCF-SMF coupling is not needed and the measurements results are immune to the cleaving angle of MCFs. Measurements results based on the conventional MCF-SMF coupling method and the Fresnel reflection method are compared, and it is found that they show very similar statistical properties. The new measurement method provides a robust and simple platform for characterizing XT in MCF FI/FO devices.

Resumé

Tranmissions kapaciteten i de nuværende optiske kommunikations fiber systemer baseret på tidssammenfletning (TDM) og bølgelængde sammenfletning (WDM) i single-mode fibre (SMF) nærmer sig en begrænsning omkring 100 Tbit/s per fiber. Dette skyldes en kombination af ikke lineære fiber effekter, fibre smeltning samt den begrænsede båndbredden af eksisterende forstærkere. For at imødekomme den til stadighed stigende globale trafik stigning og dermed undgå et kapacitets nedbrud, er en ny sammenfletnings teknologi som benytter nye typer optiske fibre meget presserende. Rummelig sammenfletning (SDM) er et lovende princip der kan overvinde kapacitetsbegrænsningerne i de eksisterende SMF baserede systemer. Blandt foreslåde SDM teknikker har teknikken baseret på ikke koblede flerkerne fibre (MCF) med en fælles delt kappe vist sig at være effektiv til at øge den samlede kapacitet betydeligt. Dette er blevet demonstreret i adskillige state-of-the-art Pbit/s højkapacitets transmission eksperimenter.

I bestræbelserne på at øge transmissionskapaciteten over MCF skal det samlede antal kerner øges samtidigt med at kerne krydstale (XT) mellem nabo kerner er tilstrækkelig lav til at det optiske signal støj forhold (OSNR) ikke forringes og dermed begrænser valg af modulationsformat (og dermed spektral effektivitet og dermed transmissions kapacitet) samt transmissionsafstand. En af de mest effektfulde og praktiske teknikker egnet til at mindske XT i en MCF er en rende-assisteret struktur, hvor hver enkelt kerne er omgivet af en rende. Disse MCF er benævnt rende assisterede MCF (TA-MCF). Den typiske tilgang til TA-MCF design er baseret på numeriske simuleringer, hvilket gør udledning af sammenhænge mellem XT og strukturelle fiber parametre vanskelig og ikke intuitiv forståelig. Da det er vigtigt at forstå indflydelsen af forskellige strukturelle fiber parametre på XT når der skal designes TA-MCF med højt antal kerne samt lavt XT, er en analytisk model til at estimere XT samt XT egenskaber af stor vigtighed.

I denne afhandling bliver en ny analytisk model beskrevet, som benyttes til at designe lav XT samt højt kerne antal TA-MCF. Ved hjælp af denne model er XT værdier let beregnet for TA-MCF

såvel som XT egenskaber herunder bølgelngde afhængig XT, XT afhængighed af rende bredde samt kerne afstand. Det er yderligere blevet vist at XT i MCF afhænger ikke kun af de strukturelle parametre af fiberen, men også af kerne layout i fiberens tværsnit areal. Med udgangspunkt i denne model er kernernes position blevet optimeret således at XT er reduceret i TA-MCF.

Sammenholdt med den analytiske model for XT i TA-MCF er modsat udbredt XT i MCF ved samtidig fremad og baglæns transmission benævnt "udbredelses retnings sammenfletning (PDI)" blevet beskrevet. En ny kerne layout struktur som udnytter XT reduktion ved PDI er blevet undersøgt. Dette layout viser sig at være en firkantet gitter struktur. Baseret på den analytiske XT model i TA-MCF kombineret med XT udtryk for PDI, er en homogen firkantet gitter struktur baseret MCF med 24 og 32 kerner blevet designet for både envejs udbredelse samt PDI transmission. Idet den værste XT værdi i den homogene 32 kerne MCF er højere end den anbefalede værdi på -20 dB over 1000 km for QPSK modulation, er et 32 kerne heterogent kerne arrangement som udnytter PDI blevet designet. Det bliver konkluderet at uden udnyttelse af PDI er heterogen kerne arrangement med mere end 2 forskellige typer kerner nødvendig, f.eks. 3 eller endda 4 forskellige typer kerner.

Til sidst bliver en nyudviklet XT måleteknik baseret på Fresnel refleksion fra MCF til luft interface indkobling udkobling (FI/FO) enhed undersøgt idet XT fra FI/FO enheder begrænser ydeevnen af MCF transmissions systemer hvorfor det er særdeles vigtigt at kunne karakteriserer disses XT egenskaber. Den nye tekniks store fordel er at MCF-SMF kobling ikke er nødvendig samt at måle resultaterne er immune overfor kløvningsvinklen af MCF. Målinger baseret på normal MCF-SMF kobling er sammenlignet med Fresnel refleksionsteknikken og det er fundet at de har sammenlige statiske egenskaber. Den nye måleteknik stiller således en robust og simpel platform til karakterisering af XT i MCF FI/FO enheder til rådighed.

Acknowledgements

First of all, I would like to express my sincere gratitude to my supervisors, Professor Toshio Morioka and Professor Christophe Peucheret, for giving me such a great opportunity to explore the world of "space-division multiplexing" in optical communications. They are always very kind and extremely supportive when I encounter any difficulties in research and personal life. Without Professor Morioka's strong connection to the research community in Japan, collaborations with leading institutions like NTT, Fujikura Ltd. and Hokkaido University would never have been possible and so fruitful. With his recommendation and support, I was able to spend three months at NTT Device Technology Laboratories, Atsugi, Japan, for my external research stay, which has been very successful and enjoyable.

I would like to thank our industrial collaborators, Takayuki Mizuno, Hidehiko Takara and Yutaka Miyamoto, NTT Network Innovation Laboratories, NTT Corporation, Japan, for their continuous support and guidance. I would also like to thank Hirotaka Ono, NTT Device Technology Laboratories, and Yoshiteru Abe, NTT Device Innovation Center, NTT Corporation, Japan. My research stay at their labs would not have been so fruitful without their excellent supervision and generous support.

I would like to thank Professor Kunimasa Saitoh, Graduate School of Information Science and Technology, Hokkaido University, Japan, for his kind guidance and continuous support. My journey to the analytical model of trench-assisted multi-core fibers would not have been possible without the collaborations with his group, especially the insightful discussions with his former Ph.D. student, Jiajing Tu, who is now with the Research Center for Convergence Networks and Ubiquitous Services, University of Science & Technology Beijing, China.

I would also like to thank our industrial collaborators, Katsuhiro Takenaga and Shoichiro Matsuo, Advanced Technology Laboratory, Fujikura Ltd., Japan, for their support and guidance.

I would like to show my appreciation to the funding agencies in Denmark, Oticon Fonden and

Otto Mønsteds Fond, for their generous financial support for providing travel grants to the international conference attendance and overseas research external stay. I would also like to thank the EU-Japan coordinated R&D project on "Scalable And Flexible optical Architecture for Reconfigurable Infrastructure (SAFARI)" by the European Commission Horizon 2020 and the Ministry of Internal Affairs and Communications (MIC) of Japan for partially supporting this work.

Last but not the least, I would like to thank all my office-mates Deming Kong, Valerija Kamchevska, Francesco Da Ros, Dragana Vukovic, Asger Sellerup Jensen and my colleagues Ashenafi Kiros Medhin, Pengyu Guan, Jason Jia, Rameez Asif, just to name a few, in High-Speed Optical Communications group for their support and useful discussions over countless coffee breaks and foosball (also called "table football") at DTU Fotonik.

Feihong YE

Kgs. Lyngby, December, 2015

Ph.D. Publications

The following publications have resulted from this Ph.D. project.

Articles in international peer-reviewed journals: (6)

[J1] Feihong Ye, Y. Tobita, K. Saitoh, K. Takenaga, S. Matsuo, and T. Morioka, "High-Count Multi-Core Fibers with Multiple Crosstalk Reduction Techniques," *(to be submitted to) IEEE Photonics Technology Letters*, 2016.

[J2] Feihong Ye, J. Tu, K. Saitoh, K. Takenaga, S. Matsuo, and T. Morioka, "Analytical Model for Homogeneous Trench-Assisted Multi-Core Fibers," *(to be submitted to) Journal of Lightwave Technology*, 2016.

[J3] Feihong Ye, H. Ono, Y. Abe, M. Yamada, and T. Morioka, "Novel Crosstalk Measurement Method for Multi-Core Fiber Fan-In/Fan-Out Devices," *(submitted to) IEEE Photonics Technology Letters*, 2016.

[J4] Feihong Ye, J. Tu, K. Saitoh, K. Takenaga, S. Matsuo, H. Takara, and T. Morioka, "Wavelength-dependence of Inter-core Crosstalk in Homogeneous Multi-Core Fibers," *IEEE Photonics Technology Letters*, vol. 28, no. 1, pp. 27–30, Jan. 2016.

[J5] Feihong Ye, J. Tu, K. Saitoh, and T. Morioka, "Simple Analytical Expression for Crosstalk Estimation in Homogeneous Trench-Assisted Multi-Core Fibers," *Optics Express*, vol. 22, no. 19, pp. 23 007–23 018, Sept. 2014.

[J6] Yunhong Ding, Feihong Ye, C. Peucheret, H. Ou, Y. Miyamoto, and T. Morioka, "On-chip Grating Coupler Array on the SOI Platform for Fan-In/Fan-Out of MCFs with Low Insertion Loss and Crosstalk," *Optics Express*, vol. 23, no. 3, pp. 3292–3298, Feb. 2015.

Contributions to international peer-reviewed conferences: (20)

[C1] H. Hu, R. Asif, Feihong Ye, , S. Gross, M. Withford, T. Morioka, and L. K. Oxenløwe, "Bidirectional 120 Gbps SDM-WDM-PON with Colourless ONU using 10 Gbps Optical Components without DSP," in *(to be presented at) Optical Fiber Communication Conference (OFC)*, Anaheim, California, USA, March 2016.

[C2] V. Kamchevska, A. K. Medhin, F. D. Ros, Feihong Ye, R. Asif, A. M. Fagertun, S. R. Ruepp, M. S. Berger, L. Dittmann, T. Morioka, L. K. Oxenløwe, and M. Galili, "Experimental Demonstration of Multidimensional Switching Nodes for All-Optical Data Centre Networks," in *41st European Conference and Exhibition on Optical Communications (ECOC)*, Valencia, Spain, Sept. 2015, paper Tu.1.2.2.

[C3] R. Asif, H. Hu, P. Mitchell, J. Macdonald, F. D. Ros, N. Psaila, Feihong Ye, L. Potì, L. K. Oxenløwe, and T. Morioka, "Experimental Demonstration of 6-Mode Division Multiplexed NG-PON2: Cost Effective 40 Gbit/s/Spatial-Mode Access Based on 3D Laser Inscribed Photonic Lanterns," in *41st European Conference and Exhibition on Optical Communications (ECOC)*, Valencia, Spain, Sept. 2015, paper Tu.1.5.1.

[C4] R. Asif, M. Imran, Feihong Ye, L. Potì, and T. Morioka, "NG-PON2 Architecture Enabled by Heterogeneous Space Division Multiplexing with Distributed Light Source: A Proof-of-Concept Evaluation," in *Photonics in Switching (PS)*, Florence, Italy, June 2015, paper ThII1.

[C5] A. Clausen, H. Hu, Feihong Ye, A. K. Medhin, Y. Ding, R. Asif, M. Galili, T. Morioka, and L. K. Oxenløwe, "Increase in Data Capacity utilising Dimensions of Wavelength, Space, Time, Polarisation and Multilevel Modulation using a Single Laser," in *17th International Conference on Transparent Optical Networks (ICTON)*, Budapest, Hungary, July 2015, paper Th.A1.1.

[C6] R. Asif, M. Imran, Feihong Ye, L. Poti, and T. Morioka, "Spatially and Spectrally Flexible Next-Generation Elastic Bi-directional SDM-WDM-PON with Dynamic Unicast/Multicast Overlay Data," in *Northern Optics and Photonics*, Lappeenranta, Finland, June 2015, paper Wed.8a.

[C7] R. Asif, Feihong Ye, and T. Morioka, "Equalizer Complexity for 6-LP Mode 112 Gbit/s m-ary DP-QAM Space Division Multiplexed Transmission in Strongly Coupled Few-Mode-Fibers,"

in *European Conference on Networks and Communications*, Paris, France, June 2015, paper OPN01.1.

[C8] ——, "Lambda-Selection Strategy in C+L Band 1-Pbit/s (448 WDM/19-Core/128 Gbit/s/channel) Flex-Grid Space Division Multiplexed Transmission," in *European Conference on Networks and Communications*, Paris, France, June 2015, paper OPN01.2.

[C9] R. Asif, M. Imran, Feihong Ye, L. Poti, and T. Morioka, "Flexible Space Division Multiplexed WDM-PON with 16-QAM Point-to-Point and PolSK Modulated Multicast Overlay Services," in *European Conference on Lasers and Electro-Optics (CLEO/Europe)*, Munich, Germany, June 2015, paper CI.P.10.

[C10] Feihong Ye, K. Saitoh, H. Takara, R. Asif, and T. Morioka, "High-count Multi-Core Fibers for Space-Division Multiplexing with Propagation-Direction Interleaving," in *Optical Fiber Communication Conference (OFC)*, LA, California, USA, March 2015, paper Th4C.3.

[C11] **[Postdeadline]** Hao Hu, Feihong Ye, A. K. Medhin, P. Guan, H. Takara, Y. Miyamoto, H. C. H. Mulvad, M. Galili, T. Morioka, and L. K. Oxenløwe, "Single Source 5-dimensional (Space-, Wavelength-, Time-, Polarization-, Quadrature-) 43 Tbit/s Data Transmission of 6 SDM $\times$ 6 WDM $\times$ 1.2 Tbit/s Nyquist-OTDM-PDM-QPSK," in *Conference on Lasers and Electro-Optics (CLEO)*, San Jose, California, USA, June 2014, paper JTh4B.10.

[C12] **[Postdeadline]** Hao Hu, A. K. Medhin, Feihong Ye, Y. Ding, R. Asif, P. Guan, H. Takara, Y. Miyamoto, H. C. H. Mulvad, M. Galili, T. Morioka, and L. K. Oxenløwe, "1.28 Tbaud Nyquist-OTDM Transmission over a 7-Core Fiber Using an On-Chip SDM Coupler," in *OptoElectronics and Communications Conference and Australian Conference on Optical Fibre Technology (OECC/ACOFT)*, Melbourne, Australia, July 2014, paper THPDP2-2.

[C13] Yunhong Ding, Feihong Ye, C. Peucheret, H. Ou, Y. Miyamoto, and T. Morioka, "On-chip Grating Coupler Array on the SOI Platform for Fan-In/Fan-Out of Multi-Core Fibers with Low Insertion Loss and Crosstalk," in *40th European Conference and Exhibition on Optical Communications (ECOC)*, Cannes, France, Sept. 2014, paper We.1.1.3.

[C14] Rameez Asif, Feihong Ye, and T. Morioka, "Phase Conjugated Twin Waves in $8 \times 21 \times 224$ Gbit/s DP-16QAM Multi-Core Fiber Transmission," in *Asia Communications and Photonics Conference (ACP)*, Shanghai, China, Nov. 2014, paper AF1F.5.

[C15] ——, "Dynamics of 1.12 Tbit/s WDM Flex-Coherent Super-Channels in Multi-Core Fiber Transmission," in *Asia Communications and Photonics Conference (ACP)*, Shanghai, China, Nov. 2014, paper AF1F.2.

[C16] Feihong Ye, J. Tu, K. Saitoh, and T. Morioka, "Theoretical Investigation of Inter-core Crosstalk Properties in Homogeneous Trench-Assisted Multi-Core Fibers," in *IEEE Photonics Society Summer Topicals Meeting Series*, Montreal, Canada, July 2014, paper TuE4.2.

[C17] Feihong Ye, J. Tu, K. Saitoh, K. Takenaga, S. Matsuo, and T. Morioka, "A New and Simple Method for Crosstalk Estimation in Homogeneous Trench-Assisted Multi-Core Fibers," in *Asia Communications and Photonics Conference (ACP)*, Shanghai, China, Nov. 2014, paper AW4C.3.

[C18] Feihong Ye, J. Tu, K. Saitoh, H. Takara, and T. Morioka, "Wavelength-dependent Crosstalk in Trench-Assisted Multi-Core Fibers," in *OptoElectronics and Communications Conference and Australian Conference on Optical Fibre Technology (OECC/ACOFT)*, Melbourne, Australia, July 2014, paper TU5C-1.

[C19] Feihong Ye and T. Morioka, "Interleaved Core Assignment for Bidirectional Transmission in Multi-Core Fibers," in *39th European Conference and Exhibition on Optical Communications (ECOC)*, London, UK, Sept. 2013, paper We.2.D.5.

[C20] Feihong Ye, C. Peucheret, and T. Morioka, "Capacity of Space-Division Multiplexing with Heterogeneous Multi-Core Fibers," in *18th OptoElectronics and Communications Conference/Photonics in Switching (OECC/PS)*, Kyoto, Japan, July 2013, paper WR2-3.

Awards

- **Best Student Award** at 18th OptoElectronics and Communications Conference/Photonics in Switching (OECC/PS), for "Capacity of Space-Division Multiplexing with Heterogeneous Multi-Core Fibers," paper WR2-3, in Kyoto, Japan, July 2013.

Acronyms

CT	Cladding Thickness
DMD	Differential Mode Delay
DRS	Dual-Ring Structure
DSP	Digital Signal Processing
EDFA	Erbium Doped Fiber Amplifier
FEC	Forward Error Correction
FEM	Finite Element Method
FI/FO	Fan-In/Fan-Out
FMF	Few-Mode Fiber
HCPS	Hexagonal Close-Packed Structure
HOM	Higher-Order Mode
LOM	Lower-Order Mode
MCF	Multi-Core Fiber
MDL	Mode-Dependent Loss
MIMO	Multiple-Input Multiple-Output
MMF	Multi-Mode Fiber
OPS	Optimal Packing Structure
ORS	One-Ring Structure

OSNR Optical Signal-to-Noise-Ratio

PDI Propagation-Direction Interleaving

PDM Polarization-Division Multiplexing

QAM Quadrature Amplitude Modulation

QPSK Quadrature Phase Shift Keying

SDM Space-Division Multiplexing

SE Spectral Efficiency

SI Step-Index

SLS Square-Lattice Structure

SMF Single-Mode Fiber

SNR Signal-to-Noise-Ratio

TA Trench-Assisted

TDM Time-Division Multiplexing

WDM Wavelength-Division Multiplexing

XT Crosstalk

Contents

Chapter 1

Introduction

1.1 Motivation

1.1.1 Global data traffic growth and capacity limit

With the inventions of optical fibers, semiconductor lasers and optical amplifiers, etc., the transmission capacity per fiber has been increased by more than three orders of magnitude over the last two decades, realizing several Tbit/s per fiber transmission systems. With an exponential global Internet traffic growth (40% – 70% per year), demands for high-capacity transport networks have never been so imperative [1]. If this traffic growth continues for the next two decades, the transmission capacity is expected to be increased by three to five orders of magnitude. The current transmission systems are based on different enabling technologies, such as time-division multiplexing (TDM), wavelength-division multiplexing (WDM) and digital coherent technology using digital signal processing (DSP). An overview of capacity growth per fiber over the years is shown in Fig. 1.1, where the previously mentioned different enabling technologies are also indicated. There are five physical dimensions that can be used for multiplexing in order to increase the capacity, which are time, wavelength, polarization, quadrature and space. TDM was used to increase the capacity per wavelength from 100 Mbit/s to 40 Gbit/s. WDM together with optical amplification then enabled the total capacity to increase beyond 1 Tbit/s. The recently developed DSP-based digital coherent technology has enabled the use of quadrature and polarization dimensions by adopting advanced

modulation formats and polarization-division multiplexing, respectively, achieving 100 Gbit/s per wavelength channel and a total capacity per fiber of nearly 10 Tbit/s and beyond.

The current transmission systems are already using four out of five total available physical dimensions for capacity enhancement, as can be seen from the capacity per fiber trend over the decades. The capacity records of around 100 Tbit/s using a standard single-mode fiber (SMF) [2] and a low loss, low-nonlinear pure silica core fiber [3], both utilizing advanced modulation formats have been reported. The capacity per SMF is ultimately limited by fiber nonlinearities, known as nonlinear Shannon limit [4–7], fiber fuse (fiber core melt-down) [8–10] and the optical amplifier bandwidth. Current optical systems based on SMFs are facing big challenges as they are approaching these fundamental capacity limits.

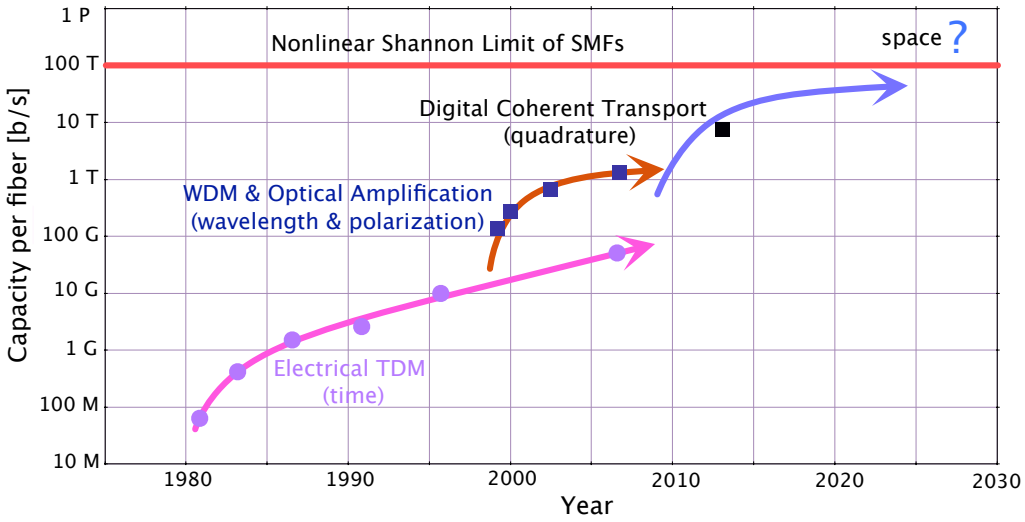

Figure 1.1: Capacity growth per fiber over the decades.

1.1.2 Overcoming capacity crunch by space-division multiplexing

To overcome the capacity limit of SMFs, space-division multiplexing (SDM) has to be used to exploit the last physical dimension, space [11, 12]. Some of the investigated SDM schemes are based on few-mode fibers (FMFs), multi-mode fibers (MMFs) [13–23], coupled multi-core fibers (MCFs) [24–27] and uncoupled MCFs [28–47]. The cross-sectional views of an FMF and an MCF are shown in Fig. 1.2(a) and Fig. 1.2(b), respectively. If the capacity of each spatial channel (either mode in case of MMFs or core in case of MCFs) is assumed to be the same, the aggregate capacity

of SDM systems can be defined as a product of the number of spatial channels and the capacity per spatial channel. Thus, the aggregate capacity of an MCF/MMF is a product of the number of cores/modes and the capacity per core/mode.

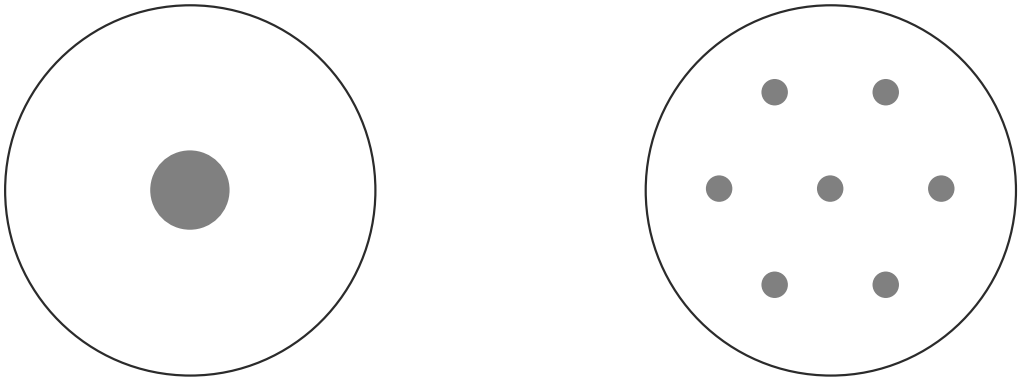

(a) (b)

Figure 1.2: The cross-sectional views of (a) an FMF and (b) an MCF (7-core fiber).

The spectral efficiency (SE) in an SMF is defined as

$$\mathrm{SE} = \log_2(1 + \mathrm{SNR}), \tag{1.1}$$

where SNR is the signal-to-noise ratio [48].

Doubling the SNR only results in an increase of SE by 1 assuming SNR is much larger than 1, and therefore, it is not a very cost effective and energy efficient way for capacity enhancement. Assuming the total power in an MCF is kept the same as in an SMF, the SE in an MCF can then be expressed as

$$\mathrm{SE} = N \log_2(1 + \mathrm{SNR}/N), \tag{1.2}$$

where N is the total number of cores in an MCF.

If the power per core in an MCF is kept the same as in an SMF, the SE in an MCF can be further increased and it is expressed as

$$\mathrm{SE} = N \log_2(1 + \mathrm{SNR}). \tag{1.3}$$

The comparison of SE in an SMF and a 7-core fiber is shown in Fig. 1.3, where the cases for both constant power per core and constant power per fiber are included. As can be seen from the figure, the SE in a 7-core fiber with constant power per fiber is around 5 times the one in an

SMF at single core SNR of 30 dB. By keeping constant power per core in 7-core fiber, the SE in a 7-core fiber can be 7 times as compared to the one in an SMF. Thus, SDM is an effective way for increasing the capacity per fiber. The motivation for adopting MCFs/FMFs instead of SMF bundles are based on the assumption that the future space-division multiplexed transmission systems should be able to adopt energy efficient multi-core (MC)/few-mode (FM) components, such as MC-EDFA/FM-EDFA as well as SDM super-channels for SDM networking and higher-speed interfaces, which potentials are being researched intensively in order to decrease the cost/bit, energy/bit and space/bit.

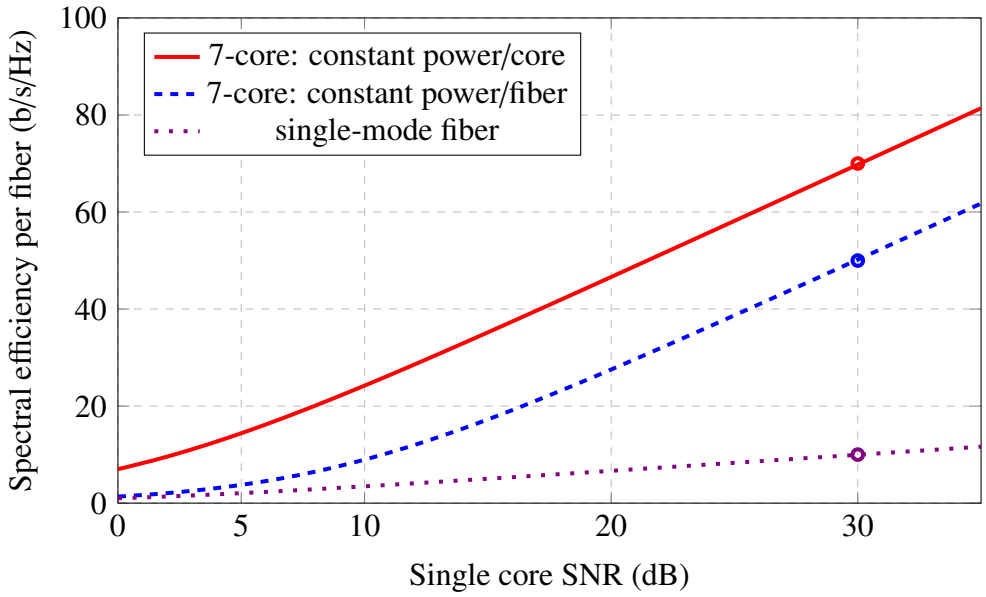

Figure 1.3: Spectral efficiency per fiber as a function of SNR in single-mode fiber and 7-core fiber.

For SDM scheme based on FMFs/MMFs, increasing the number of modes will induce inevitable inter-modal crosstalk due to mode coupling. Therefore multiple-input multiple-output (MIMO) signal processing is generally needed to recover the original signals. The complexity of the spatial distributions of the higher-order modes (HOMs) grows as the number of modes increases. The system memory is a key parameter which determines the complexity of the MIMO receivers, and it is directly related to the maximum differential mode delay (DMD) after transmission [49, 50]. DMD measures the spread of group delays between the fastest and slowest modes. Mode-dependent loss (MDL) is another issue for FMFs/MMFs, where the HOMs suffer higher loss compared to lower-order modes (LOMs). Thus, increasing the number of modes in SDM systems based on

FMFs/MMFs beyond 20 becomes very challenging and unrealistic for practical applications.

Compared to MMFs, SDM based on uncoupled MCFs is a simple and robust option as it does not require any MIMO signal processing at the receiver side. In order to increase the capacity of optical transport systems employing MCFs, it is essential to increase the total number of cores in an MCF within a fixed cross section, which eventually results in a smaller core-to-core distance (or core pitch, Λ). The inter-core crosstalk (XT) in dB of MCFs is inversely proportional to the core pitch and the XT has to be under certain levels as high XT results in serious optical signal-to-noise ratio (OSNR) penalty in optical transmission systems employing advanced modulation formats [51]. Thus, XT reduction methods have to be adopted in order to increase the number of cores in an MCF. The XT reduction techniques can be categorized into two types, the first one being based on strong mode confinement, which results in a smaller mode coupling coefficient between adjacent cores, the second one based on phase mismatching, which results in weaker coupling between adjacent cores.

The highest number of modes and cores in a fabricated FMF/MMF and an MCF are 15 [22] and 31 [52] up to now, respectively. Other demonstrations with hybrid FM-MCFs have also been reported, for instance, a 3-mode 36-core fiber with 108 spatial channels [53] and a 6-mode 19-core fiber with 114 spatial channels [54]. It should be noted that fibers with such high-count spatial channels have been achieved by adopting very large cladding diameters, which are 306 μm and 318 μm for the 3-mode 36-core fiber and the 6-mode 19-core fiber, respectively, as compared to a typical single mode MCF cladding diameter of around 230 μm. The maximum cladding diameter used in this thesis is limited to 225 μm, for the consideration of mechanical reliability issue [33]. Pursuing of ultimate maximum number of spatial channels per fiber is still a hot research topic and the aggregate capacity per fiber should be at least 100 times larger as compared to the current capacity of standard SMFs in order to make SDM systems cost effective and satisfy the capacity requirements for the next decades.

1.2 Contribution of Ph.D. Thesis

In this thesis, we newly developed an analytical model for XT estimations in homogeneous trench-assisted MCFs (TA-MCFs) where we looked into different XT reduction techniques for achieving low-XT and high-count MCFs. The first investigated XT reduction technique utilizes strong mode confinement by a TA structure while the second XT reduction technique is based on phase mis-

matching by propagation-direction interleaving (PDI), where the propagation directions in adjacent cores are opposite to each other for which we formulated the backward propagated XT in MCFs adopting PDI. The accuracy of the proposed analytical model has been validated by comparing with results obtained by the analytical model and numerical simulations. The comparison with experiment measurements of two types of fabricated TA-MCFs has also been made. The analytical model is very powerful, as it is capable of calculating the XT accurately and analyzing the XT properties against various fiber structural parameters in TA-MCFs. The model has also been used to obtain quasi-optimum core layout structure by moving the core positions in non-closely packed structure (i.e. one-ring structure) for XT reduction.

The MCF fan-in/fan-out (FI/FO) devices are essential components in MCF transmission systems as an interface with existing SMF-based devices and it can limit the system performance if its inter-core XT is higher than that in MCF employed in the same fiber link. We investigated a new XT measurement method for MCF FI/FO devices based on Fresnel reflection, which features much less measurement time and robustness as it is immune to the cleaving angle of MCFs. The results obtained by this method are compared with the ones by the traditional MCF-SMF coupling-based method, and they show very similar statistical properties, confirming that the new method provides a powerful tool for simple and fast XT measurements in MCF FI/FO devices.

The works within this Ph.D. project are unique in the sense that we approach the XT estimations based on analytical formulations as compared to the traditional one, which heavily relies on numerical simulations. The development of this analytical model was previously considered to be impossible or at least extremely difficult. The developed model greatly simplifies designing low-XT and high-count TA-MCFs for high-capacity and long-distance transmission.

1.3 Thesis Structure

The rest of this thesis is organized as follows.

Chapter 2 reviews the formulations of XT both under ideal straight condition and realistic bending condition. We then discuss different XT reduction techniques for achieving low-XT in high-count MCFs, which are based on strong mode confinement and phase mismatching. For XT reduction techniques based on strong mode confinement, both hole-assisted/hole-walled structures and TA structures are covered. For XT reduction techniques based on phase mismatching, both heterogeneous core arrangement and PDI are discussed. We also derive an analytical expression

for the backward propagated XT between two adjacent cores, in which the signals propagate in opposite directions.

Chapter 3 presents the development of analytical model for TA-MCFs, where the inter-core XT can be calculated directly without numerical simulations. After the motivation of developing analytical model for XT in TA-MCFs, we formulate the mode coupling coefficient in TA-MCFs by relating it to the one in normal step-index (SI) - MCFs (SI-MCFs). The derived mode coupling coefficient is then related to XT formulation, resulting in an analytical model of XT in TA-MCFs. We compare the XT calculated using the newly developed analytical model with the one obtained by numerical simulations, and we found out they show excellent agreement with each other. We also compare the XT calculated by the analytical model with the one obtained by experiment measurements using two types of fabricated TA-MCFs, and they also exhibit excellent agreement. Based on the analytical model, we then investigate XT properties such as wavelength-dependent XT, XT reduction amount versus trench width, trench depth and XT dependence on core pitch. We also discuss the possibilities and practical limitations for further reduction of XT in TA-MCFs.

Chapter 4 presents XT reduction by moving core positions in a non-closely packed structure. As the XT in MCFs not only depends on fiber structural parameters, such as trench width, trench depth, core radius, but also on the core layout, searching for a better core layout structure is also very important for XT reduction. In this chapter, we demonstrate how we can further reduce the XT in one-ring structure (ORS) by this core position movement. With the use of our analytical model, we demonstrate that dual-ring structure (DRS) is a quasi-optimum core layout structure by moving core positions starting from ORS.

Chapter 5 shows how the analytical model can be used for designing low-XT and high-count MCFs. We first investigate different core layout structures for 12-core fiber, including the ones that have been used in fabricated 12-core fibers and other new core layout structures. We then investigate different core layout structures to fully utilize the XT reduction benefits of PDI. We then conclude that square-lattice structure (SLS) should be used for MCF transmission systems adopting PDI, as it can dramatically reduce the inter-core XT compared to other core layout structures. With the analytical model for XT in TA-MCFs and backward propagated XT in PDI, 24-core and 32-core fibers with SLS are designed both for unidirectional and PDI transmission schemes. In order to achieve MCFs with even lower XT and more than 30 cores per fiber, a heterogeneous TA 32-core fiber with PDI is designed, in which 2 types of non-identical cores are used. We then conclude that if we are restricted to design low-XT and high-count MCFs without adopting PDI, heterogeneous

core arrangements with more than 2 types of cores are needed, i.e., 3 or even 4 types of cores.

Chapter 6 looks into XT measurements of MCF FI/FO devices, as such components are very important in MCF transmission systems. We propose and investigate a novel XT measurement method based on Fresnel reflection at the MCF-to-air interface. In the traditional method, MCF-SMF coupling has always been needed, which is time-consuming and error-prone as perfect coupling is difficult to achieve unless advanced equipment is available. The new method eliminates a need for the MCF-SMF coupling and measurement results are immune to the cleaving angle of MCFs. Measurement results based on the traditional method and Fresnel reflection method are compared, and they show very similar statistical properties. It is thus confirmed that the new measurement method provides a powerful tool for characterizing XT in MCF FI/FO devices.

The last chapter concludes the thesis summarizing the key results achieved in this work and provides a brief outlook for future work.

□ End of chapter.

Chapter 2

Background

2.1 Introduction

To effectively exploit the benefits of SDM for capacity enhancement in future transmission systems employing MCFs, the number of cores in an MCF should be increased dramatically. If the effective area of each core is kept constant, increasing the number of cores within a fixed cross-sectional area results in a smaller core pitch, which leads to higher inter-core XT. As low XT is needed to allow advanced modulation formats to be adopted in SDM transmission systems without significant OSNR performance penalty, it is essential to reduce XT while keeping high core density in MCFs.

In this chapter, we firstly look into the formulation of XT in MCFs, under the ideal straight deployment condition (without fiber bending effects) as well as the realistic fiber bending condition. Based on the XT formulation under bending effects, we then review different XT reduction techniques. There are two main types of XT reduction techniques, which are based on strong mode confinement and phase mismatching. For the mode confinement based techniques, both hole-assisted/hole-walled structures and TA structures have been proposed, where the latter one has been widely used in MCFs adopted in state-of-the-art capacity transmission experiments. For the phase mismatching based techniques, the heterogeneous core arrangement and PDI have been proposed. Here, we also derive the analytical expression for the backward propagated XT by relating it to the forward propagated XT. Finally, we present some examples of MCFs which have already been fabricated and set the XT target to be achieved in this thesis.

2.2 Formulation of XT in MCFs

2.2.1 Definition of XT in MCFs

As the distance between adjacent cores in an MCF is normally very small (i.e. 30 μm to 50 μm) due to the limited cladding diameter and high core density requirement, the mode fields of the adjacent cores inevitably overlap with each other, resulting in non-negligible inter-core XT. The power coupling from core i to core j in an MCF is illustrated in Fig. 2.1, where the dashed arrow represents the power coupling and z is a distance in the signal propagation direction.

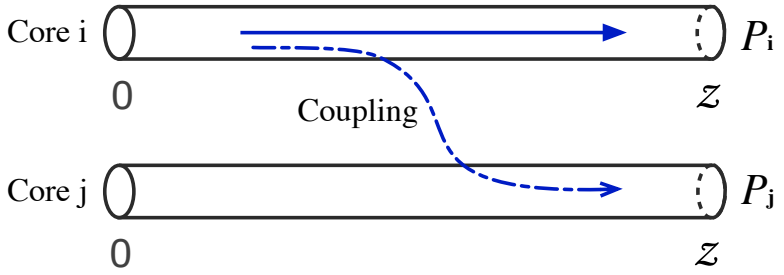

Figure 2.1: Power coupling from one core to an adjacent core in an MCF.

The XT is defined as the ratio of the received power of core j to that of core i at the receiver end. XT can be expressed in logarithm scale as

$$\mathrm{XT} = 10\log_{10}\left(\frac{P_j}{P_i}\right), \tag{2.1}$$

where P_j and P_i are the received powers at core j and core i, respectively.

2.2.2 XT formulation without bending effects

In a co-directional coupler without bending, the optical power flow along the z-direction in core i and core j is given by [55]

$$\begin{cases} P_i(z) = 1 - F\sin^2(qz), \\ P_j(z) = F\sin^2(qz), \end{cases} \tag{2.2}$$

where F denotes the maximum power-coupling efficiency defined by

$$F = \left(\frac{\kappa}{q}\right)^2 = \frac{1}{1 + (\sigma/\kappa)^2}, \tag{2.3}$$

where κ is the mode coupling coefficient between adjacent cores and $\sigma = (\beta_i - \beta_j)/2$ is the difference of the propagation constants between core i and core j, and $q = (\kappa^2 + \sigma^2)^{1/2}$.

In a homogenous MCF, where all the cores have the same refractive index, and thus the mode in each core has the same propagation constant, σ becomes zero, and normalized transmitted and coupled powers in two adjacent cores can be plotted as shown in Fig. 2.2.

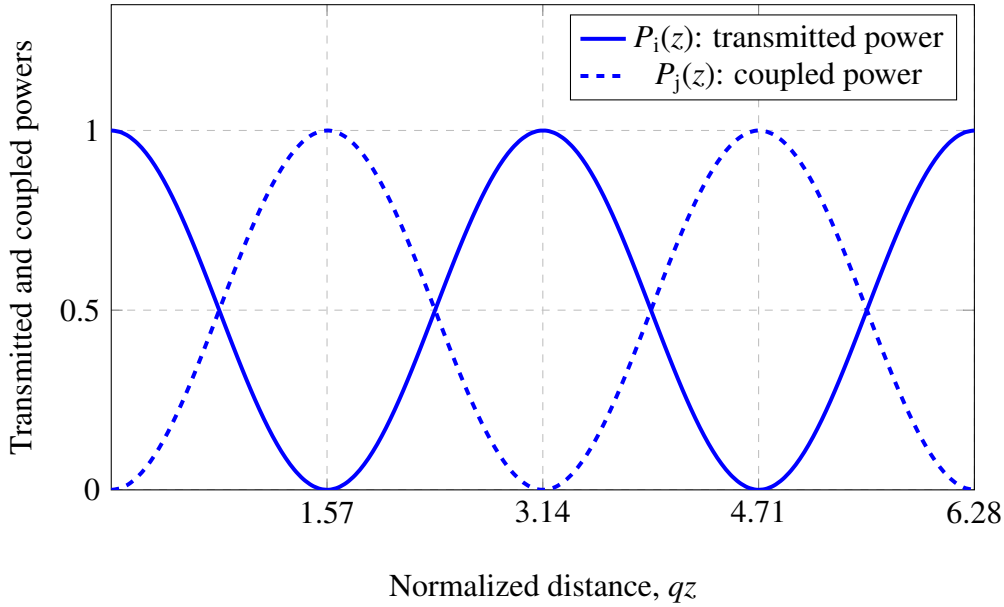

Figure 2.2: Variation of optical powers in a co-directional coupled MCF with $\sigma = 0$ (in other words, $F = 1.0$). Solid lines: transmitted power. Dashed lines: coupled power.

As can be seen from the figure, the coupled power changes periodically between 0 to 1 every half period along the z direction. With the typical fiber parameters such as core radius of 4.5 μm, relative refractive index between core and cladding Δ of 0.35% and core pitch Λ of 50 μm, the fiber length corresponding to an inter-core XT level of -30 dB is around 2 km [28]. Thus, from the XT formulation without bending effects, it can be concluded that homogeneous MCFs are not suitable for high-capacity and long-distance transmissions as the inter-core XT is too high in longer (at least more than 100 km) MCFs with a core pitch of less than 50 μm. In order to reduce the XT, a heterogeneous MCF was proposed [28] where adjacent cores have different refractive indices.

Fig. 2.3 shows transmitted and coupled powers in two adjacent cores in a heterogeneous MCF in the case of $\sigma = 2\kappa$ as an example. As can be seen from the figure, a normalized coupled power is always less than 0.2 and the XT is reduced compared to homogeneous MCFs.

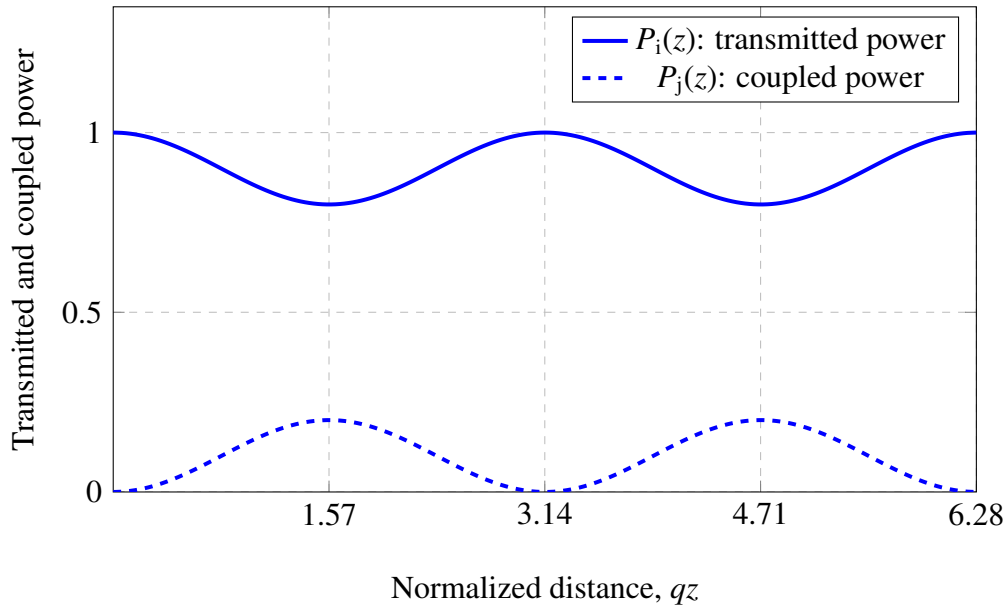

Figure 2.3: Variation of optical powers in a co-directional coupled MCF with $F = 0.2$. Solid lines: transmitted power. Dashed lines: coupled power.

With the typical fiber parameters such as core radius of 4.5 μm, core pitch Λ of 30 μm, Δ_i of 0.35% in non-identical core i and Δ_j of 0.35% ± 0.005% in non-identical core j, the maximum inter-core XT is less than − 30 dB [28]. Thus, heterogeneous core arrangement can significantly reduce the XT in MCFs. It should be noted that the formulation of XT given in this section assumes an MCF under ideal straight conditions, which are not usually met in the deployed fibers suffering from bending effects. Thus, a more accurate model will be described in the next section, taking into account the fiber bending effects.

2.2.3 XT formulation with bending effects

Measured XT in fabricated MCFs exhibited a large discrepancy from the theoretical prediction based on the previous XT model without bending effects. In deployed optical fiber cables, the fibers are not straight but with bending radii ranging from around 100 mm to 1 m, depending on

the cable structure designs such as slotted-core (helical winding) and loose tube structures. The bending is introduced as a result of giving extra length so that there will be no tension applied onto the fibers under real deployment conditions. Thus, MCFs should also be wound on fiber spools with certain diameters for XT measurement and the previous XT formulation without bending effects should not be appropriate in real applications.

Taking the fiber bending and twisting effects into consideration, a new model of XT in MCFs has been established based on the power coupling theory [36, 56]. In this model, the statistical mean of the XT between two adjacent cores of a homogeneous MCF can be expressed as

$$\mathrm{XT}_{\mu} \approx \frac{2\kappa_{ji}^{2} R_{b}}{\beta\Lambda} L, \tag{2.4}$$

where κ_{ji}, R_b, L, β and Λ are the mode coupling coefficient between core j and core i, fiber bending radius, total fiber length, propagation constant in each core and core pitch, respectively.

Under the constraints of a fixed effective area, a fixed cutoff wavelength and a fixed core pitch, the XT can be reduced either by confining the mode in each core more strongly, which results in less mode overlaps between adjacent cores or by introducing phase mismatching, which significantly reduces the coupling between adjacent cores.

2.3 XT Reduction Techniques

2.3.1 XT reduction by strong mode confinement

In order to confine the spatial mode strongly in each core of an MCF, a material with a lower index compared to the cladding can be introduced around each core, as shown in Fig. 2.4. A lower index can be achieved by either using air holes or doping. Based on these two different methods, hole-assisted/hole-walled structures and a TA structure were proposed.

Hole-assisted/hole-walled structures

Hole-assisted structure was proposed for achieving high core density [57, 58], where the cross-sectional view of such fiber is shown in Fig. 2.5(a). By introducing air holes around each core, the mode can be strongly confined without affecting the effective area and cutoff wavelength, resulting

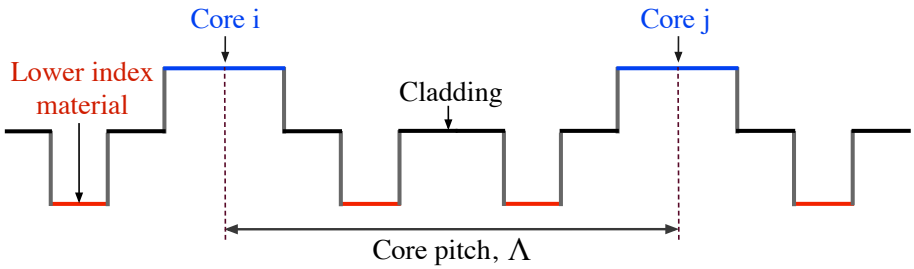

Figure 2.4: Refractive index profiles of two adjacent cores (separated by a distance of Λ) in an MCF, with a lower index material surrounding each core.

in a smaller mode coupling coefficient between adjacent cores. Another air hole based structure was also proposed, termed as "hole-walled structure" [59], where arrayed holes walling is used in between cores, as shown in Fig. 2.5(b).

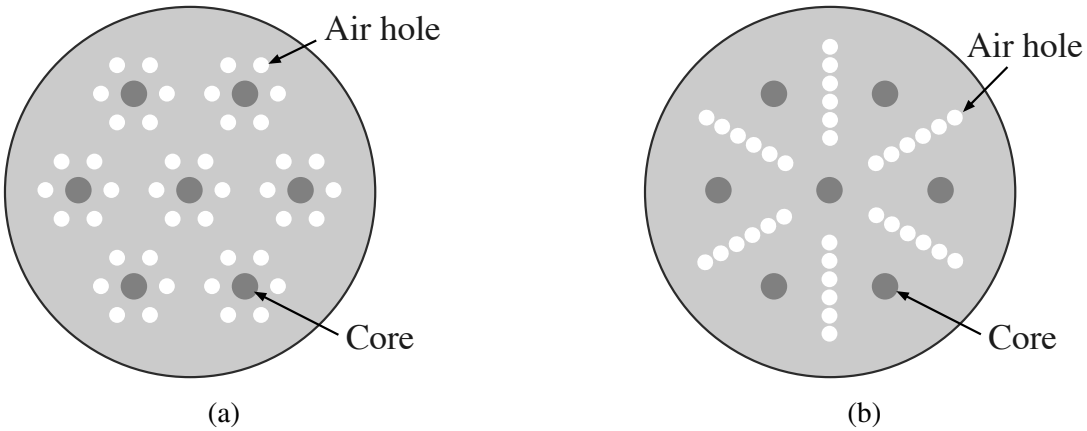

Figure 2.5: Cross-sectional views of 7-core fibers with (a) a hole-assisted structure and (b) a hole-walled structure.

Hole-assisted/hole-walled MCFs have not widely been used for high-capacity transmission experiments, due to the fact that the holes can be easily damaged during the fiber splicing process and other connection issues.

Trench-Assisted (TA) structure

The TA structure was firstly proposed to reduce the bending loss in fiber-to-the-home applications [60] due to its strong mode confinement capability. It was then proposed to be adopted in MCFs for XT reduction [31]. Compared to hole-assisted MCFs, TA-MCFs have widely been used

in state-of-the-art transmission experiments [42, 44]. The refractive index profile of a TA structure and the cross-sectional view of a 7-core fiber with a TA structure are shown in Fig. 2.6(a) and Fig. 2.6(b), respectively.

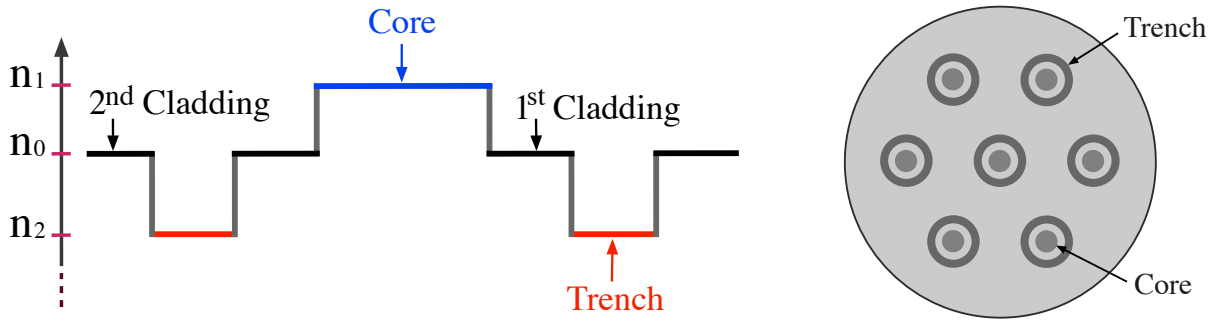

Figure 2.6: (a) Refractive index profile of a TA structure and (b) a cross-sectional view of a 7-core fiber with a TA structure.

2.3.2 XT reduction by phase mismatching

Heterogeneous core arrangement

An issue with homogeneous MCFs is their low core density which limits the total capacity per fiber. A heterogeneous core arrangement, where the neighboring cores have different refractive index profiles, has been proposed to reduce the XT [28], or in other words, to increase the core density as there is a tradeoff between the number of cores in an MCF and the XT in each core. The refractive index profiles and the corresponding effective indices in a homogeneous core arrangement and a heterogeneous core arrangement are shown in Fig. 2.7(a) and Fig. 2.7(b), respectively.

The statistical mean of XT between two adjacent cores of a heterogeneous MCF has been derived and can be written as [56]

$$\mathrm{XT}_{\mu} \approx \frac{2\kappa_{ji}^{2}}{(\Delta\beta)^{2}d}L, \tag{2.5}$$

where $\Delta\beta$ is the propagation constant difference between the two adjacent cores, core i and core j and d is the correlation length.

Figure 2.7: Refractive index profiles and corresponding effective indices in (a) a homogeneous core arrangement and (b) a heterogeneous core arrangement.

Since the XT in heterogeneous MCFs is much lower as compared to the one in homogeneous MCFs, due to the phase mismatching induced by different effective indices in non-identical cores, the heterogeneous core arrangement can be used as another effective XT reduction technique. It should be noted that the XT in heterogeneous MCFs is bending radius insensitive as R_b is not included in Eq. (2.5).

Propagation-direction interleaving (PDI)

The traditional transmission scheme is based on unidirectional propagation as shown in Fig. 2.8 where all the signals in different cores are propagating in the same direction. The forward propagated XT (denoted as XT_f) from signal i is the one that should be taken into account for signal quality degradation in core j.

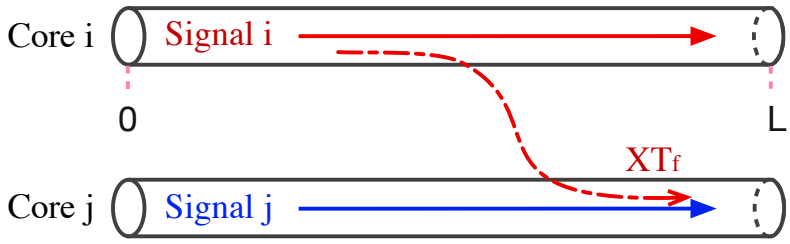

Figure 2.8: Unidirectional transmission scheme.

By reversing the propagation direction of signal j in core j, a bidirectional transmission scheme is realized, where signals in the two cores are propagating in opposite directions [61]. The scheme is often termed as "propagation-direction interleaving (PDI)" [62, 63], and it can be regarded as an extreme case of phase mismatching as the propagation constants of signals in different propagation directions have the opposite signs. Ideally, the XT reduction effect in PDI should be much more

significant than the one in heterogeneous core arrangement, as the propagation constant difference between adjacent cores in PDI is much larger than that between non-identical cores in heterogeneous MCFs. Thus, PDI has a great potential for XT reduction in high-count MCFs.

The principle of PDI is illustrated in Fig. 2.9 where the signals in core i and core j are propagating in opposite directions. Thus, the XT that should be taken into account for signals in core j is XT_b, the backward propagated XT and it is normally much smaller than XT_f (forward propagated XT). For the case of unidirectional transmission scheme, XT_f is the one that is normally considered.

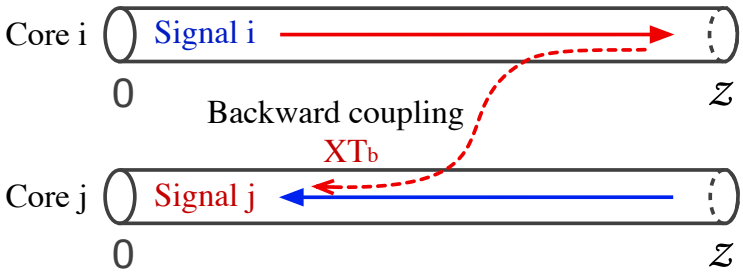

Figure 2.9: Propagation-direction interleaving.

Our derivation process of the backward propagated XT in PDI can be found as follows.

Assuming P_0 is the input power at core i, the powers in core i and j at a distance of z from the input side of P_0 are expressed as

$$\begin{cases} P_i(z) = P_0 \exp(-h_{ij}z)\cosh(-h_{ij}z)\exp(-\alpha z) \\ P_j(z) = P_0 \exp(-h_{ij}z)\sinh(-h_{ij}z)\exp(-\alpha z), \end{cases} \tag{2.6}$$

where h_{ij} and α are the power coupling coefficient between two adjacent cores and the attenuation coefficient of the fiber in linear scale, respectively.

For small $h_{ij}z$, we have $\exp(-2h_{ij}z) \approx 1 - 2h_{ij}z$, and thus,

$$\begin{cases} \dfrac{1+\exp(-2h_{ij}z)}{2} \approx 1 - h_{ij}z \\ \dfrac{1-\exp(-2h_{ij}z)}{2} \approx h_{ij}z. \end{cases} \tag{2.7}$$

With the help of Eq. (2.7), the power at a distance of z from the input side in core i, $P_i(z)$ can be

simplified as

$$\begin{aligned} P_{\mathrm{i}}(z) &= P_0 \exp(-h_{\mathrm{ij}} z) \cosh(-h_{\mathrm{ij}} z) \exp(-\alpha z) \\ &= P_0 \exp(-h_{\mathrm{ij}} z) \frac{\exp(h_{\mathrm{ij}} z) + \exp(-h_{\mathrm{ij}} z)}{2} \exp(-\alpha z) \\ &= P_0 \frac{1 + \exp(-2h_{\mathrm{ij}} z)}{2} \exp(-\alpha z) \\ &\approx P_0 (1 - h_{\mathrm{ij}} z) \exp(-\alpha z). \end{aligned} \tag{2.8}$$

The power at a distance of z from the input side in core j, $P_{\mathrm{j}}(z)$ can also be simplified as

$$\begin{aligned} P_{\mathrm{j}}(z) &= P_0 \exp(-h_{\mathrm{ij}} z) \sinh(-h_{\mathrm{ij}} z) \exp(-\alpha z) \\ &= P_0 \exp(-h_{\mathrm{ij}} z) \frac{\exp(h_{\mathrm{ij}} z) - \exp(-h_{\mathrm{ij}} z)}{2} \exp(-\alpha z) \\ &= P_0 \frac{1 - \exp(-2h_{\mathrm{ij}} z)}{2} \exp(-\alpha z) \\ &\approx P_0 h_{\mathrm{ij}} z \exp(-\alpha z). \end{aligned} \tag{2.9}$$

Using Eq. (4) from Ref. [64], the total backscattered field $\vec{\mathcal{E}}_{\mathrm{b}}(t)$ is the superposition of the field contributions from the disjoint scatter sections and it is expressed as

$$\vec{\mathcal{E}}_{\mathrm{b}}(t) = \sum_{n=1}^{N} \Delta\vec{\mathcal{E}}_{\mathrm{b}}(t, n\Delta l), \tag{2.10}$$

where N is the total number of scatter sections for a fiber length of L, $\Delta l = L/N$ is the length of each scatter section and n is the scatter section number.

Using Eq. (A2) from Ref. [64], $\alpha_{\mathrm{R}} S = 2\sigma^2$ from Ref. [65] and Eq. (2.8), the mean backscattered power at $z = 0$ in core i from $P_{\mathrm{i}}(z)$ can be simplified as

$$
\begin{aligned}
P_{\text{bi-i}}(0) &= S\,\alpha_{\text{R}} \sum_{n=1}^{N} P_{\text{i}}(n\Delta l)\exp(-\alpha n\Delta l) \\
&= S\,\alpha_{\text{R}} \int_0^L P_{\text{i}}(z)\exp(-\alpha z)\,dz \\
&\approx S\,\alpha_{\text{R}} P_0 \int_0^L (1 - h_{\text{ij}} z)\exp(-2\alpha z)\,dz \\
&\approx S\,\alpha_{\text{R}} P_0 \int_0^L \exp(-2\alpha z)\,dz \\
&= \frac{S\,\alpha_{\text{R}}}{2\alpha} P_0[1 - \exp(-2\alpha L)],
\end{aligned}
\tag{2.11}
$$

where S and α_{R} are the recapture factor of the Rayleigh scattering component into the backward direction and the attenuation coefficient due to Rayleigh scattering, respectively.

The total mean backscattered power at z = 0 in core j is composed of two parts. One is backscattered part from the transmitted power in core j, expressed as $P_{\text{bj-j}}(0)$, where the subscript $_{\text{bj-j}}$ means that the power is originated from core j, denoted as $_{\text{-j}}$ and then backscattered in the same core, denoted as $_{\text{bj}}$, thus, is denoted as $P_{\text{bj-j}}(0)$. The other one is the co-directionally coupled part from the backscattered power in core i, expressed as $P_{\text{j-bi}}(0)$, where the subscript $_{\text{j-bi}}$ means that the power is originated from the backscattered power in core i, denoted as $_{\text{-bi}}$ and then co-directionally coupled to core j, denoted as $_{\text{j}}$, thus, is denoted as $P_{\text{j-bi}}(0)$.

With the same principle and using Eq. (2.9), the mean backscattered power at $z = 0$ in core j from $P_{\text{j}}(z)$ can be derived as

$$
\begin{aligned}
P_{\text{bj-j}}(0) &= S\,\alpha_{\text{R}} \int_0^L P_{\text{j}}(z)\exp(-\alpha z)\,dz \\
&= S\,\alpha_{\text{R}} P_0 h_{\text{ij}} \int_0^L z\exp(-2\alpha z)\,dz \\
&= S\,\alpha_{\text{R}} P_0 h_{\text{ij}} \frac{1 - (1 + 2\alpha L)\exp(-2\alpha L)}{4\alpha^2} \\
&= \frac{S\,\alpha_{\text{R}}}{2\alpha} P_0 h_{\text{ij}} \left[\frac{1 - \exp(-2\alpha L)}{2\alpha} - L\exp(-2\alpha L)\right].
\end{aligned}
\tag{2.12}
$$

On the other hand, the mean power at $z = 0$ in core j coupled from the backscattered power in core i, can be expressed as

$$
\begin{aligned}
P_{\text{j-bi}}(0) &= S\,\alpha_{\text{R}} \sum_{n=1}^{N} P_{\text{i}}(n\Delta l) h_{\text{ij}} n\Delta l \exp(-\alpha n\Delta l) \\
&= S\,\alpha_{\text{R}} P_0 h_{\text{ij}} \int_0^L z \exp(-2\alpha z)\, dz \\
&= S\,\alpha_{\text{R}} P_0 h_{\text{ij}} \frac{1-(1+2\alpha L)\exp(-2\alpha L)}{4\alpha^2} \\
&= \frac{S\,\alpha_{\text{R}}}{2\alpha} P_0 h_{\text{ij}} \left[\frac{1-\exp(-2\alpha L)}{2\alpha} - L\exp(-2\alpha L) \right].
\end{aligned}
\tag{2.13}
$$

Eventually, the total mean backscattered power at $z = 0$ in core j can be written as

$$
\begin{aligned}
P_{\text{bj}} &= P_{\text{bj-j}}(0) + P_{\text{j-bi}}(0) \\
&= \frac{S\,\alpha_{\text{R}}}{2\alpha} P_0 h_{\text{ij}} \left[\frac{1-\exp(-2\alpha L)}{\alpha} - 2L\exp(-2\alpha L) \right].
\end{aligned}
\tag{2.14}
$$

Using the XT definition of Eq. (2.1), the forward propagated XT in linear scale in the fiber with total length of L, can be expressed as

$$
\text{XT}_{\text{f}} = \frac{P_{\text{j}}(L)}{P_{\text{i}}(L)} = \frac{h_{\text{ij}} L}{1 - h_{\text{ij}} z} \approx h_{\text{ij}} L. \tag{2.15}
$$

The backward propagated XT in linear scale in the fiber with a total length of L, can also be obtained in the same manner and it is expressed as

$$
\begin{aligned}
\text{XT}_{\text{b}} = \frac{P_{\text{bj}}}{P_{\text{i}}(L)} &\approx \frac{S\,\alpha_{\text{R}}}{2\alpha} P_0 h_{\text{ij}} \left[\frac{1-\exp(-2\alpha L)}{\alpha} - 2L\exp(-2\alpha L) \right] / P_0 \exp(-\alpha L) \\
&= \frac{S\,\alpha_{\text{R}}}{2\alpha} h_{\text{ij}} L \left[\frac{\exp(\alpha L) - \exp(-\alpha L)}{\alpha L} - 2\exp(-\alpha L) \right].
\end{aligned}
\tag{2.16}
$$

Using the formulation for XT_{f} and XT_{b} above, the difference of XT (in dB) by PDI compared to the unidirectional propagation case can be expressed as

$$
\begin{aligned}
\text{XT}_{\text{b\_dB}} - \text{XT}_{\text{f\_dB}} &= 10\log\left(\frac{\text{XT}_{\text{b}}}{\text{XT}_{\text{f}}}\right) \\
&= 10\log\left\{ \frac{S\alpha_{\text{R}}}{2\alpha} \left[\frac{\exp(\alpha L) - \exp(-\alpha L)}{\alpha L} - 2\exp(-\alpha L) \right] \right\}.
\end{aligned}
\tag{2.17}
$$

As can be seem from Eq. (2.17), the XT difference does not depend on the core pitch (or in other means, mode coupling coefficient) as this parameter is not included in the equation. For a fiber length of 100 km, XT_b is calculated to be around 18.6 dB lower than XT_f. Thus, if this property is used in an effective manner, significant amount of XT reduction can be achieved.

2.4 Examples of Fabricated MCFs

The first one Pbit/s capacity transmission experiment was achieved by adopting a 52 km, 12-core fiber with a one-ring structure (ORS) [44]. The cross-sectional view of the fiber is shown in Fig. 2.10(a) with a cladding diameter (D_{clad}), a cladding thickness (CT) and a core pitch of 225 μm, 38.9 μm, 36.8 μm, respectively. The corresponding effective areas at 1550 nm and 1625 nm are 80.7 μm^2 and 84.7 μm^2, respectively.

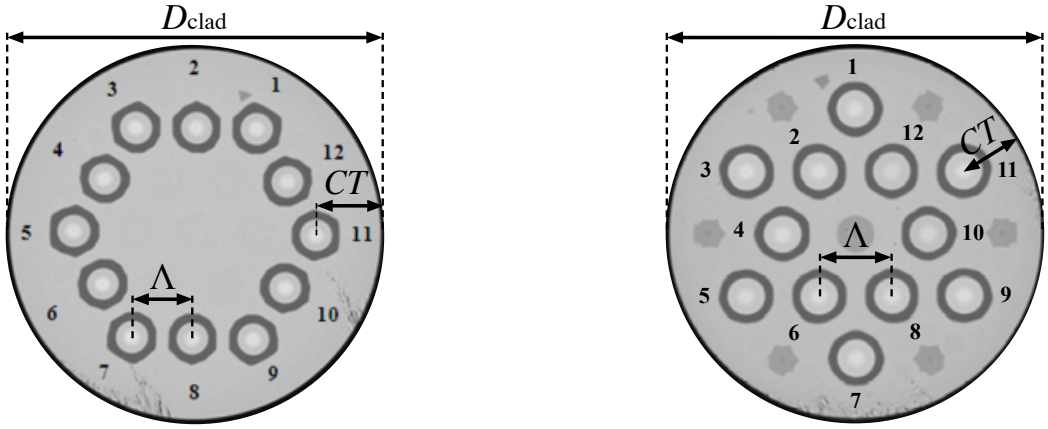

Figure 2.10: Cross-sectional views of fabricated 12-core fibers with (a) ORS and (b) DRS.

Another 50 km, 12-core fiber was also fabricated for the PDI transmission scheme, with a dual-ring structure (DRS) [62, 66] as shown in Fig. 2.10(b). The D_{clad}, CT and core pitch are 230 μm, 37.7 μm, 44.6 μm, respectively. The corresponding effective area at 1550 nm is 105.8 μm^2, 30% larger than the one in the previously mentioned 12-core fiber with ORS. Both fabricated 12-core fibers are wound on bobbins with the same bending radius of 155 mm.

2.5 XT Target

There is a tradeoff between the number of cores in an MCF and the XT in each core. In order to design MCFs with more than 30 cores per fiber and adopt modulation format suitable for practical applications, the XT target of -30 dB over 100 km seems reasonable, which also translates to the required XT value of -20 dB over 1000 km for 100 G signals adopting PDM-QPSK modulation format with OSNR penalty of less than 0.5 dB. The maximum values of XT acceptable for suppressing the XT-induced OSNR penalty to be less than 0.5 dB for other advanced modulation formats such as 16QAM, 32QAM, and 64QAM are around -27 dB, -30 dB, -34 dB, respectively.

2.6 Summary

As the inter-core XT between adjacent cores limits the total number of cores that can be packed in an MCF with a fixed cladding diameter, it is essential and important to investigate the XT properties for designing high-count MCFs. In this chapter, we reviewed the formulations of inter-core XT in MCFs both for the ideal straight condition without fiber bending and a more realistic condition with fiber bending. The XT behaviors under these two conditions are very different where the XT in MCFs under the ideal straight condition changes periodically with respect to the fiber length, while the XT in MCFs with fiber bending effects increases linearly with the fiber length. As fibers are not straight but with certain bending radii in deployed optical fiber cables, the XT formulation under the bending condition should be used. Such bending is necessary and introduced on purpose in order to provide an extra length so that there will be no tension applied onto the fibers under real deployment conditions. The results obtained using this model agree well with measurement results using fabricated MCFs wound on bobbins with certain diameters.

Two different XT reduction principles are described, which are strong mode confinement in a core and phase mismatching between adjacent cores. Hole-assisted/hole-walled structures and a TA structure belong to the 1st category as both structures confine the mode strongly in the core. The heterogeneous core arrangement and PDI belong to the 2nd category where the propagation constants in adjacent cores are different, resulting in phase mismatching.

In this thesis, we focus on high-count MCFs designs utilizing a TA structure and PDI for XT reduction. Our approach is based on an analytical model which is different from other research groups where MCFs design are based on numerical simulations. In order to design MCFs with

ultra-low XT for long-distance and high-capacity MCF transmission systems, it is important to understand the effects of these various fiber parameters on the XT reduction in TA-MCFs making full use of the analytical model.

□ End of chapter.

Chapter 3

Analytical Model for TA-MCFs

3.1 Introduction

In the previous chapter, we reviewed different XT reduction techniques based on strong mode confinement in each fiber core and phase mismatching between adjacent cores. As the strong mode confinement techniques, hole-assisted/hole-walled structures are not as widely used as TA structure due to the fact that the holes can be easily damaged during the fiber splicing process and other connection issues. For the phase mismatching techniques, heterogeneous core arrangement has been extensively investigated [37, 67–69] while the PDI transmission scheme is another effective, but new XT reduction technique for which we have newly derived an analytical expression for estimating XT reduction taking into account the backward propagated XT in the previous chapter. Thus, our focus in the present work will be on homogeneous MCFs with a TA structure and PDI.

TA structures have been widely adopted in MCFs and used in high-capacity space-division multiplexed transmission experiments [40, 44, 62]. Estimations of the inter-core XT in TA-MCFs were done by numerical simulations in all the reported works [31, 33, 34, 43]. Thus, the relationships between XT and fiber structural parameters such as trench width, relative refractive index difference between trench and cladding, core pitch in TA-MCFs were difficult to interpret. In order to achieve the lowest XT by TA structure and design high-count MCFs for long-distance and high-capacity transmission, however, it is important to understand the effects of different fiber parameters on XT reduction in TA-MCFs. Thus, it is desirable to develop an analytical model for inter-core XT in

TA-MCFs so that high-count MCFs can be designed quickly and reliably.

The analytical expression of the mode coupling coefficient between two adjacent cores in MCFs with a normal SI profile has been derived [55]. By adding a trench structure around each fiber core, the mode field distribution is suppressed in the cladding region and the distribution becomes much more complex compared to the one in MCFs with a normal step-index (SI) profile. In order to develop an analytical model for XT in TA-MCFs, it is essential to derive an analytical expression of the mode coupling efficient between two adjacent cores with a TA structure.

In this chapter, we derive an analytical expression for the mode coupling coefficient in TA-MCFs. The derived mode coupling coefficient in TA-MCFs can be directly related to the one in normal SI-MCFs. Thus, the XT reduction amount (in dB) by a TA structure compared to a normal SI structure can also be formulated in a simple expression. The XT results calculated by the analytical model agree very well with the ones obtained by numerical simulations based on finite element method (FEM). One important issue in MCF transmission is the wavelength-dependent XT over the transmission band, and the wavelength-dependent XT properties are analyzed based on the analytical model. Other XT properties, i.e., relationships between XT and fiber structural parameters such as trench width, core pitch, refractive index difference between trench and cladding are also analyzed.

3.2 Mode Coupling Coefficient Formulations

Coupled mode theory deals with the mutual lightwave interactions between the two propagation modes. When the electromagnetic field distributions in each core after mode coupling do not differ substantially from those before coupling, the propagation characteristics of the coupled cores can be analyzed by the perturbation method.

The parameter which characterizes the mode coupling effect between the two adjacent cores in a directional coupler is called a mode coupling coefficient. The mode coupling coefficient from core i to core j in a directional coupler [55] is defined as

$$\kappa_{ji} = \frac{\omega\varepsilon_0 \int_{-\infty}^{\infty}\int_{-\infty}^{\infty}(N^2 - N_i^2)\,\mathbf{E}_j^* \cdot \mathbf{E}_i\, dxdy}{\int_{-\infty}^{\infty}\int_{-\infty}^{\infty}\mathbf{u}_z \cdot (\mathbf{E}_j^* \times \mathbf{H}_j + \mathbf{E}_j \times \mathbf{H}_j^*)\, dxdy}, \tag{3.1}$$

where ω is an angular frequency of the electromagnetic fields, and ε_0 is the permittivity of the

medium. $N^2(x, y)$ denotes the refractive index distribution in the entire coupled region while N_i^2 represents the refractive index distribution of waveguide i. $\mathbf{E}_i/\mathbf{H}_i$ and $\mathbf{E}_j/\mathbf{H}_j$ are the electric/magnetic fields in waveguides i and j, respectively. * denotes the complex conjugate and $\mathbf{u}_z$ is the unit vector.

3.2.1 Mode coupling coefficient in normal SI-MCFs

For homogeneous MCFs, all the cores in an MCF have the same refractive index profile. The cross-sectional view and the refractive index profile of a homogeneous MCF with a normal SI profile are shown in Fig. 3.1(a) and Fig. 3.1(b), respectively. The refractive indices for the core and the cladding are n_1 and n_0, respectively. The core radius, and the relative refractive index difference between core and cladding are a_1 and Δ_1, respectively. The distance between adjacent cores is within a range of around 30 μm to 50 μm, depending on the total number of cores and the cladding diameter in an MCF. Thus, the mode fields of adjacent cores essentially overlap (or couple) with each other, resulting in inter-core XT.

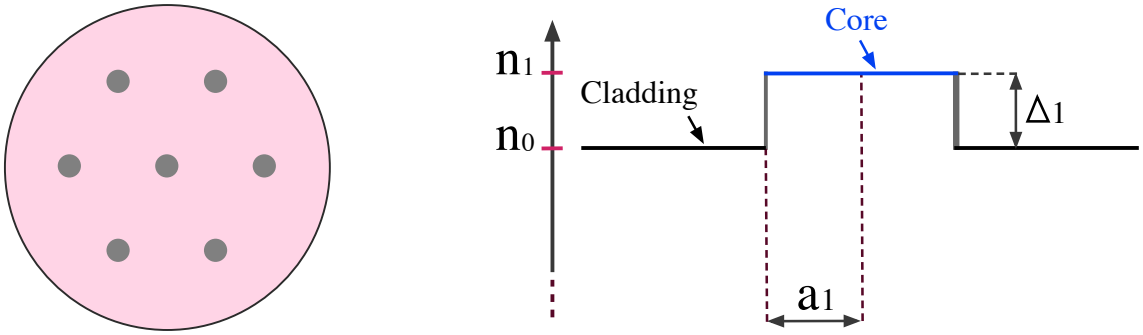

Figure 3.1: (a) Cross-sectional view of a normal SI 7-core fiber and (b) the corresponding refractive index profile for each core.

The mode coupling coefficient between two adjacent cores with SI profiles in a directional coupler [55] can be simplified to

$$\kappa_{ji}^{'} = \frac{\sqrt{\Delta_1}}{a_1} \frac{U_1^2}{V_1^3 K_1^2(W_1)} \sqrt{\frac{\pi a_1}{W_1 \Lambda}} \exp\Big(- \frac{W_1}{a_1} \Lambda \Big), \tag{3.2}$$

where $U_1^2 = a_1^2(k^2 n_1^2 - \beta^2)$ and $W_1^2 = a_1^2(\beta^2 - k^2 n_0^2)$, in which β is the propagation constant and $k = 2\pi/\lambda$ is the wave number, where λ is the wavelength of light in vacuum. Λ is the core pitch and

$V_1 = k\,a_1 n_1 (2\Delta_1)^{1/2}$ is the V number which determines the modes propagating in a fiber. $K_1(W_1)$ is the modified Bessel function of the 2nd kind with 1st order.

3.2.2 Mode coupling coefficient in TA-MCFs

As shown in Fig. 3.2, when two homogeneous TA fiber cores are placed close to each other, the modes of each core either couple or interfere with each other. The 1st and 2nd claddings are assumed to have the same refractive index. The refractive indices of the core, the cladding and the trench are n_1, n_0 and n_2, respectively.

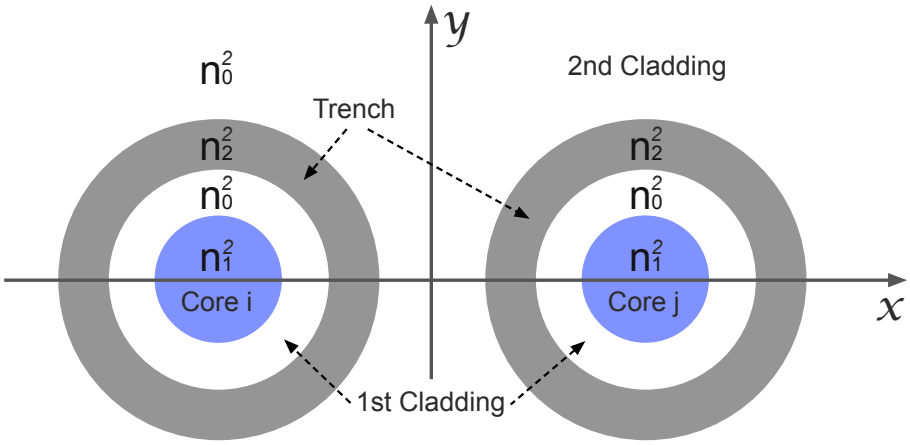

Figure 3.2: Cross-sectional view of two homogeneous TA fiber cores.

The corresponding refractive-index distribution $N^2(x, y)$ of the two closely packed homogeneous TA cores, the refractive-index distribution N_i^2 of waveguide i and the difference of the refractive-index distribution $N^2 - N_i^2$ are shown in Fig. 3.3(a), Fig. 3.3(b) and Fig. 3.3(c), respectively. As can be seen from the figures, the actual value of $N^2 - N_i^2$ in core j equals $n_1^2 - n_0^2$ and equals zero in the other regions.

Thus, the mode coupling coefficient formulation of Eq. (3.1) can be simplified into

$$\kappa_{ji} = \frac{\omega\varepsilon_0 \int_0^{2\pi}\int_0^{a_1} (n_1^2 - n_0^2)\,\mathbf{E}_j^* \cdot \mathbf{E}_i\, r dr d\theta}{\int_{-\infty}^{\infty}\int_{-\infty}^{\infty} \mathbf{u}_z \cdot (\mathbf{E}_j^* \times \mathbf{H}_j + \mathbf{E}_j \times \mathbf{H}_j^*)\, dxdy}. \tag{3.3}$$

The optical power carried by each eigen mode in waveguide j is expressed as

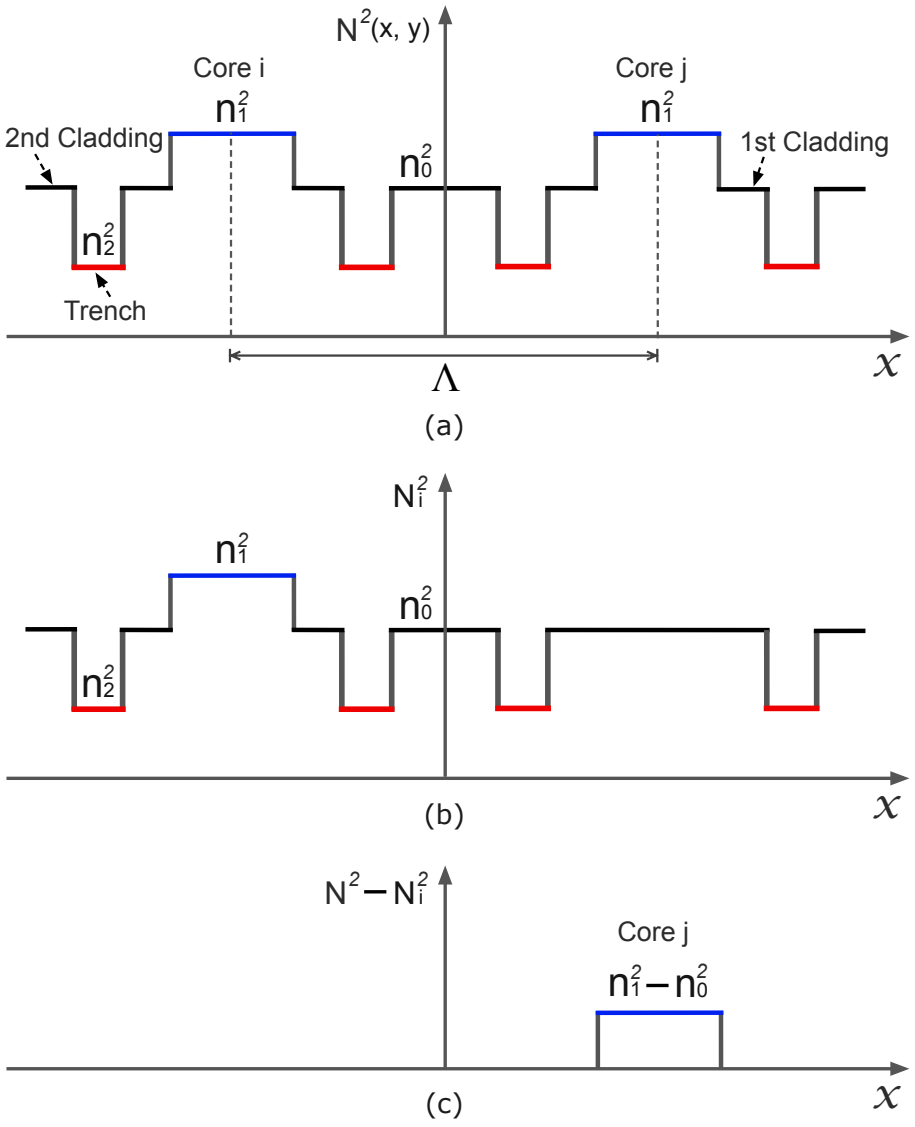

Figure 3.3: Refractive-index distribution (a) $N^2(x, y)$ of the two TA fiber cores, (b) N_i^2 of waveguide i and (c) the difference of the refractive-index distribution $N^2 - N_i^2$.

$$P_j = \frac{1}{2}\int_{-\infty}^{\infty}\int_{-\infty}^{\infty} \mathbf{u}_z \cdot (\mathbf{E}_j \times \mathbf{H}_j^*)\, dxdy. \tag{3.4}$$

Thus, the denominator of Eq. (3.3) can be expressed as

$$\int_{-\infty}^{\infty}\int_{-\infty}^{\infty} \mathbf{u}_z \cdot (\mathbf{E}_j^* \times \mathbf{H}_j + \mathbf{E}_j \times \mathbf{H}_j^*)\, dxdy = 4P_j. \tag{3.5}$$

The mode coupling coefficient in TA-MCFs can then be simplified to

$$\kappa_{ji} = \frac{\omega\varepsilon_0(n_1^2 - n_0^2)}{4P_j}\int_0^{2\pi}\int_0^{a_1} \mathbf{E}_j^* \cdot \mathbf{E}_i\, rdrd\theta. \tag{3.6}$$

The refractive index profile and cross-sectional dimensions of a TA structure are shown in Fig. 3.4. The relative refractive index differences between the core and the cladding, and that between the trench and the cladding are Δ_1 and Δ_2, respectively. The core radius, the distance from the outer edge of the 1st cladding to the core center, the distance from the outer edge of the trench to the core center, and the trench width are a_1, a_2, a_3 and w_{tr}, respectively.

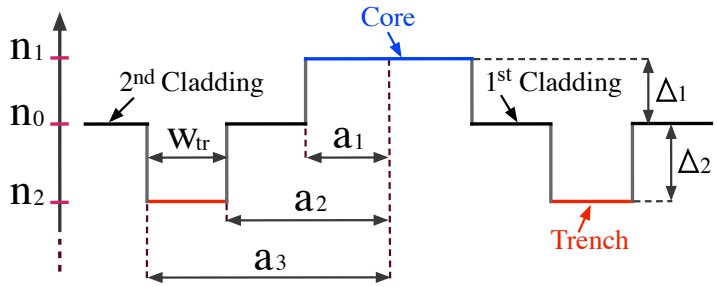

Figure 3.4: Refractive index profile and cross-sectional dimensions of a TA structure.

We then define the wave number in core q ($q = i,\ j$), the cladding and the trench along the transversal direction as following [67]

$$\begin{cases} \xi_q = \sqrt{n_1^2k^2 - \beta_q^2}, \\ \delta_q = \sqrt{\beta_q^2 - n_0^2k^2}, \\ \gamma_q = \sqrt{\beta_q^2 - n_2^2k^2}, \end{cases} \tag{3.7}$$

where β_q is the propagation constant in core q.

The normalized frequency (V_1 and V_2), the normalized transverse wave number in core q, the cladding and the trench (U_1, W_1 and W_2, respectively) can be expressed as

$$\begin{cases} V_1 = a_1 k \sqrt{n_1^2 - n_0^2}, \\ V_2 = a_1 k \sqrt{n_0^2 - n_2^2}, \\ U_1 = a_1 \xi_{\mathrm{q}} = \sqrt{V_1^2 - W_1^2}, \\ W_1 = a_1 \delta_{\mathrm{q}} = 1.1428 V_1 - 0.996, \\ W_2 = a_1 \gamma_{\mathrm{q}} = \sqrt{V_2^2 + W_1^2}. \end{cases} \tag{3.8}$$

As the sizes of the 1st cladding and the trench in a TA structure are not infinitely large, the solutions in these two regions also contain the modified Bessel functions of the 1st kind $I_0(W_1 r/a_1)$, which makes the derivation of mode coupling coefficients in TA-MCFs difficult. If $I_0(W_1 r/a_1)$ in the 1st cladding and in the trench are ignored, the mode coupling coefficient between two adjacent cores in heterogeneous TA-MCFs can be written as Eq. (33) in Ref. [67], which can be simplified to the following expression in the homogeneous case

$$\begin{aligned} \kappa_{\mathrm{ji}}'' = {} & \frac{k\,(n_1^2 - n_0^2) W_1 U_1 L_{\mathrm{i}}}{n_1 a_1^2 V_1^2 J_1^2(U_1)} \sqrt{\frac{\pi a_1}{2 W_1 \Lambda}} \exp\Big(- \frac{W_1}{a_1}\Lambda \Big) \int_0^{a_1} J_0\Big(\frac{U_1}{a_1} r\Big) \\ & \times I_0\Big[\Big(\frac{W_1}{a_1} + \frac{P_1 - P_2 + Y_1 - Y_2}{\Lambda - r}\Big) r\Big] \exp\Big[- (P_1 - P_2 + Y_1 - Y_2) \frac{\Lambda}{\Lambda - r}\Big] r\, dr, \end{aligned} \tag{3.9}$$

where L_{i}, P_1, P_2, Y_1, Y_2 and $P_1 - P_2 + Y_1 - Y_2$ can be expressed as

$$\begin{cases} L_{\mathrm{i}} = \dfrac{J_1(U_1) K_1(W_1 a_2/a_1) K_1(W_2 a_3/a_1)}{K_1(W_1) K_1(W_2 a_2/a_1) K_1(W_1 a_3/a_1)}, \\ P_1 = W_1 \dfrac{\Lambda - a_3}{a_1}, \quad P_2 = W_2 \dfrac{\Lambda - a_3}{a_1}, \\ Y_1 = W_2 \dfrac{\Lambda - a_2}{a_1}, \quad Y_2 = W_1 \dfrac{\Lambda - a_2}{a_1}, \\ P_1 - P_2 + Y_1 - Y_2 = (W_2 - W_1) \dfrac{a_3 - a_2}{a_1} = (W_2 - W_1) \dfrac{w_{\mathrm{tr}}}{a_1}. \end{cases} \tag{3.10}$$

In order to compare with the mode coupling coefficient as Eq. (33) in Ref. [67], the one in a normal SI structure should also be expressed in a similar form. With Eq. (4.118) in Ref. [55] and $z = r/a_1$, the integration part of Eq. (4.118) in Ref. [55] can be written as

$$\int_0^{2\pi}\int_0^{a_1} J_0\Big(\frac{U_1}{a_1}r\Big)\exp\Big(\frac{W_1}{a_1}r\cos\theta\Big)\,r\,dr\,d\theta = 2\pi\int_0^{a_1} J_0\Big(\frac{U_1}{a_1}r\Big)I_0\Big(\frac{W_1}{a_1}r\Big)\,r\,dr, \tag{3.11}$$

where $J_0(U_1 r/a_1)$ is the Bessel function of the 1$^{\text{st}}$ kind with zero order and $I_0(W_1 r/a_1)$ is the modified Bessel function of the 1$^{\text{st}}$ kind with zero order, in which r is the radial distance from the center of the fiber core q. To make an easy comparison between a normal SI structure and a TA structure, the core radius a_1, the relative refractive index difference between core and cladding Δ_1 are assumed to be the same in these two structures .

Finally, the mode coupling coefficient of a directional coupler with a normal SI profile can also be expressed as

$$\kappa_{ji}^{'} = k\,(n_1^2 - n_0^2)\frac{W_1^2}{n_1 a_1^2 V_1^2 J_1^2(U_1)}\frac{J_0(U_1)}{K_0(W_1)}\sqrt{\frac{\pi a_1}{2W_1\Lambda}}\exp\Big(-\frac{W_1}{a_1}\Lambda\Big)\int_0^{a_1} J_0\Big(\frac{U_1}{a_1}r\Big)I_0\Big(\frac{W_1}{a_1}r\Big)\,r\,dr, \tag{3.12}$$

where $J_1(U_1)$ is the Bessel function of the 1$^{\text{st}}$ kind with 1$^{\text{st}}$ order and $K_0(W_1)$ is the modified Bessel function of the 2$^{\text{nd}}$ kind with zero order.

Comparing Eq. (3.12) with Eq. (3.9), we have

$$\frac{\kappa_{ji}^{''}}{\kappa_{ji}^{'}} = \frac{U_1 L_i\displaystyle\int_0^{a_1} J_0\Big(\frac{U_1}{a_1}r\Big)I_0\Big[\Big(\frac{W_1}{a_1}+\frac{P_1-P_2+Y_1-Y_2}{\Lambda-r}\Big)r\Big]\exp\Big[-(P_1-P_2+Y_1-Y_2)\frac{\Lambda}{\Lambda-r}\Big]\,r\,dr}{W_1\dfrac{J_0(U_1)}{K_0(W_1)}\displaystyle\int_0^{a_1} J_0\Big(\frac{U_1}{a_1}r\Big)I_0\Big(\frac{W_1}{a_1}r\Big)\,r\,dr}. \tag{3.13}$$

For large arguments of ax and $(a+b)x$, the modified Bessel function of the 1$^{\text{st}}$ kind can be approximated as

$$I_0(ax) \approx \frac{1}{\sqrt{2\pi ax}}\exp(ax), \qquad I_0[(a+b)x] \approx \frac{1}{\sqrt{2\pi(a+b)x}}\exp[(a+b)x], \tag{3.14}$$

respectively, where $a > b > 0$.

If b is relatively small compared to a, $I_0[(a+b)x]$ can be related to $I_0(ax)$ by the following expression with good accuracy using the above relationship

$$I_0[(a+b)x] \approx \sqrt{\frac{a}{a+b}}\, I_0(ax)\exp(bx). \tag{3.15}$$

It is interesting to note that the approximation in Eq. (3.14) is valid only for large arguments of ax and $(a+b)x$, while Eq. (3.15) is valid even when the argument $(a+b)x$ is small. As typical values of Λ (i.e. 30 μm to 50 μm) can be more than 5 times larger than the trench width (i.e. 4.5 μm) and $(P_1 - P_2 + Y_1 - Y_2)/(\Lambda - r) = (W_2 - W_1)w_{\mathrm{tr}}/[a_1(\Lambda - r)] > 0$ is much smaller than W_1/a_1, using Eq. (3.15), we have

$$I_0\left[\left(\frac{W_1}{a_1} + \frac{P_1 - P_2 + Y_1 - Y_2}{\Lambda - r}\right)r\right] \approx \sqrt{\Gamma}\, I_0\left(\frac{W_1}{a_1}r\right)\exp\left(\frac{P_1 - P_2 + Y_1 - Y_2}{\Lambda - r}r\right), \tag{3.16}$$

where Γ is a coefficient which depends on the fiber structural parameters.

Γ can be expressed as

$$\Gamma = \frac{W_1/a_1}{W_1/a_1 + (P_1 - P_2 + Y_1 - Y_2)/\Lambda} = \frac{W_1}{W_1 + (W_2 - W_1)w_{\mathrm{tr}}/\Lambda}, \tag{3.17}$$

in which r has been dropped since $(P_1 - P_2 + Y_1 - Y_2)/(\Lambda - r)$ is much smaller than W_1/a_1 and r is much smaller than Λ.

Substituting Eq. (3.16) into Eq. (3.13), the ratio between the mode coupling coefficients for the two structures becomes

$$\begin{aligned}
\frac{\kappa''_{ji}}{\kappa'_{ji}} &= \frac{U_1 L_i \int_0^{a_1} J_0\left(\frac{U_1}{a_1}r\right)\sqrt{\Gamma}\, I_0\left(\frac{W_1}{a_1}r\right)\exp\left(\frac{P_1 - P_2 + Y_1 - Y_2}{\Lambda - r}r\right)\exp\left[-(P_1 - P_2 + Y_1 - Y_2)\frac{\Lambda}{\Lambda - r}\right]r\,dr}{W_1\frac{J_0(U_1)}{K_0(W_1)}\int_0^{a_1} J_0\left(\frac{U_1}{a_1}r\right)I_0\left(\frac{W_1}{a_1}r\right)r\,dr} \\
&= \frac{\sqrt{\Gamma}U_1 L_i \int_0^{a_1} J_0\left(\frac{U_1}{a_1}r\right)I_0\left(\frac{W_1}{a_1}r\right)\exp\left[-(P_1 - P_2 + Y_1 - Y_2)\frac{\Lambda - r}{\Lambda - r}\right]r\,dr}{W_1\frac{J_0(U_1)}{K_0(W_1)}\int_0^{a_1} J_0\left(\frac{U_1}{a_1}r\right)I_0\left(\frac{W_1}{a_1}r\right)r\,dr} \\
&= \frac{\sqrt{\Gamma}U_1 L_i \exp\left[-(P_1 - P_2 + Y_1 - Y_2)\right]}{W_1\frac{J_0(U_1)}{K_0(W_1)}}.
\end{aligned} \tag{3.18}$$

Assuming $n = 1$ in the dispersion equation Eq. (3.71) for a normal SI fiber in Ref. [55], we have

$$\frac{J_0(U_1)}{U_1 J_1(U_1)} = \frac{K_0(W_1)}{W_1 K_1(W_1)}. \tag{3.19}$$

Substituting Eq. (3.19) into Eq. (3.18), we obtain

$$\frac{\kappa_{ji}^{''}}{\kappa_{ji}^{'}} = \frac{\sqrt{\Gamma} L_i \exp\left[-(P_1 - P_2 + Y_1 - Y_2)\right]}{\frac{J_1(U_1)}{K_1(W_1)}}. \tag{3.20}$$

For $x \geq 2$, the modified Bessel function of the 2nd kind can be approximated as

$$K_1(x) \approx K_0(x) \approx \sqrt{\frac{\pi}{2x}} \exp(-x). \tag{3.21}$$

Thus, L_i in Eq. (3.10) can be simplified to

$$L_i = \frac{J_1(U_1)}{K_1(W_1)} \exp\left[-(W_2 - W_1)\frac{w_{tr}}{a_1}\right]. \tag{3.22}$$

Eventually, the ratio between the mode coupling coefficients for the two structures becomes

$$\frac{\kappa_{ji}^{''}}{\kappa_{ji}^{'}} = \sqrt{\Gamma} \exp\left[-(P_1 - P_2 + Y_1 - Y_2)\right] \exp\left[-(W_2 - W_1)\frac{w_{tr}}{a_1}\right] = \sqrt{\Gamma} \exp\left[-2(W_2 - W_1)\frac{w_{tr}}{a_1}\right]. \tag{3.23}$$

Replacing $\kappa_{ji}^{'}$ with Eq. (3.2), the mode coupling coefficient between two adjacent cores with TA structures in a directional coupler can then be expressed as

$$\kappa_{ji}^{''} = \frac{\sqrt{\Gamma}\sqrt{\Delta_1}}{a_1} \frac{U_1^2}{V_1^3 K_1^2(W_1)} \sqrt{\frac{\pi a_1}{W_1 \Lambda}} \exp\left[-\frac{W_1 \Lambda + 2(W_2 - W_1) w_{tr}}{a_1}\right]. \tag{3.24}$$

3.3 Relating Mode Coupling Coefficients to XT

Substituting Eq. (3.2) and Eq. (3.24) into Eq. (2.4), the analytical expressions for XT in homogeneous normal SI-MCFs and homogeneous TA-MCFs can be formulated, respectively.

For estimating the XT reduction in a TA structure compared to a normal SI structure, the only difference between these two structures comes from the mode coupling coefficients. Assuming the

same bending radius, fiber length and core pitch in homogeneous MCFs with these two different structures, the ratio of XT for a TA structure to that for a normal SI structure becomes

$$\frac{\mathrm{XT}_{\mu}^{''}}{\mathrm{XT}_{\mu}^{'}} = \left(\frac{\kappa_{ji}^{''}}{\kappa_{ji}^{'}}\right)^2 = \Gamma \exp\left[-4(W_2 - W_1)\frac{w_{\mathrm{tr}}}{a_1}\right], \tag{3.25}$$

where $\mathrm{XT}_{\mu}^{''}$ and $\mathrm{XT}_{\mu}^{'}$ are the mean XT in TA-MCFs and normal SI-MCFs, respectively.

If the mean XT is expressed in dB, we have

$$\mathrm{XT}_{\mathrm{dB}}^{''} - \mathrm{XT}_{\mathrm{dB}}^{'} = 10\log_{10}\left\{\Gamma \exp\left[-4(W_2 - W_1)\frac{w_{\mathrm{tr}}}{a_1}\right]\right\} = 10\log_{10}\Gamma - 17.4(W_2 - W_1)\frac{w_{\mathrm{tr}}}{a_1}. \tag{3.26}$$

From Eq. (3.8), we have

$$V_1 = \frac{2\pi}{\lambda}a_1 n_1\sqrt{2\Delta_1}, \qquad V_2 = \frac{2\pi}{\lambda}a_1 n_0\sqrt{2|\Delta_2|}, \qquad W_2 = \sqrt{V_2^2 + W_1^2}. \tag{3.27}$$

Since $n_1 \approx n_0$ and it is assumed that $|\Delta_2|/\Delta_1 = m$, we have $V_2^2 \approx mV_1^2$. For $1.5 \le V_1 \le 2.5$ in SI fibers, an excellent approximation of W_1 can be derived by assuming that W_1 is a linear function of V_1. It can be written as $W_1 = 1.1428V_1 - 0.996$, which is within 0.2% of accuracy over the range of V_1 [70]. Thus

$$W_2 \approx \sqrt{mV_1^2 + W_1^2} = \sqrt{mV_1^2 + (1.1428V_1 - 0.996)^2}. \tag{3.28}$$

For $1.5 \le V_1 \le 2.5$, W_2 can also be approximated to be a linear function of V_1, as listed in Table 3.1, where $m = 0$ means that there is no trench, which corresponds to a normal SI structure. The approximation accuracies at $m = 1$, $m = 2$, $m = 2.206$, $m = 2.976$ and $m = 3$ are all within $\pm 0.3\%$. As the approximation can also be made when m is not an integer, the examples shown here demonstrate the possibility to express $W_2 - W_1$ as a linear function of V_1.

3.4 Comparison with Numerical Simulations

In order to derive the mode coupling coefficient for the homogeneous TA-MCFs, the modified Bessel functions of the 1$^{\mathrm{st}}$ kind $I_0(W_1 r/a_1)$ in the 1$^{\mathrm{st}}$ cladding and the trench have been ignored. Firstly, the XT obtained using Eq. (3.9) and FEM can differ. Furthermore, as the simplified analyti-

Table 3.1: Approximations of W_2 for different values of m

$m = \lvert\Delta_2\rvert/\Delta_1$	W_2	$W_2 - W_1$
0	$1.1428V_1 - 0.996$	0
$0.35/0.35 = 1$	$1.452V_1 - 0.520$	$0.309V_1 + 0.476$
$0.70/0.35 = 2$	$1.750V_1 - 0.388$	$0.607V_1 + 0.608$
$0.75/0.34 = 2.206$	$1.812V_1 - 0.383$	$0.669V_1 + 0.613$
$0.75/0.252 = 2.976$	$2V_1 - 0.312$	$0.857V_1 + 0.684$
$1.05/0.35 = 3$	$2.01V_1 - 0.320$	$0.867V_1 + 0.676$

where $m = 0.75/0.34$ and $m = 0.75/0.252$ are for the cases of fabricated 12-core fibers with ORS and DRS, respectively.

cal expression Eq. (3.24) is an approximation of the non integrable expression Eq. (3.9), comparison of the XT based on these two expressions is also needed. Comparisons have been made based on the parameters listed in Table 3.2, in which the distance from the outer edge of the 1st cladding to the core center a_2 has been assumed to be twice the core radius a_1. The effective area of each core will be reduced if the trench is placed too close to the core while the trench should be placed as close as possible to the core to have MCFs with high core density. Taking these considerations into account, the ratio $a_2/a_1 = 2$ seems to be a reasonable choice.

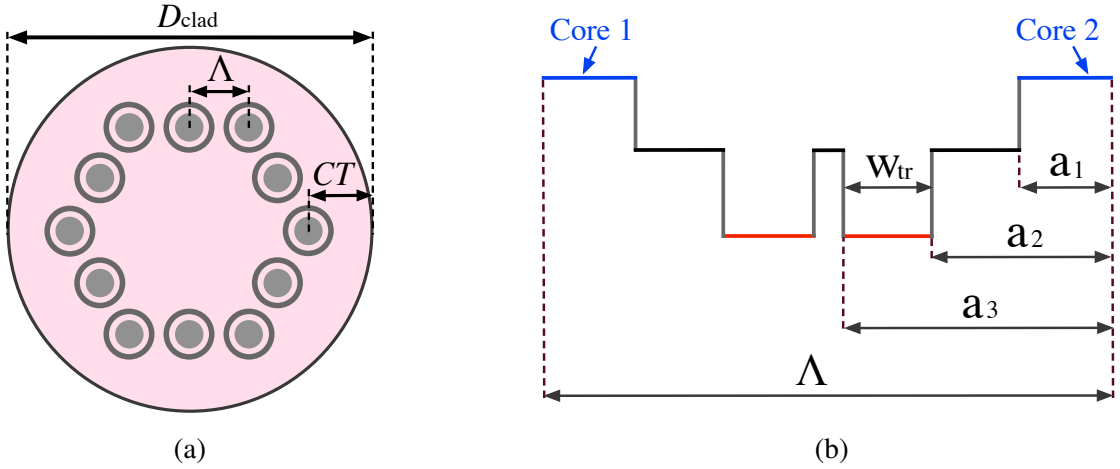

(a) (b)

Figure 3.5: (a) Cross-sectional view of a TA 12-core fiber with ORS and (b) refractive index profiles and core pitch for adjacent cores.

Table 3.2: Parameters for the XT calculation and numerical simulations

Parameters	TA (Trench-assisted)	SI (Step-index)	Units
a_1	4.5	4.5	μm
a_2/a_1	2	-	-
a_3/a_1	3	-	-
w_{tr}/a_1	1	-	-
n_0	1.45	1.45	-
Δ_1	0.35	0.35	%
Δ_2	$-0.35, -0.70$	-	%
R_b	140	140	mm
L	100	100	km

The trench width w_{tr} is limited by the core pitch and the distance between adjacent trenches since they should not overlap with each other, as shown in Fig. 3.5. The maximum cladding diameter (D_{clad}) is limited by mechanical reliability issues [29] since fibers with larger cladding diameter will experience larger tensions due to bending. To satisfy the limit of failure probability, the cladding diameter should be less than 225 μm [33]. The cladding thickness (CT), a distance between the cladding edge and the center of the outermost cores is assumed to be at least 30 μm for micro-bending loss considerations [34]. With these constraints and if the minimum distance between adjacent trenches is assumed to be 3 μm, the core pitch of a TA 12-core fiber with ORS as the one shown in Fig. 3.5(a), should be less than 39 μm. Thus, the maximum distance from the outer edge of trench to the core center, a_3, would be $(39-3)/2 = 18$ μm. With the other parameters listed in Table 3.2, the allowed trench width w_{tr} has to be less than $2a_1$ (or 9 μm), where $w_{tr} = 4.5$ μm is used in the table. The comparison of XT between analytical calculations and numerical simulations (both by non integrable expressions and FEM) for TA-MCFs is plotted in Fig. 3.6. It should be noted that the XT presented here is only between two adjacent cores for simplicity without assuming any core layout structure in MCFs. The fiber length and the bending radius are assumed to 100 km and 140 mm, respectively. The XT for a normal SI structure is also included for the XT comparison since it can be regarded as a special case of a TA structure with Δ_2 of 0%.

In order to check that the simplified analytical expression has good accuracy for a wide range of

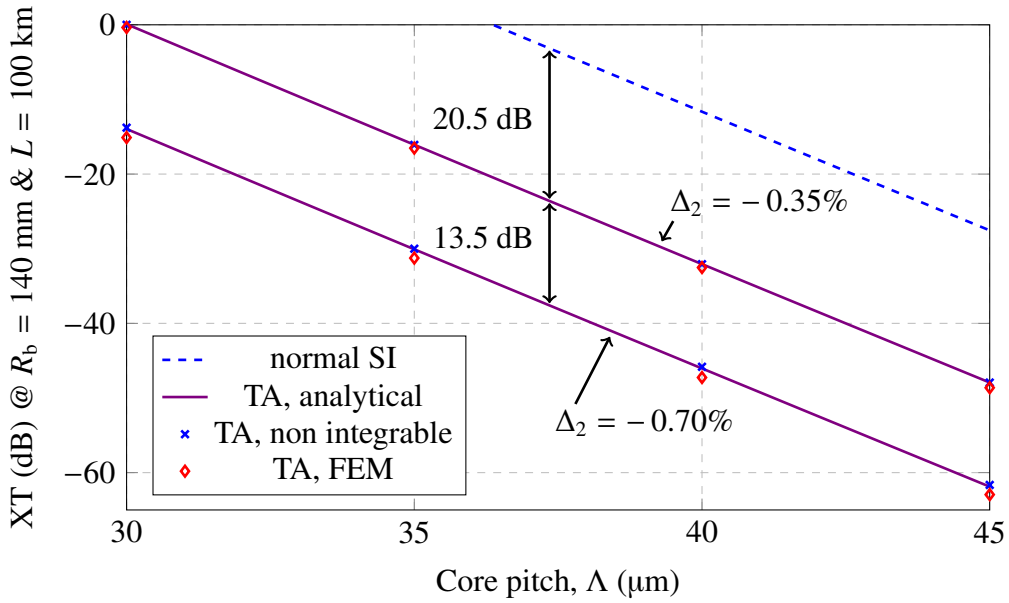

Figure 3.6: Crosstalk comparison between the analytical calculations and numerical simulations for a TA structure as a function of core pitch Λ at a wavelength of 1550 nm with a trench width equal to the core radius. The XT for a normal SI structure is also included.

fiber parameters, the XT comparison at Δ_2 of both -0.35% and -0.70% is included as the relative refractive index difference between the trench and the cladding of $\Delta_2 = -0.70\%$ is assumed to be the limit for regular VAD and OVD processes. The trench width should be large enough to reduce the XT and if the minimum trench width is set to be the same as a_1 as in Table 3.2, the corresponding core pitch would be $2a_3+3 = 2\times 3a_1+3 = 30$ μm, in which 3 μm is the minimum distance between adjacent trenches. The numerical simulations based on the non integrable expression of Eq. (3.9) and FEM are carried out at core pitches of 30, 35, 40 and 45 μm, while the XT curves calculated from the analytical expression Eq. (3.24) can be plotted continuously.

As can be seen from Fig. 3.6, the XT results calculated for the analytical expression and the non integrable expression agree very well, assuring that the approximation used to simplify the non integrable expression has very good accuracy. The XT simulated by FEM is always a little lower than the one obtained by the non integrable and the analytical expressions. For the case of Δ_2 of -0.35%, the maximum XT difference between the analytical expression and FEM is below 0.7 dB. For the case of $\Delta_2 = -0.70\%$, this difference is increased, but still below 1.5 dB, which is fairly small compared to the absolute value of XT as the typical target XT should be as low as -30 dB or even lower over 100 km. Thus, the analytical expression can be used to estimate XT without the

burden of numerical simulations based on FEM. As can be seen from Fig. 3.6, the XT curves based on the analytical expression at different values of Δ_2 appear to be parallel to each other. Referring to Eq. (3.36), it is found that the XT reduction in a TA structure compared to a normal SI is indeed core pitch independent.

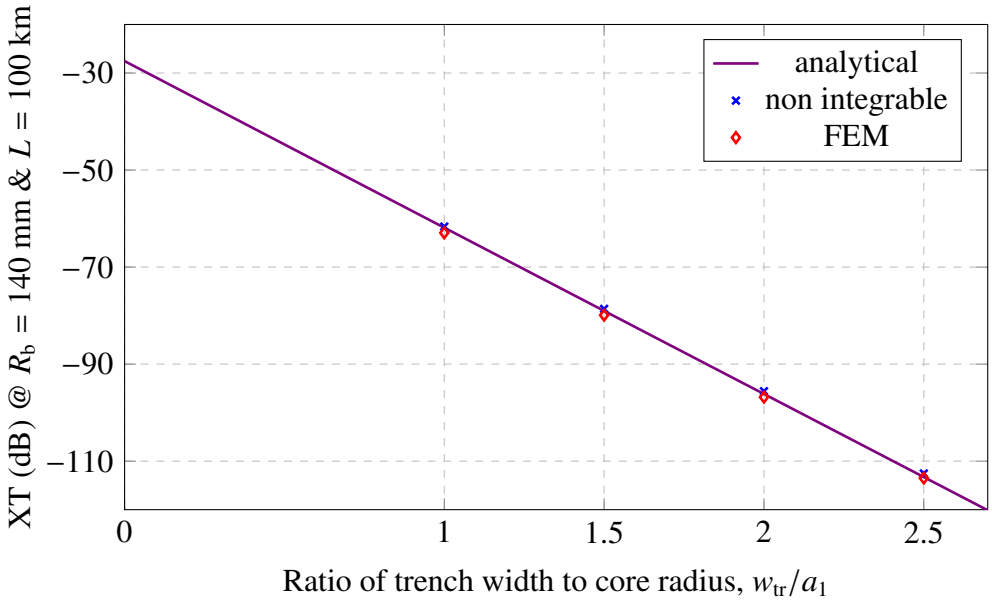

Figure 3.7: XT comparison between the analytical expression and the numerical simulations in a TA structure as a function of the ratio of trench width to core radius w_{tr}/a_1, at a wavelength of 1550 nm with a core pitch Λ of 45 μm and $\Delta_2 = -0.70\%$.

Since the trench width may be changed in TA-MCFs for different designs and core layout structures, it is also important to compare the XT based on the analytical expression and numerical simulations for different trench widths (or a ratio of the trench width to the core radius). As discussed before, the maximum trench width can be larger than the core radius depending on the allowed core pitch in high core density MCFs. The XT comparison is then extended to the case where w_{tr} is larger than the core radius a_1 as shown in Fig. 3.7, in which the relative refractive index difference between the trench and the cladding Δ_2 is set to be -0.70%. The numerical simulations based on the non integrable expression and FEM are performed and plotted for w_{tr}/a_1 =1.0, 1.5, 2.0 and 2.5, while the XT versus the ratio of the trench width to the core radius calculated from the analytical expression is plotted continuously. The XT at $w_{tr}/a_1 = 0$ corresponds to the case of a normal SI structure. The core pitch in this comparison is set to be 45 μm for all different ratios of trench width to core radius, and thus, the distance between adjacent trenches is different for dif-

ferent values of w_{tr}/a_1. With the maximum w_{tr}/a_1 of 2.5, the minimum distance between adjacent trenches can be calculated to be $45 - 2 \times (2 + 2.5)a_1 = 4.5$ μm, which still satisfies the requirement for the minimum distance between adjacent trenches of 3 μm.

Again, the XT results based on the analytical expression agree very well with the ones obtained by non integrable expression at different w_{tr}/a_1. The XT results simulated by FEM is still a little lower than the ones calculated by the analytical method, but the maximum difference is below 1.5 dB for w_{tr}/a_1 ranging from 1.0 to 2.5 as plotted in Fig. 3.7. The maximum w_{tr}/a_1 used in the comparison is 2.5, which should be sufficient in practical applications. By comparing with FEM results, it is confirmed that our analytical expression is valid even when fiber parameters such as Δ_2 decreases from 0 to -0.70% and trench width increases from 0 to as large as $2.5a_1$. It should be noted that the distance from the outer edge of 1st cladding to the core center is always set to be twice the core radius in the above XT comparison.

3.5 Comparison with Experimental Measurements

In addition to the comparison with numerical simulations, the XT results based on the analytical model and experimental measurements in TA-MCFs are also compared [71]. The structural parameters for fabricated TA 12-core fibers with ORS of 52 km and DRS of 50 km are listed in Table 3.3.

Table 3.3: Structural parameters of fabricated 12-core fibers

Parameters	ORS	DRS	Units
a_1	4.6	5.2	μm
a_2/a_1	2.0	2.0	-
w_{tr}/a_1	1.2	1.0	-
n_0	1.444	1.444	-
Δ_1	0.34	0.252	%
Δ_2	-0.75	-0.75	%

The cross-sectional views of fabricated TA 12-core fibers with ORS and DRS are shown in Fig. 3.8(a) and Fig. 3.8(b), respectively, where the core numbers are also marked. The cladding diameters,

cladding thicknesses and core pitches for the fabricated 12-core fibers with ORS and DRS are 225 μm, 38.9 μm, 36.8 μm and 230 μm, 37.7 μm, 44.6 μm, respectively.

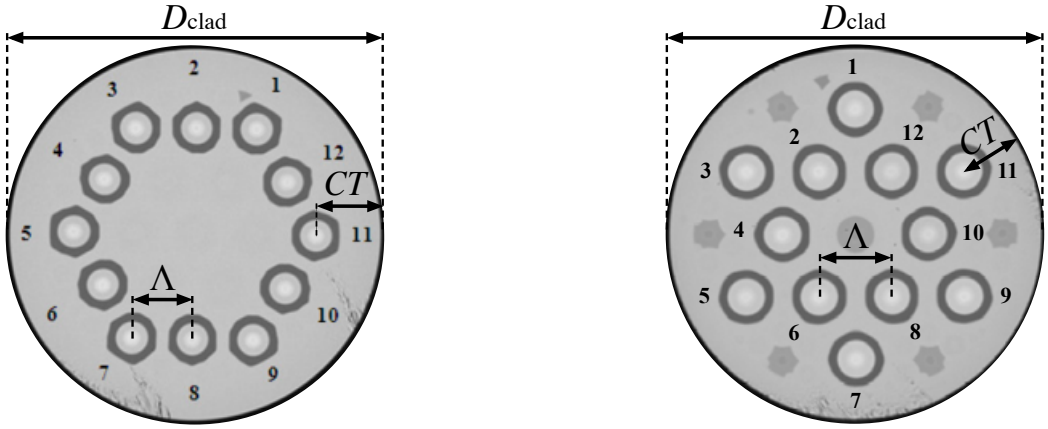

(a) (b)

Figure 3.8: Cross-sectional views of fabricated 12-core fibers with (a) ORS and (b) DRS.

Although it would be desirable to obtain measured XT for different bending radii, fiber lengths or wavelengths in order to compare the XT based on the analytical expression and experimental measurements, the easiest way is to compare XT at different wavelengths. Accordingly, Eq. (3.25) can be easily expressed as a function of wavelength for the XT comparison. The measured core-to-core XT in fabricated MCFs with ORS and DRS at two different wavelengths in C + L bands are shown in Fig. 3.9. The XT varies due to the deviations of fiber parameters induced through the manufacturing process and also due to the statistical nature of XT caused by the fiber bending and twist [72]. The average measured XT for the MCF with ORS is − 46.92 dB and − 38.84 dB at 1550 nm and 1625 nm, respectively, while for the MCF with DRS, the average measured XT is − 54.69 dB and − 46.06 dB at 1550 nm and 1625 nm, respectively.

The XT (red for ORS, blue for DRS) versus wavelength based on the analytical model is plotted in Fig. 3.10 using the fiber parameters of the fabricated 12-core fibers. The symbols "×" are the average values of the measured XT where the maximum and minimum XT (indicated by the bars) are also shown in the same figure.

As can be seen from the figure, the plotted XT curves based on the analytical model agree well with the average measured XT for both ORS and DRS. For ORS, the XT from the plot is only 0.40 dB and 0.42 dB higher than the average measured XT at 1550 nm and 1625 nm, respectively, while for DRS, the difference is 0.65 dB and 0.55 dB at 1550 nm and 1625 nm, respectively. As

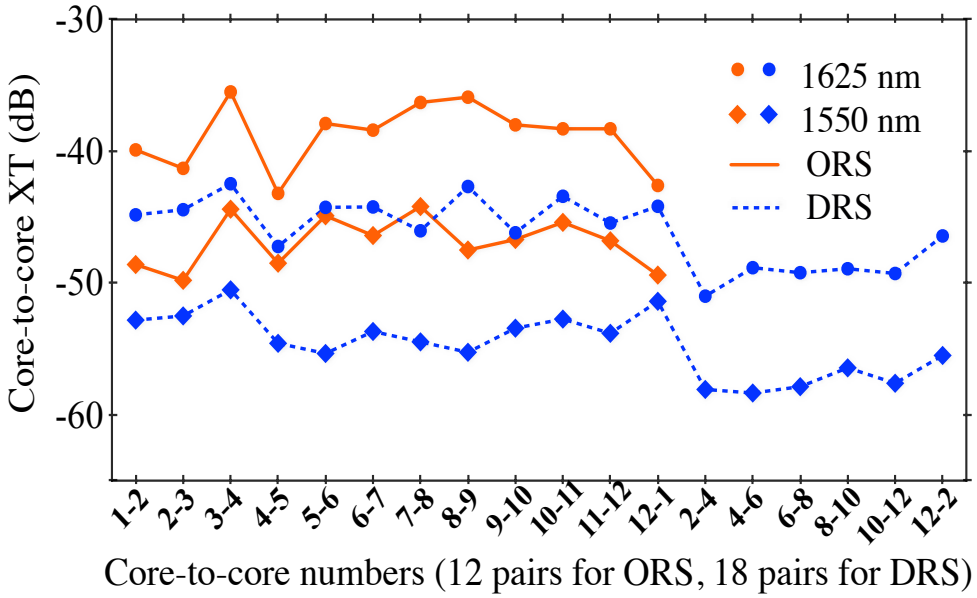

Figure 3.9: Measured XT at two different wavelengths for fabricated MCFs with ORS and DRS.

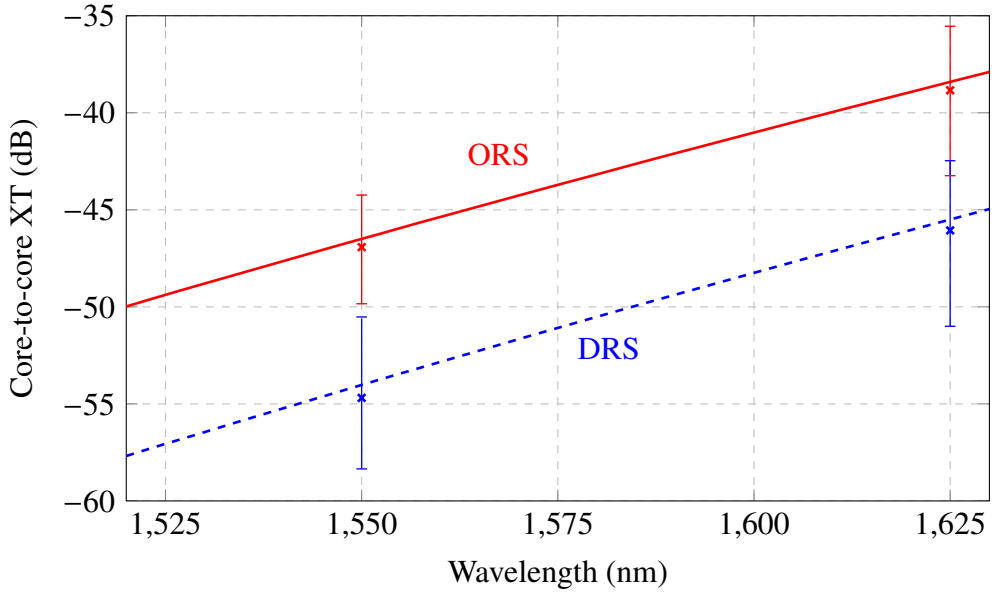

Figure 3.10: Comparison of XT versus wavelength between the analytical model and experimental measurements.

the typical target values of XT in low-XT MCFs are in the range of -30 dB to -40 dB, the XT difference between the analytical expression and experimental measurement is small enough to show that the analytical expression should be valid for designing low-XT MCFs.

3.6 Wavelength-dependent XT

One important issue in MCF transmission is the wavelength-dependent XT over the transmission band (e.g. C + L bands) [73, 74], which normally increases monotonously with wavelength as there will be larger electro-magnetic field overlaps at longer wavelengths between adjacent cores. Characterizing the wavelength-dependent XT in MCFs becomes important in designing future MCF-based networks and transmission systems, where different modulation formats or/and FECs may have to be used for different groups of wavelengths if there is large wavelength dependence. This adaptive modulation scheme will be provided by the next generation programmable DSPs supporting different modulation formats (QPSK, 8QAM, 16QAM etc) and FECs designed for Flexible Grid and future elastic optical networks. Moreover, the wavelength dependence of XT may become an essential parameter in establishing an optical path in the future MCF-based WDM networks consisting of multiple different MCFs with different wavelength dependence of XT.

The characteristics of wavelength-dependent XT in MCFs with a normal SI profile or a TA structure have not been well studied, and thus exact relationships between XT and wavelength were not well defined. Based on our analytical model for XT in TA-MCFs, we will investigate the wavelength dependence properties of XT in detail in this section.

3.6.1 Formulation in normal SI-MCFs

Referring to the Eq. (2.4), it is found that only the mode coupling coefficient κ_{pq} and the propagation constant β are wavelength-dependent.

For the mode coupling coefficient $\kappa_{pq}^{'}$ between two adjacent cores with normal SI profiles in Eq. (3.2), only V_1, U_1 and W_1 are related to wavelength, and thus should be expressed as a function of wavelength. V_1 can be expressed as C/λ, where $C = 2\pi a_1 n_1 (2\Delta_1)^{1/2}$, which is wavelength-independent. U_1 and W_1 can also be expressed as a function of wavelength by relating it to V_1, where $W_1 = 1.1428V_1 - 0.996$. Thus

$$\kappa_{pq}^{'} = \frac{\sqrt{\Delta_1}}{a_1}\frac{2.28\lambda^2 C - 0.99\lambda^3 - 0.31\lambda C^2}{C^3 K_1^2(1.1428C/\lambda - 0.996)}\exp\Big(0.996\frac{\Lambda}{a_1}\Big) \times \sqrt{\frac{\pi a_1}{(1.1428C/\lambda - 0.996)\Lambda}}\exp\Big(-\frac{1.1428C}{\lambda}\frac{\Lambda}{a_1}\Big). \tag{3.29}$$

Within the wavelength range of 1260 nm to 1620 nm, the terms in the above equation such as $2.28\lambda^2 C - 0.99\lambda^3 - 0.31\lambda C^2$, $1/(1.1428C/\lambda - 0.996)^{1/2}$ and $\exp[-1.1428C\Lambda/(\lambda a_1)]$ all increase as the wavelength increases, while $1/K_1^2(1.1428C/\lambda - 0.996)$ decreases. Since the increasing rate of $\exp[-1.1428C\Lambda/(\lambda a_1)]$ is much higher than the decreasing rate of $1/K_1^2(1.1428C/\lambda - 0.996)$, the mode coupling coefficient increases exponentially with wavelength.

The relative XT, defined as the XT difference (in dB) between λ and the lower end of C band λ_0 (i.e. 1530 nm), can then be expressed as

$$\Delta XT_{dB}^{'} = 10\log_{10}\frac{XT_{\mu}^{\lambda}}{XT_{\mu}^{\lambda_0}} = 10\log_{10}\left[\left(\frac{\kappa_\lambda}{\kappa_{\lambda_0}}\right)^2\frac{\beta_{\lambda_0}}{\beta_\lambda}\right], \tag{3.30}$$

where XT_{μ}^{λ} and $XT_{\mu}^{\lambda_0}$, κ_λ and κ_{λ_0}, β_λ and β_{λ_0} are the mean XT, mode coupling coefficients and propagation constants at a wavelength of λ and λ_0, respectively.

As $10\log_{10}(\beta_{\lambda_0}/\beta_\lambda)$ is very small being around 0.25 dB for $\lambda_0 = 1530$ nm and $\lambda = 1620$ nm with the parameters used in this work, it is ignored for simplicity.

Eventually,

$$\begin{aligned}\Delta XT_{dB}^{'} &\approx 10\log_{10}\left[K\exp\Big(2.2856\frac{C}{\lambda_0}\frac{\lambda-\lambda_0}{\lambda}\frac{\Lambda}{a_1}\Big)\right] \\ &\approx 10\log_{10}K + 19.85\,\pi n_1\sqrt{2\Delta_1}\frac{\Delta\lambda}{\lambda\lambda_0}\Lambda,\end{aligned} \tag{3.31}$$

where K ($0 < K < 1$) is a coefficient which depends on V_1 and $\Delta\lambda$, and can be approximated to be $(1 - 0.001256\Delta\lambda)^4$ as in this work with the accuracy of within $\pm 0.3\%$. $\Delta\lambda = \lambda - \lambda_0$ is the wavelength difference between λ and λ_0 (or transmission bandwidth) where $\lambda_0 = 1530$ nm is the shortest wavelength of the transmission band (i.e. C + L bands).

The slope of relative XT (in dB/nm) in normal SI-MCFs over the transmission band can then be calculated as

$$S^{'} = \frac{\Delta \mathrm{XT}^{'}_{\mathrm{dB}}}{\Delta\lambda} = \frac{10\log_{10} K}{\Delta\lambda} + 19.85\,\pi n_1 \sqrt{2\Delta_1}\frac{\Lambda}{\lambda\lambda_0}. \tag{3.32}$$

3.6.2 Formulation in TA-MCFs

Assuming the same core pitch, bending radius and fiber length for MCFs both in a normal SI structure and a TA structure, the XT between two adjacent cores in homogeneous TA-MCFs can be simplified to

$$\mathrm{XT}^{''}_{\mu} = \mathrm{XT}^{'}_{\mu}\,\Gamma \exp\Big[-4(W_2 - W_1)\frac{w_{\mathrm{tr}}}{a_1}\Big], \tag{3.33}$$

where $\mathrm{XT}^{''}_{\mu}$ and $\mathrm{XT}^{'}_{\mu}$ are the mean XT for MCFs with a TA structure and a normal SI structure, respectively.

As Γ is related to W_1 and W_2, it is also wavelength-dependent. The value of $10\log_{10}(\Gamma_\lambda/\Gamma_{\lambda_0})$ is very small being around -0.23 dB over the entire C + L bands with the parameters used in this work, which happens to be very close to $10\log_{10}(\beta_{\lambda_0}/\beta_\lambda)$. Interestingly, the effects of these terms cancel out as $0.25 + (-0.23) = 0.02$ dB.

Similarly, the relative XT (in dB) for homogeneous TA-MCFs can then be written as

$$\Delta \mathrm{XT}^{''}_{\mathrm{dB}} = \Delta\lambda \times S^{''}, \tag{3.34}$$

where $S^{''}$ is the slope of relative XT (in dB/nm) in TA-MCFs.

And

$$S^{''} \approx \frac{10\log_{10} K}{\Delta\lambda} + 19.85\,\pi n_1 \sqrt{2\Delta_1}\frac{\Lambda + 1.75A_{\mathrm{m}}w_{\mathrm{tr}}}{\lambda\lambda_0}, \tag{3.35}$$

where A_{m} is an m-dependent coefficient and it is 0.309, 0.607 and 0.867 for $m = 1$, 2 and 3, respectively. The values of A_{m} can be obtained from Table 3.1.

The additional term in Eq. (3.35) compared to Eq. (3.32) is $1.75A_{\mathrm{m}}w_{\mathrm{tr}}$ originating from the TA structure. As A_{m} is positive, a higher slope of relative XT is expected for TA-MCFs as compared to normal SI-MCFs.

3.6.3 Results and discussions

The XT versus wavelength over the C + L bands based on the analytical expression [75] and the numerical simulations in TA-MCFs are plotted in Fig. 3.11. The fiber structural parameters used for the comparison are listed in Table 3.4 and the core pitch is 35 μm.

Table 3.4: Fiber structural parameters for relative XT comparison

Parameters	TA (Trench-assisted)	SI (Step-index)	Units
a_1	4.5	4.5	μm
a_2/a_1	2	-	-
w_{tr}/a_1	1	-	-
Δ_1	0.35	0.35	%
Δ_2	$-0.35, -0.70, -1.05$	-	%

As can be seen from Fig. 3.11, the XT obtained by FEM-based numerical simulations is slightly lower than the one by the analytical expression. For the case of $\Delta_2 = -0.35\%$, the maximum XT difference between the analytical expression and FEM is less than 0.7 dB, while for the case of $\Delta_2 = -0.70\%$, the difference is increased, but is still less than 1.5 dB. The relative XT is plotted with respect to wavelength in Fig. 3.12. Both results based on numerical simulations and the analytical expression are compared so as to verify the accuracy of the analytical expression for the relative XT in TA-MCFs. The relative XT in a normal SI structure obtained by the analytical expression is also included.

As can be seen from Fig. 3.12, the FEM-based relative XT is 0.16 dB and 0.14 dB higher than the one by the analytical expression at 1620 nm for Δ_2 of -0.35% and -0.70%, respectively. The actual values of relative XT in normal SI-MCFs are around 0.25 dB higher than the one plotted here since the term $10\log_{10}(\beta_{\lambda_0}/\beta_\lambda)$ is dropped. For the case of TA-MCFs, the actual values are almost the same as the ones plotted here due to the cancellation effect of $10\log_{10}(\beta_{\lambda_0}/\beta_\lambda)$ and $10\log_{10}(\Gamma_\lambda/\Gamma_{\lambda_0})$. As can be seen from the figure, the slope of relative XT in TA-MCFs at $\Delta_2 = -0.35\%$ is slightly higher than the one in normal SI-MCFs, and it increases even further as $|\Delta_2|$ increases; by increasing $|\Delta_2|$ from 0.35% to 0.70%, the relative XT slope increases from 0.091 dB/nm to 0.099 dB/nm and is further increased for $|\Delta_2| = 1.05\%$.

The relative XT for MCFs with different number of cores is calculated based on the analytical

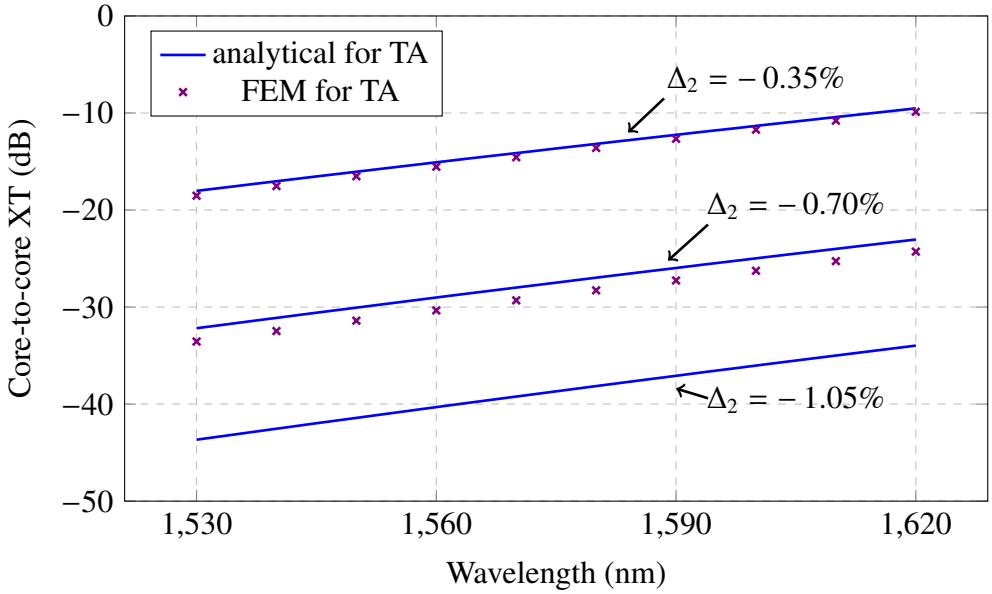

Figure 3.11: Core-to-core XT versus wavelength: comparison between the analytical expression and the numerical simulations in TA-MCFs with the bending radius and the fiber length of 140 mm and 100 km, respectively.

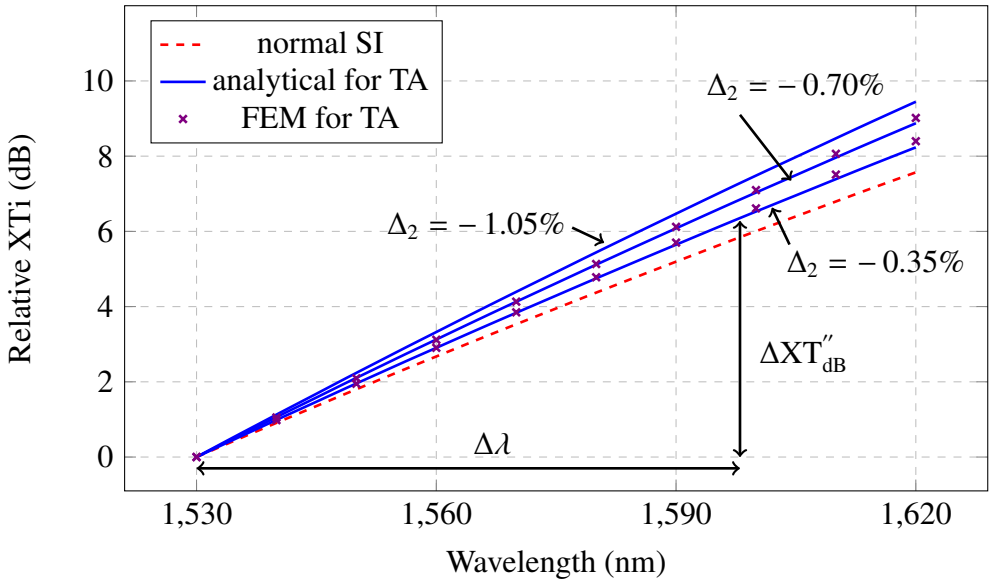

Figure 3.12: Relative XT versus wavelength: comparison between the analytical expression and FEM-based numerical simulations in MCFs with a TA structure.

expression as shown in Fig. 3.13, using the fiber parameters from Table 3.4 with $\Delta_2 = -0.70\%$. The relative XT in higher-count MCFs is reduced as compared to a 7-core fiber due to the reduced core pitch under the cladding diameter and cladding thickness constraints and is 13.5 dB, 12 dB, 10.5 dB and 7.3 dB in 7-core, 12-core, 19-core and 30-core fibers, respectively.

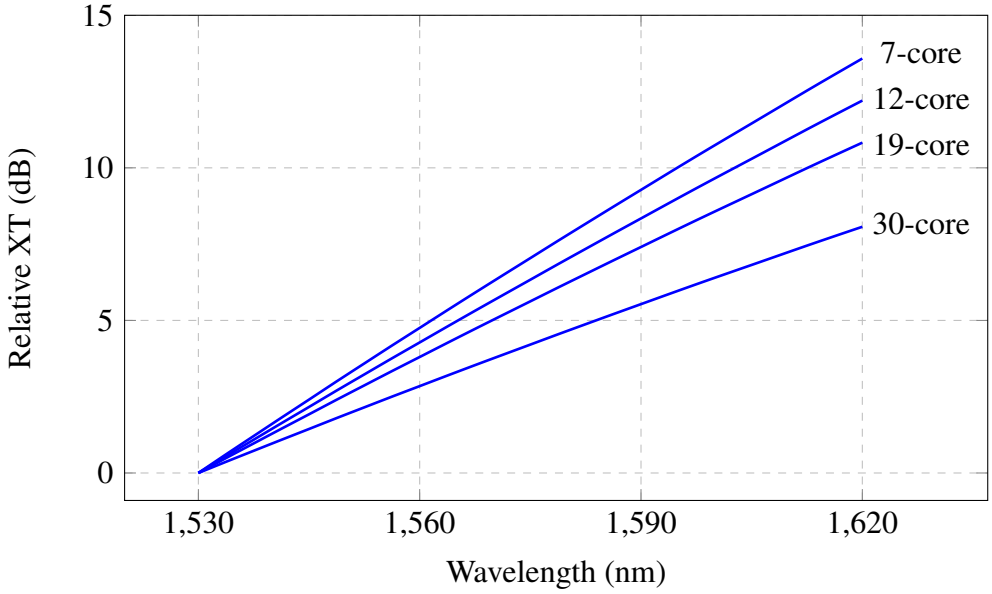

Figure 3.13: Relative XT in 7-core, 12-core, 19-core and 30-core fibers with corresponding core pitches of 50, 45, 40 and 30 μm, respectively.

The relative XT (in dB) is independent of bending radius R_b and fiber link length L as it is a logarithm of the ratio of the XT (refer to Eq. (2.4)) at λ to the one at λ_0. It should also be noted that the relative XT does not depend on core radius a_1, but is almost proportional to core pitch Λ. The relative XT is plotted as a function of core pitch in Fig. 3.13 to show the linear relationship between relative XT (in dB) and core pitch for a normal SI structure and TA structures with Δ_2 of -0.35%, -0.70% and -1.05%.

In addition to the comparison with numerical simulations, the results based on the analytical expression and experimental measurements for relative XT in TA-MCFs are also compared. The core pitches for 12-core fibers with ORS and DRS that were used for experimental measurements are 36.8 μm and 44.6 μm, respectively. The core-averaged relative XT is 8.08 dB and 8.63 dB from 1550 nm to 1625 nm for MCFs with ORS and DRS, with slopes of 0.1077 dB/nm and 0.1151 dB/nm, respectively. The slopes of relative XT from the measurements and the analyt-

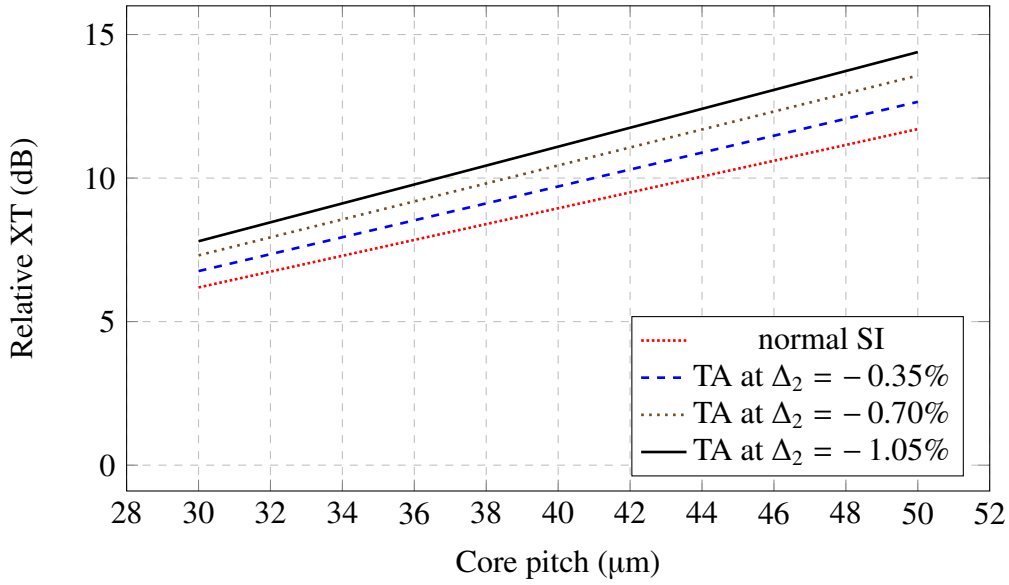

Figure 3.14: Relative XT as a function of core pitch in TA-MCFs and normal SI-MCFs, over the whole C + L bands.

ical calculation agree well (0.1077 dB/nm by the measurement results versus 0.1069 dB/nm by analytical calculation for ORS and 0.1151 dB/nm by the measurement results versus 0.1123 dB/nm by analytical calculation for DRS), which again confirms the accuracy of the analytical expressions for the relative XT and its slope in TA-MCFs.

3.7 Other XT Properties

3.7.1 XT reduction amount versus trench width

Using Eq. (3.26) [75], the XT reduction amount (> 0 dB) in a TA structure compared to a normal SI structure can be expressed as

$$\Delta\mathrm{XT} = \mathrm{XT}'_{\mathrm{dB}} - \mathrm{XT}''_{\mathrm{dB}} \approx 17.4\,(W_2 - W_1)\frac{w_{\mathrm{tr}}}{a_1} - 10\log_{10}\Gamma. \tag{3.36}$$

As can be seen from the above equation, the trench width has a direct effect on the XT reduction amount in a TA structure. The comparison between the analytical model and FEM-based numerical simulations in the previous sections deal with the absolute XT values in TA-MCFs instead of XT

reduction amount in a TA structure as compared to a normal SI structure. Here we compare the XT reduction amount based on two different methods. The main fiber structural parameters for this comparison are listed in Table 3.2. The comparison for the XT reduction amount as a function of the ratio of trench width to core radius is shown in Fig. 3.15 for a core pitch of 45 μm and a relative refractive index difference between the trench and the cladding Δ_2 of -0.35% and -0.70%. The FEM-based numerical simulations were performed at $R_{tr} = w_{tr}/a_1$ =1.0, 1.5, 2.0 and 2.5. $R_{tr} = 0$ corresponds to MCFs with a normal SI structure.

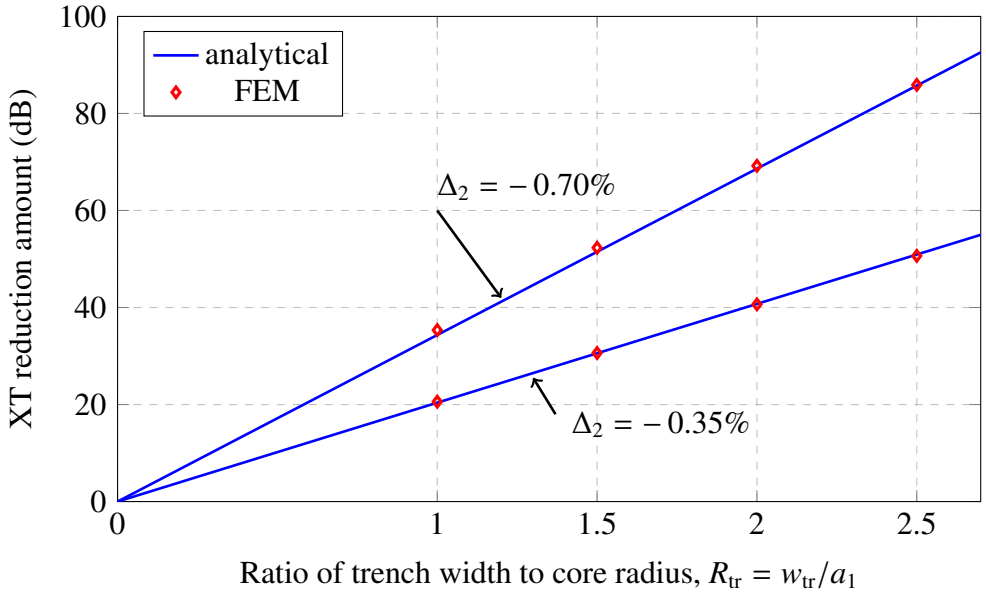

Figure 3.15: Comparison: XT reduction amount comparison as a function of $R_{tr} = w_{tr}/a_1$ (a ratio of trench width to core radius) between the analytical expression and numerical simulations at 1550 nm, with a core pitch Λ of 45 μm.

As can be seen from Fig. 3.15, the XT reduction amount using the analytical model and those obtained by FEM-based numerical simulations agree very well. The XT reduction amount based on numerical simulations are a little larger than the one based on analytical model. The maximum difference is around 1.0 dB at $R_{tr} = 1$ with $\Delta_2 = -0.70\%$. It can also be seen that the XT reduction amount increases almost linearly with R_{tr}. The linear property can be explained by Eq. (3.36), in which Γ has very weak dependence on the trench width and the the XT reduction amount can be treated as a linear function of the trench width. The slopes are around 20.4 dB and 34.3 dB per R_{tr} for Δ_2 of -0.35% and -0.70%, respectively. Thus, by increasing the trench width from $w_{tr} = a_1$ to $w_{tr} = 2a_1$, XT can be further reduced by 20.4 dB and 34.3 dB for Δ_2 of -0.35% and

-0.70%, respectively. It should be noted that trench width cannot be increased endlessly since the cable cutoff wavelength becomes longer when the trench width increases. For instance, with Δ_2 of -0.70%, the maximum trench width is $1.56a_1$ such that the single mode operation is guaranteed in the C band with a corresponding cable cutoff wavelength of 1530 nm.

3.7.2 XT reduction amount versus trench depth

In addition to increasing the trench width, the XT in TA-MCFs can also be reduced by adopting a deeper trench (i.e., larger $|\Delta_2|$).

With Eq. (3.36), the XT reduction amount can also be written as

$$\Delta\mathrm{XT} \approx 17.4\,[(mV_1^2 + W_1^2)^{1/2} - W_1]R_{\mathrm{tr}} - 10\log_{10}\Gamma. \tag{3.37}$$

With this equation, the XT reduction amount ΔXT, can be calculated and plotted with respect to $m = |\Delta_2|/\Delta_1$ as shown in Fig. 3.16. The ratio of trench width to core radius, R_{tr}, is chosen as 1, and the core pitch is set at 45 μm as in the previous section. The FEM-based numerical simulations were performed at $m = 1 \sim 10$ where only integers are considered.

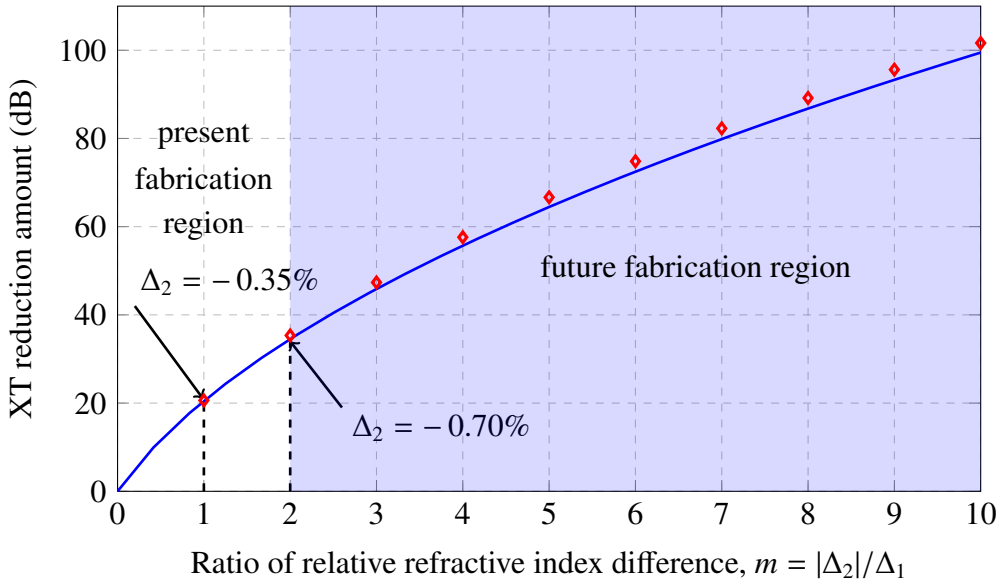

Figure 3.16: Comparison: XT reduction amount as a function of $m = |\Delta_2|/\Delta_1$ between the analytical model and numerical simulations, at 1550 nm, with $R_{\mathrm{tr}} = w_{\mathrm{tr}}/a_1 = 1$, $a_2 = 2a_1$ and a core pitch Λ of 45 μm.

As can be seen from the figure, the results based on the analytical model and FEM agree very well. The XT reduction amount increases with the ratio of relative refractive index difference m. This can be readily explained as a deeper trench results in stronger mode confinement, which reduces the mode overlap between adjacent cores. The slope of the curve decreases with m due to the square root nature of $(mV_1^2 + W_1^2)^{1/2}$ in Eq. (3.37). The ratio m is taken over a wide range, for instance from 1 to 10, where $m = 10$, corresponds to $|\Delta_2| = 3.50\%$. It should be noted that the cable cutoff wavelength also becomes longer when the trench becomes deeper. Compared to a normal SI structure, the XT can be reduced by as large as 98 dB by adding a TA structure with trench depth (Δ_2) of -3.50%. Such deep trench is very challenging to achieve since $\Delta_2 = -0.70\%$ might be the limit for using regular VAD and OVD processes. At $\Delta_2 = -0.35\%$, the XT reduction amount is around 20.5 dB, and further XT reduction of 14 dB can be achieved with $\Delta_2 = -0.70\%$.

Other techniques for further reducing Δ_2 including a hole-assisted structure [57] and nanoStructures [76]. The process for making hole-assisted fibers is much more complex than conventional fiber manufacturing processes. Compared to hole-assisted structure, nanoStructures technology is fully compatible with standard SMFs and can be manufactured with a standard OVD process [76]. If nanoStructures is adopted in MCFs, a big reduction of XT can be expected because the $|\Delta_2|$ in nanoStructures can be as large as a few percent depending on the void fill fraction. As shown in Fig. 3.18, if $|\Delta_2|$ is increased from 0.70% to 1.40%, further XT reduction of around 21 dB is possible. It should be noted that an increase of $|\Delta_2|$ or w_{tr}/a_1 might result in a longer cable cutoff wavelength when the core pitch is small since the mode is strongly confined in TA-MCFs especially in the center core of MCFs with a hexagonal close-packed structure.

If the ratio of relative refractive index difference m and the ratio of trench width to core radius w_{tr}/a_1 are fixed, XT in TA-MCFs can be reduced by increasing V_1, as can be seen from Table 3.1. Since V_1 is the V number at the transmission wavelength, the theoretical cutoff wavelength (at which, $V_1 = 2.405$) should be shifted towards the lower end of C band (1530 nm). In deployed systems, a cable cutoff wavelength is practically used, and it can be longer than the theoretical cutoff wavelength depending on the trench depth, trench width and the core pitch. If the cable cutoff wavelength (which must be smaller than 1530 nm if both C + L bands are used) is longer than theoretical cutoff wavelength, then V_1 has to be less than 2.405, which is not good for XT reduction if the XT reduction is achieved by only increasing V_1.

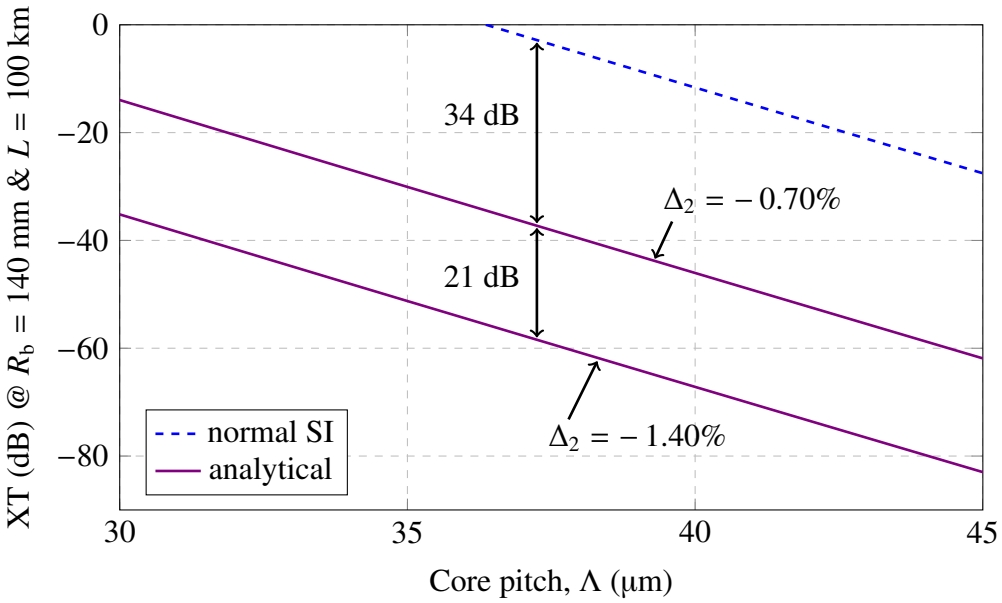

Figure 3.17: Further reduction of XT versus core pitch by decreasing Δ_2 from -0.70% to -1.40% based on the analytical expression in a TA structure at 1550 nm with the trench width equal to the core radius.

3.7.3 XT dependence on core pitch

The relationship between XT'_{dB} in normal SI-MCFs and the core pitch is almost linear. This can be explained by putting the analytical expression of the mode coupling coefficient κ'_{pq} into Eq. (2.4) and expressing XT in dB. In addition, the difference between XT'_{dB} and XT''_{dB} almost does not depend on core pitch, as can be seen from Eq. (3.36) where the term Γ has very little dependence on core pitch. Thus, XT''_{dB} in TA-MCFs can also be regarded as a linear function of core pitch. The slope of XT with respect to core pitch (dB/μm) in both normal SI-MCFs and TA-MCFs can be written by the same following expression [77] as

$$S = \frac{\Delta XT_{dB}}{\Lambda_0 - \Lambda} = -20\,(\log_{10} e)\frac{W_1}{a_1} - \frac{20\log_{10}(\Lambda/\Lambda_0)}{\Lambda - \Lambda_0}, \tag{3.38}$$

where ΔXT_{dB} (> 0) is the difference of XT in dB at core pitches of Λ_0 and Λ, where $\Lambda_0 < \Lambda$.

The XT is plotted as a function of core pitch using the analytical expression and FEM-based numerical simulations for Δ_2 of -0.35% in Fig. 3.18 using the structural parameters from Table 3.2. The numerical simulations were carried out at core pitches of 30, 35, 40 and 45 μm. The maximum XT difference between the analytical expression and FEM occurs at a core pitch of 45 μm

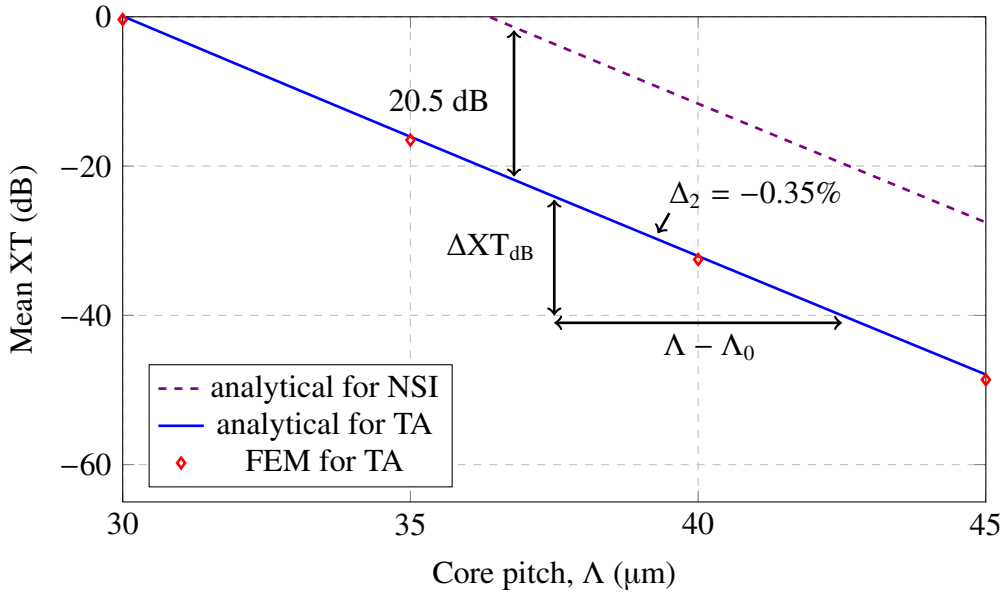

Figure 3.18: XT as a function of core pitch, based on analytical expression and numerical simulations, at 1550 nm. XT in MCFs with normal SI structure is also included.

where the result from analytical expression is around 0.7 dB higher than the one based on FEM. The slope of XT against core pitch can be estimated by Eq. (3.38) with high accuracy, which is around − 3.2 dB/μm. This number is useful in estimating XT if core pitch is increased or reduced. For instance, if the core pitch is increased from 35 μm to 40 μm, XT reduction of 16 dB is expected. It is interesting to mention that the slope of XT against core pitch does not depend on the trench structure. Thus, an increase of core pitch by the same amount results in same XT reduction amount in both normal SI-MCFs and TA-MCFs.

3.8 Summary

An analytical expression for the mode coupling coefficient between two adjacent cores in homogeneous TA-MCFs is derived, which has a very simple relationship with the mode coupling coefficient in homogeneous normal SI-MCFs. With this analytical expression, an analytical model for XT in TA-MCFs is formulated. Using the analytical model, the XT in MCFs with a TA structure can be calculated directly without the need of numerical simulations. The XT reduction amount (in dB) in a TA structure compared to a normal SI structure is also formulated to be a simple expression.

The analytical model can be used to quickly estimate the XT reduction amount and analyze the relationship between XT and fiber structural parameters in a TA structure. Comparison of XT results obtained by the analytical model and numerical simulations confirms that the analytical model has very good accuracy, and thus provides a very useful and powerful tool in designing low-XT and high-count MCFs. With the analytical model, XT properties such as wavelength-dependent XT, XT reduction amount versus trench width and trench depth, XT dependence on core pitch are analyzed. Based on the relationship, it is found that the XT in TA-MCFs is ultimately limited by the relative refractive index difference between the trench and the cladding, and the trench width.

□ End of chapter.

Chapter 4

Optimization of Core Positions in MCFs

4.1 Introduction

Cores in an MCF can be arranged using different core layout structures. For instance, a hexagonal close-packed structure (HCPS) is most widely used for MCFs with 7 cores and 19 cores. Earlier works on MCFs design are exclusively 7-core fibers with HCPS [31, 57, 72, 78, 79] as shown in Fig. 4.1. In terms of refractive index profiles, MCFs in Fig. 4.1(a), Fig. 4.1(b) adopt a normal SI profile and a hole-assisted structure, while those in Fig. 4.1(c) and Fig. 4.1(d) adopt a TA structure.

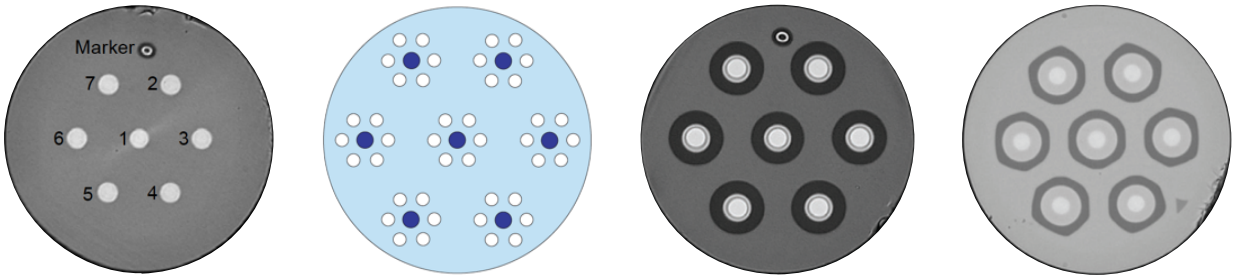

(a) [72] (b) [57] (c) [78, 79] (d) [31]

Figure 4.1: Cross-sectional views of 7-core fibers from earlier works.

With the introduction of different XT reduction techniques, especially a TA structure, the number of cores in an MCF has been increased while the XT is still kept low enough such that higher order modulation formats can be adopted for long-distance and high-capacity transmission sys-

tems. A 12-core fiber with an one-ring structure (ORS) was used in the first one Pbit/s transmission experiment [44] with its cross-sectional view shown in Fig. 4.2(a). Another 12-core fiber with a dual-ring structure (DRS) was used for a PDI transmission scheme [62, 66] as shown in Fig. 4.2(b). For 12-core fibers, cores can also be arranged using a square-lattice structure (SLS) as show in Fig. 4.2(c).

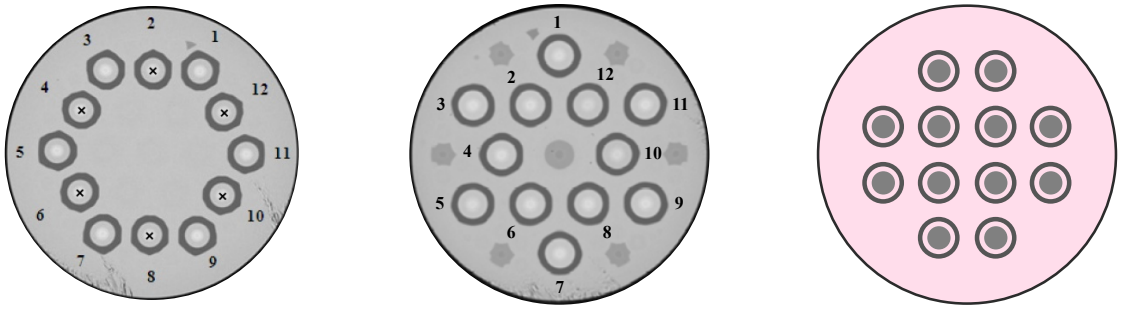

(a) (b) (c)

Figure 4.2: Cross-sectional views of 12-core fiber with (a) ORS [44], (b) DRS [62, 66] and (c) SLS.

The ORS was proposed to solve the two main issues in HCPS [43] which are

1. Core pitch limitation due to the cable cutoff wavelength lengthening of inner cores [31, 34]
2. Excessive XT degradation in inner cores [32]

As can be seem from Fig. 4.2(a), the center of MCF with ORS has a large empty area and thus, it would be worthwhile to investigate whether such a core layout structure is optimum in terms of XT. Such investigation is generally difficult based on numerical simulations as there is no intuitive way to determine how the cores should be arranged and numerical simulations can be done only after the core layout structure has been determined. Applying our analytical model in a 12-core fiber with ORS, we are able to search for new core positions with lower XT by moving 6 cores out of 12 cores. We then prove that DRS is a quasi-optimum core layout structure by the core positions movement based on ORS.

4.2 Principle of Core Positions Movement

The cross-sectional views of 6-core, 8-core and 10-core fibers with ORS are shown in Figs. 4.3(a), 4.3(b) and 4.3(c), respectively. Here we use the analytical model to find the new positions for XT

reduction. It should be noted that only MCFs with even number of cores (i.e. 6, 8, 10 and 12) are considered due to the symmetry requirement for core positions movement.

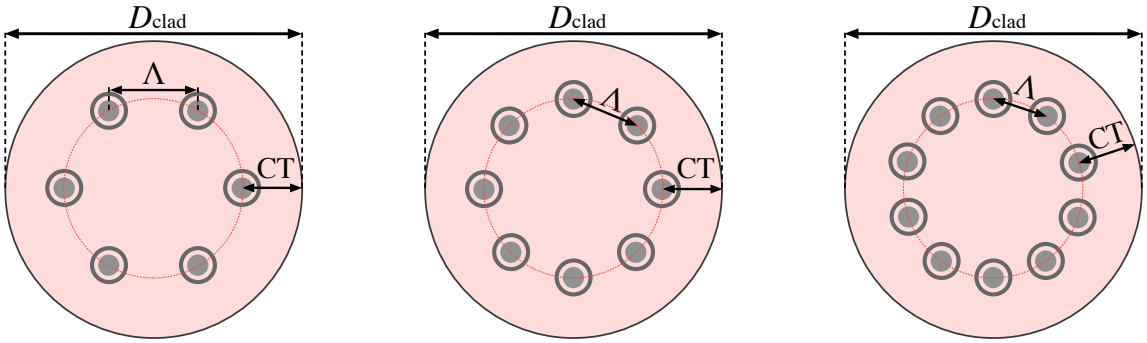

Figure 4.3: Cross-sectional views of (a) 6-core, (b) 8-core and (c) 10-core fibers with ORS.

In order to search for new core positions, the analytical expression for XT in TA-MCFs should be expressed as a function of core positions (related to core pitch). Using Eq. (2.4) and Eq. (3.24), the XT between two adjacent cores in TA-MCFs can also be expressed as

$$\mathrm{XT}''_{\mu} = M\frac{\Gamma}{\Lambda^2}\exp\Big(-\frac{2W_1\Lambda}{a_1}\Big), \tag{4.1}$$

where M does not depend on the core pitch, and it is expressed as

$$M = \frac{2\Delta_1}{a_1}\frac{U_1^4}{V_1^6 K_1^4(W_1)}\frac{\pi R_b L}{W_1\beta}\exp\Big[-4(W_2-W_1)\frac{w_{tr}}{a_1}\Big]. \tag{4.2}$$

The coordinate system for the core positions movement based on an MCF with ORS is shown in Fig. 4.4. The total number of cores N_{total} can be 6, 8, 10 or 12 etc and it can be calculated as $N_{total} = 2\pi/\theta$ where θ is the angle between two adjacent cores as illustrated in the figure. The red cores (named as B#) are sitting on the dotted red circle with its diameter of $2b = D_{clad} - 2CT$, and they are fixed at the current positions so that the requirement for CT due to the bending loss constraints [34] is always satisfied. The blue cores (named as A#) sitting on the dotted blue circle can be moved by the same amount towards the fiber center so that the red and blue cores are assigned in an interleaved manner. It should be noted that the blue cores are originally sitting on the red circle while the blue cores in the figure have already moved towards the center for illustrating core positions movement principle. For the case of A1, as it should have the same

distance to B1 and B2, it can only be moved along the y axis to find its new position. The distance from the center of the MCF to the center of red cores is b. The coordinates for A1, B2 and A3 are $(0,\ Y)$, $(b\sin\theta,\ b\cos\theta)$ and $(Y\sin 2\theta,\ Y\cos 2\theta)$, respectively, where Y is the distance from the center of A1 to the center of the MCF. Since the maximum D_{clad} is assumed to be 225 μm [33] so as to satisfy requirement due to failure probability and the minimum CT is assumed to be 30 μm for micro-bending loss constraints [34], the maximum b is calculated to be 82.5 μm.

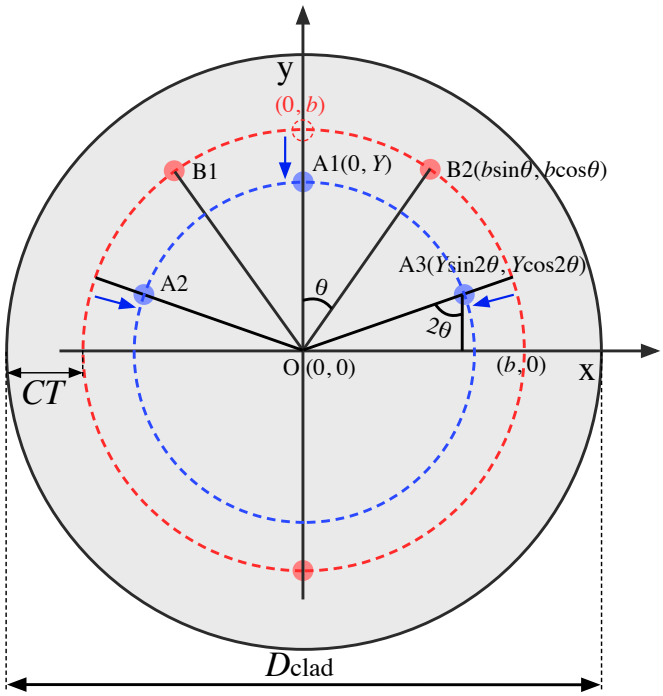

Figure 4.4: Coordinate system for core positions movement based on an MCF with ORS. D_{clad} is a cladding diameter and CT is a cladding thickness.

The core pitch Λ_1 between A1 and B2 (or B1) can be calculated as

$$\Lambda_1 = \sqrt{Y^2 - 2bY\cos\theta + b^2}. \tag{4.3}$$

The core pitch Λ_2 between A1 and A3 (or A2) is $2Y\sin\theta$. As B1, B2, A2 and A3 are the main contributors of XT for A1, the total XT for A1 (XT from 2 cores at Λ_1 and 2 cores at Λ_2) with a TA structure can be calculated as

$$\mathrm{XT}''_{\text{total}} = 2M\frac{\Gamma(\Lambda_1)}{\Lambda_1^2}\exp\Big(-\frac{2W_1\Lambda_1}{a_1}\Big) + 2M\frac{\Gamma(\Lambda_2)}{\Lambda_2^2}\exp\Big(-\frac{2W_1\Lambda_2}{a_1}\Big). \tag{4.4}$$

4.3 Results and Discussions

Since the core pitch in a 6-core fiber with ORS cannot be increased by moving the 3 blue cores towards the center of the MCF, 8, 10 and 12-core MCFs are considered for XT reduction by core positions movement. The corresponding core pitches in ORS MCFs with different number of cores are listed in Table 4.1. Other fiber parameters are the same as in Table 3.2 where only Δ_2 of -0.70% is considered. Instead of plotting absolute values of the XT, the XT improvement with the new core positions from ORS is plotted in Fig. 4.5.

Table 4.1: Geometrical parameters in ORS with different number of cores

N_{total}	θ	Λ_1	Λ_2
8	$\pi/4$	$(Y^2 - \sqrt{2}bY + b^2)^{1/2}$	$\sqrt{2}Y$
10	$\pi/5$	$[Y^2 - (1+\sqrt{5})bY/2 + b^2]^{1/2}$	$(10-2\sqrt{5})^{1/2}Y/2$
12	$\pi/6$	$(Y^2 - \sqrt{3}bY + b^2)^{1/2}$	Y

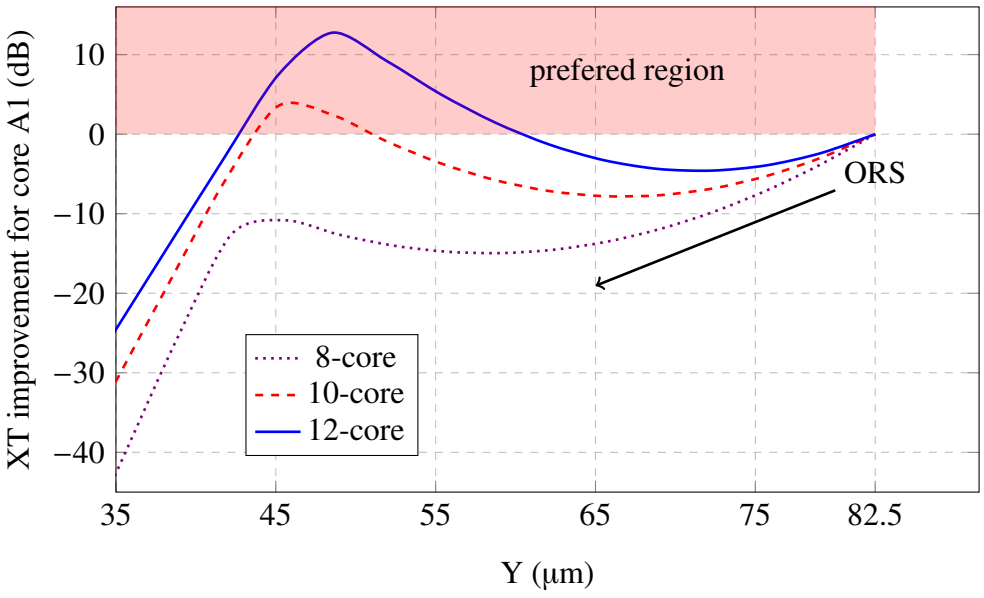

Figure 4.5: XT improvement for core A1 versus its position at 1550 nm.

As can be seen from the figure, for an 8-core fiber, the XT becomes larger (i.e. increased XT) by moving the blue cores towards the center. As the total number of cores increases in an one-ring

structured MCF, the space that can be utilized around the center of an MCF increases. In fact, the XT in 10-core and 12-core fibers can be improved by core positions movement at certain values of Y. The exact amount of improvement depends on the core position of A1. For instance, the highest XT improvement in a 10-core fiber is around 3.8 dB at $Y = 45.8$ μm, while for a 12-core fiber, it becomes around 12.7 dB at $Y = 48.7$ μm. It should be noted that the 12-core fiber used in this example is not the traditional hexagonal ORS as Fig. 4.2(a), it is actually a so-called "circular ORS" where all the cores are at the same distance to the center of the MCF.

It is concluded that if the total number of cores in ORS is equal to or more than 10, XT improvement can be achieved by moving half of the interleaved cores towards the center of the MCF. Since the first one Pbit/s MCF transmission experiment adopted a 12-core fiber with ORS [44], it would be worthwhile to investigate this special case for XT reduction by the core positions movement.

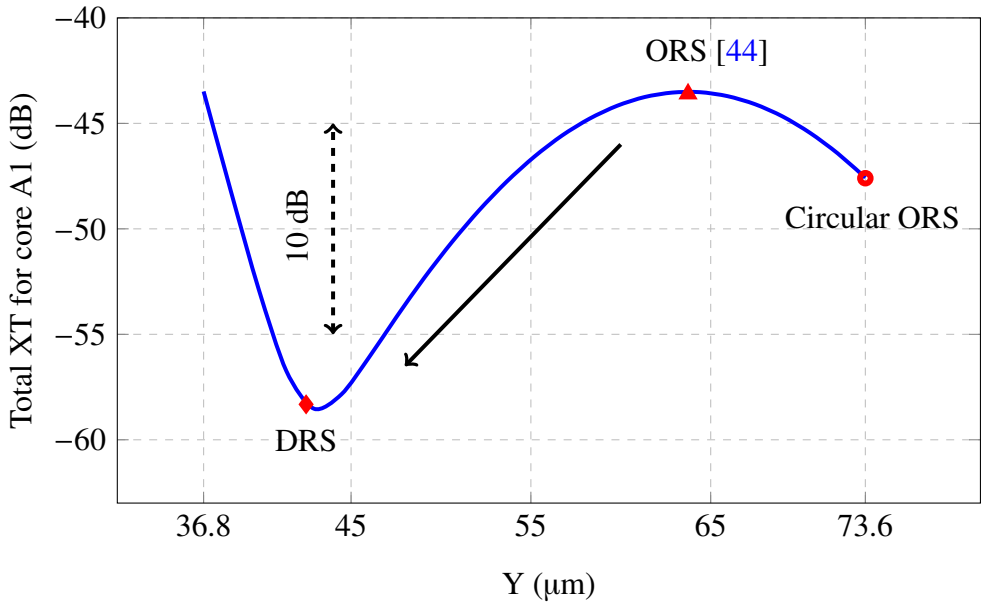

Figure 4.6: Total XT in core A1 at 1550 nm versus its position based on a 12-core fiber with ORS over the range $b/2 \leq Y \leq b$ ($b = 73.6$).

The bending radii for both fabricated MCFs are 155 mm while the fiber lengths are 52 km and 50 km for MCFs with ORS and DRS, respectively. Other fiber structural parameters of the two fabricated 12-core fibers are listed in Table 3.3. Using the fiber parameters in the 12-core fiber with ORS, b can be calculated as $D_{\text{clad}}/2 - CT = 73.6$ μm. The total XT in A1 is plotted with respect to Y as shown in Fig. 4.6. The marks ∘, △ and ⋄ correspond to "circular ORS" $(0, b)$, ORS $(0, \sqrt{3}b/2)$

and DRS $(0, b/\sqrt{3})$, respectively, where the total XT in A1 with hexagonal shape ORS [44] is the worst case over the plotted range. The XT can be reduced simply by moving A1 towards the edge of cladding (increasing Y from $\sqrt{3}b/2$ towards b) or towards the center of the MCF (decreasing Y from $\sqrt{3}b/2$ towards $b/2$). The minimum XT occurs at 43.20 μm, which corresponds to XT of -58.56 dB. In the special case when $\Lambda_1 = \Lambda_2$, Y equals $b/\sqrt{3} = 42.49$ μm, resulting in a new core arrangement,which is DRS. As 42.49 μm is very close to 43.20 μm which corresponds to minimum, the difference of XT between these two points is only 0.24 dB. DRS can be regarded as a quasi-optimum core layout. The amount of XT reduction from the hexagonal shape ORS to DRS is 14.82 dB. In other words, by adopting DRS, the transmission distance could be extended up to 30 times compared to ORS until the nonlinearity comes into play. It is interesting to note that the quasi-optimum position is always at $Y = b/\sqrt{3}$, which does not depend on the core radius or the trench structure.

Table 4.2: XT results obtained by the analytical model and FEM-based numerical simulations for different core layout structures

Core layout Structures	XT (dB)	
	analytical model	numerical simulations
ORS (hexagonal)	-43.50	-44.70
Circular ORS	-47.60	-48.80
DRS	-58.32	-59.57
Reduction From ORS to DRS	14.82	14.87

The numerical simulations for the worst XT (for the core with most adjacent cores) in different core layout structures are performed and the results are listed in Table 4.2. The XT difference between the analytical model and FEM-based numerical simulations is within 1.2 dB for three core layout structures (ORS, circular ORS and DRS). It should be noted that the XT reduction amount from ORS to DRS is almost the same for two different methods (14.82 dB by the analytical model versus 14.87 dB by the numerical simulations).

Fig. 4.7 shows how the hexagonal shape ORS changes to DRS by the core positions movement. It can be clearly seen that the core pitch is increased in DRS compared to ORS under the same cladding diameter and cladding thickness constraints. It should also be noted that the number of adjacent cores has been increased from 2 to 4 by shifting from ORS to DRS, but the XT reduction

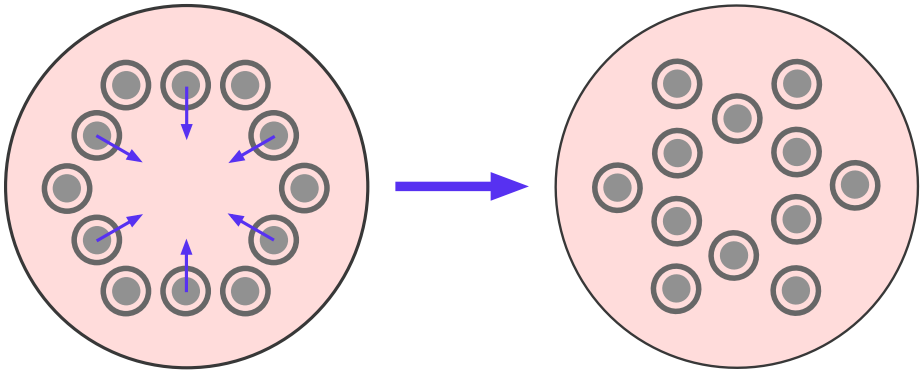

Figure 4.7: Cross-sectional views from ORS to DRS by the core positions movement.

effect induced by the increase in core pitch in DRS is more significant, resulting in lower overall XT for each core.

4.4 Summary

The analytical model for XT in TA-MCFs was successfully used to search for new core positions for XT reduction in non close-packed core layout structures, achieving much lower XT without changing other fiber parameters. Based on the method, we optimized the core positions in homogeneous TA 12-core fibers with ORS to achieve least XT and showed that DRS is the quasi-optimum design with corresponding XT reduction amount of more than 14 dB compared to ORS.

□ End of chapter.

Chapter 5

High-Count MCFs Design

5.1 Introduction

In order to increase the total capacity of SDM transmission systems, the number of cores in an MCF should be increased under the cladding diameter and cladding thickness constraints. The state-of-the-art SDM transmission with a total capacity of 2.15 Pbit/s was achieved by adopting a 64QAM modulation format over 10 THz bandwidth in a 31 km homogeneous 22-core fiber with a cladding diameter of 260 μm [47], where the highest aggregate inter-core XT was measured to be -45 dB/km. In order to further increase the number of cores in an MCF, the heterogeneous core arrangement where adjacent cores have different refractive index profiles, should be used as it can further reduce the inter-core XT compared to the homogeneous core arrangement. Recently, a 9.6 km heterogeneous 30-core fiber having 4 types of non-identical cores with a cladding diameter of 228 μm has been fabricated and reported with its XT of less than -40 dB over 100 km at 1550 nm [80]. It would be preferable, however, to use the homogeneous core arrangement as it would make the fiber design and manufacturing much simpler. Taking this consideration into account, a quasi-single-mode homogeneous 31-core fiber was designed and fabricated with fundamental mode XT of -38.4 dB over 11 km at 1550 nm with the projected XT of -28.8 dB over 100 km at 1550 nm [52].

The hexagonal close-packed structure (HCPS) has been widely used in MCFs due to its high core density and its simpler fabrication process than other structures, for instance, in 7-core fibers [32]

and 19-core fibers [40] as shown in Fig. 5.1(a) and Fig. 5.1(b), respectively.

Here we briefly investigate the effects of PDI for XT reduction in MCFs with HCPS. The cross-sectional views of 7-core and 19-core fibers with HCPS for bidirectional core assignment is shown in Fig. 5.2. It is interesting to note that there are two different kinds of core assignment schemes in 19-core fibers as shown in Fig. 5.2(b) and Fig. 5.2(c), respectively.

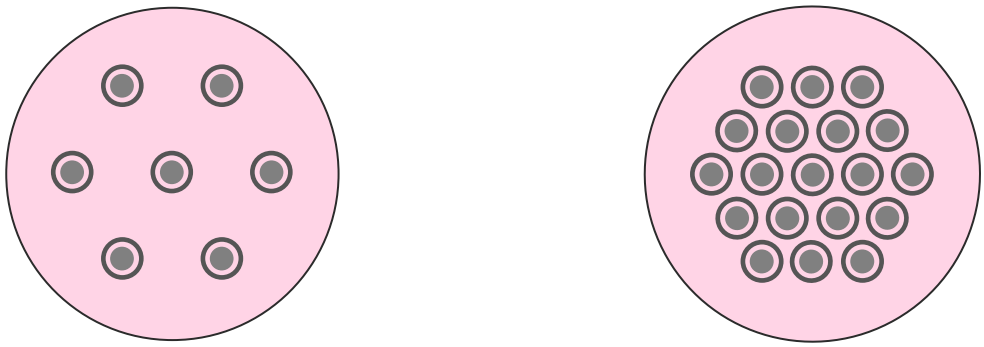

(a) (b)

Figure 5.1: HCPS for (a) 7-core fiber and (b) 19-core fiber.

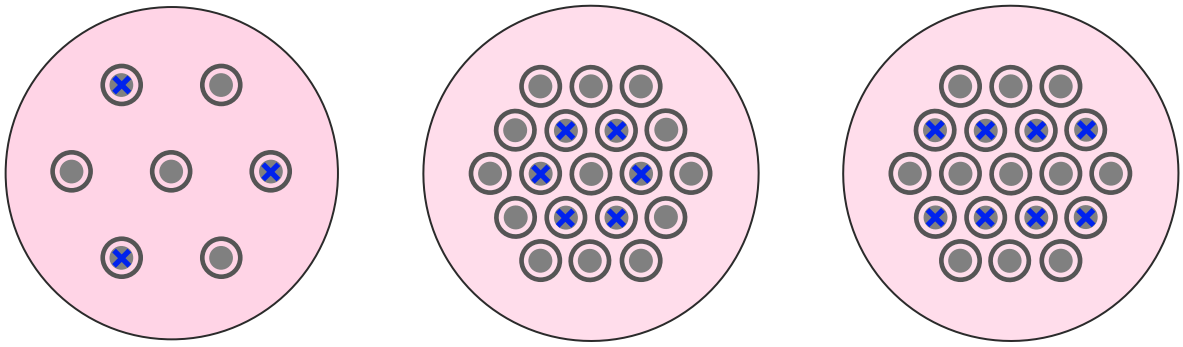

(a) (b) (c)

Figure 5.2: HCPS for (a) 7-core fiber with bidirectional core assignment, (b) 19-core fiber with first core assignment scheme and (c) 19-core fiber with second core assignment scheme.

As the forward propagated XT is much higher than the backward propagated XT arising from the Rayleigh backward scattering for an MCF of 100 km, the worst XT is determined by the forward propagated XT from the N_{adj} adjacent cores. As can be seen from the figure, the number of adjacent cores with the same propagation direction in HCPS, N_{adj}, cannot be reduced to zero under PDI. For instance, N_{adj} in the center core of the 7-core fiber is reduced from 6 under unidirec-

tional transmission scheme to 3 under PDI transmission scheme, resulting in the XT improvement of 3 dB. Considering the worst case scenario, for the 19-core fiber, N_{adj} is reduced from 6 under unidirectional transmission scheme to 2 under PDI transmission scheme, resulting in the XT improvement of 4.8 dB. Even though two different bidirectional core assignments can be used in the 19-core fiber as shown in Fig. 5.2(b) and Fig. 5.2(c), the XT performances are the same if only the worst case scenario is considered. It should be noted that the number of cores in each propagation direction cannot be the same due to the fact that the total number of cores in MCFs with HCPS is always odd. Due to these limitations, HCPS is not considered in this chapter for designing low-XT and high-count MCFs.

In this chapter, we design high-count homogeneous MCFs by fully using the analytical model for XT in TA-MCFs and the backward propagated XT formulation in PDI which we have developed and described in the previous chapters. The XT in high-count MCFs not only depends on fiber structural parameters but also on core layout structures as the XT of any core in an MCF is proportional to the number of adjacent cores in linear scale.

As a simple example, we first investigate different core layout structures for 12-core fibers for both unidirectional and PDI transmission schemes. In order to utilize the XT reduction benefits of PDI, core layout structures have to be carefully chosen as those suited for unidirectional transmission scheme may not be suitable for PDI. Thus, we first study different core layout structures such as ORS and DRS, and then we conclude that existing core layout structures are not suitable for PDI and propose SLS to be used for PDI as it can overcome the disadvantages of the previously mentioned core arrangement structures, resulting in much lower XT under PDI. We then design MCFs with more than 20 cores, namely, 24-core fiber and 32-core fiber both with SLS. The worst XT in the 32-core fiber is -23 dB at 1550 nm over 100 km even by adopting PDI for XT reduction. In order to achieve MCFs with a target XT of -30 dB over 100 km, a heterogeneous TA 32-core fiber with PDI is designed where 2 types of non-identical cores are used, resulting in the worst XT of -30 dB at 1550 nm over 100 km. We conclude that heterogeneous core arrangements with more than 2 types of cores are needed such as 3 or even 4 types of cores if we need to design low-XT MCFs without adopting PDI.

5.2 Core Layout Structures

5.2.1 Core layout structures for unidirectional transmission scheme

In order to search for the core layout structure with highest core density, we first investigate the core layout structures with 12-core fibers for simplicity. For 12-core fibers, core layout structures such as ORS and DRS have been proposed and such fibers have been adopted in different transmission experiments [44, 62, 66], enabling over one Pbit/s capacity transmission [44]. The cross-sectional views of these two structures are shown in Fig. 5.3(a) and Fig. 5.3(b), respectively.

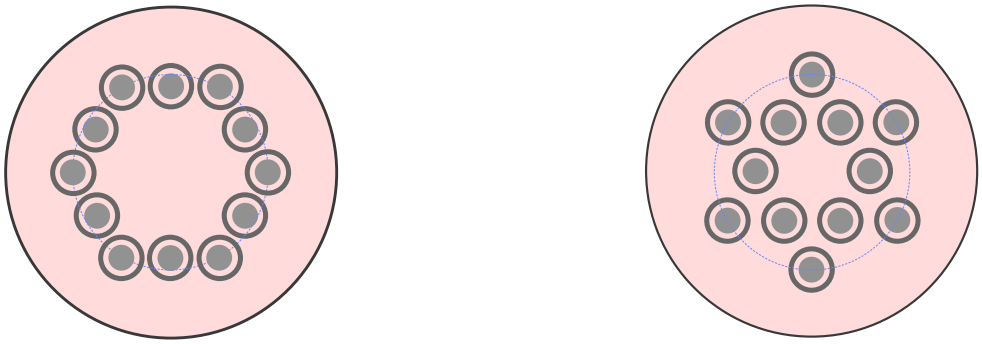

(a) (b)

Figure 5.3: 12-core fibers with (a) ORS and (b) DRS.

Cores in 12-core fibers can also be arranged using a "circular ORS" and a square-lattice structure (SLS) as shown in Fig. 5.4(a) and Fig. 5.4(b), respectively. Circle packing in a circle is a two-dimensional packing problem with the objective of packing unit circles into the smallest possible larger circle and its results can be directly used for core layout structures in MCFs design such that the lowest XT can be achieved. Ref. [81] lists optimum packing structures for a total number of circles ranging from 2 to 65. It should be noted that the optimum packing structure for a total number of circles between 12 and 20 are conjectured optimal. For the 12 circles case, the optimal packing structure (OPS) as shown in Fig. 5.4(c) has been mathematically proven [82], and it is the same as the conjectured one in Ref. [83]. It should be noted that the 9 outer cores in OPS are arranged into 3 groups as shown in Fig. 5.4(c) where the center core in each group has the same distance (Λ) to the two adjacent cores, and the distance between the closest cores in different groups is larger than Λ. Since this is the proven optimal core layout structure, the XT performance of this structure will be better than all the other existing core layout structures.

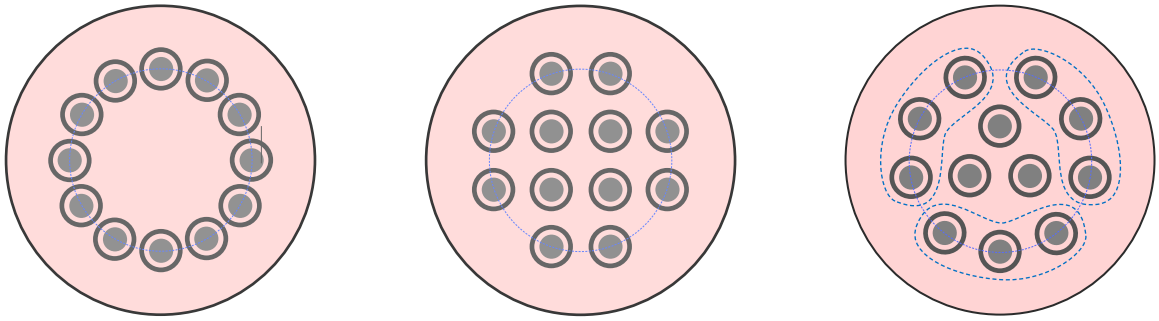

(a) (b) (c)

Figure 5.4: 12-core fibers with (a) circular ORS, (b) SLS and (c) OPS.

We can then compare these five core layout structures (ORS, DRS, "circular ORS", SLS and OPS) in terms of XT performance under the same cladding diameter and cladding thickness constraints. As discussed in the previous chapter, DRS can reduce the XT as compared to ORS in unidirectional transmission scheme as the core pitch in DRS is larger than that in ORS. The fiber structural parameters used in the comparison are listed in Table 5.1 where the fiber length and the bending radius are assumed to be 100 km and 140 mm, respectively. The distance from the center of the MCF to the center of the outer cores is $b = D_{\text{clad}}/2 - CT$. As the maximum D_{clad} is limited to around 225 μm so as to satisfy the limit of failure probability due to mechanical constraints, and the minimum CT is assumed to be 30 μm due to the micro-bending loss constraints, thus, the maximum b is around 82.5 μm.

Table 5.1: Fiber structural parameters in 12-core fibers with different core layout structures

Parameters	a_1	a_2/a_1	w_{tr}/a_1	Δ_1	Δ_2
Values	4.5	2.0	1.0	0.35	– 0.70
Units	μm	-	-	%	%

The worst XT in an MCF is defined as

$$\text{XT}_{\text{worst}} = 10\log_{10} N_{\text{adj}}\text{XT} = \text{XT}_{\text{dB}} + 10\log_{10} N_{\text{adj}}, \tag{5.1}$$

where N_{adj}, XT and XT_{dB} are the maximum number of adjacent cores at a distance of Λ, core-to-core XT in linear scale and core-to-core XT in dB, respectively.

As can be seen from the above equation, the more the adjacent cores the core under XT consid-

eration has, the worse the XT becomes. For instance, if the number of adjacent cores is 4, the worst XT is around 6 dB worse than the core-to-core XT. As can be seen from Fig. 5.3 and Fig. 5.4, for the inner cores in DRS, SLS and OPS, they all have 4 adjacent cores, while for the outer cores, the number of adjacent cores in these three structures have been reduced to only 2. Since the worst XT scenario is considered, the XT evaluation will be based on the inner cores. On the other hand, all the cores in ORS and "circular ORS" have only 2 adjacent cores. By taking the number of adjacent cores into account and using the analytical model for XT in homogeneous TA-MCFs, the worst XT can then be evaluated. The XT comparison results at 1550 nm for a fiber of 100 km are shown in Table 5.2 where each core layout structure is ranked according to its XT performance. The core pitch in each core layout structure is also listed and expressed in relation to b.

Table 5.2: Worst XT in different core layout structures with unidirectional transmission scheme at 1550 nm for a fiber length of 100 km

	ORS	DRS	Circular ORS	SLS	OPS
N_{adj} (no. of adjacent cores)	2	4	2	4	4
Λ (relative to b)	$0.5b$	$0.5774b$	$0.5176b$	$0.6325b$	$0.6603b$
Λ at b = 82.5 (μm)	41.25	47.6	42.7	52.2	54.5
Worst XT (dB)	– 47.0	– 64.1	– 51.6	– 78.5	– 85.7
XT Performance ranking	5	3	4	2	1

As can be seen from the table, OPS has the lowest XT among all the structures as expected. It should be noted that ORS which was proposed and adopted in the 12-core fiber for one Pbit/s transmission experiment [44] provides the highest XT. By going from ORS to "circular ORS", the worst XT is improved by 4.6 dB while the XT reduction by going from ORS to DRS is substantially large as much as around 17 dB as discussed in the previous chapter. The XT can be further improved by adopting SLS, which improves the XT by 14.4 dB compared to DRS. It should be noted that DRS, the quasi-optimal structure defined in the previous chapter only ranks the 3rd on the list, which is obtained by the core position movement based on ORS. The worst XT in OPS is further 7.2 dB lower than the one in SLS due to the 2.3 μm larger core pitch.

In addition to the comparison table, the worst XT in different structures for 12-core fibers are also plotted in Fig. 5.5 for visually illustrating the XT performance of the 5 different core layout structures. It should be noted that even though the new core layout structure OPS results in lower

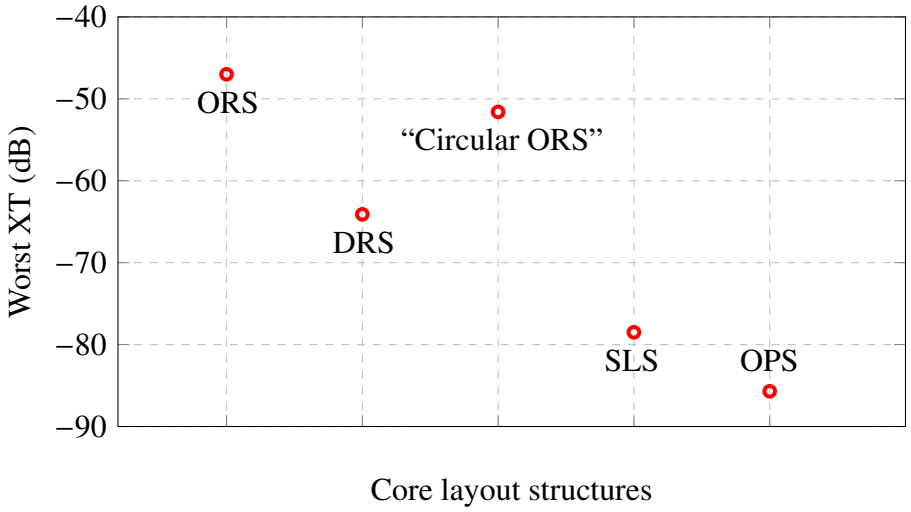

Figure 5.5: The worst XT in the five different core layout structures for 12-core fibers under unidirectional transmission scheme at 1550 nm for a fiber length of 100 km.

XT compared to SLS, it might be challenging to fabricate fibers with such a core layout structure as the structure is unsymmetrical and difficult to maintain during the manufacturing process.

5.2.2 Core layout structures for PDI transmission scheme

The PDI transmission scheme can also be used in MCFs for XT reduction as discussed in Chapter 2. With Eq. (2.17), the difference of XT between the backward propagated XT (XT_b) and the forward propagated XT (XT_f) can be plotted as a function of fiber length at 1550 nm as shown in Fig. 5.6. As can be seen from the figure, the absolute value of the XT difference decreases as the fiber length increases due to Rayleigh scattering, weakening the XT reduction effect of PDI for longer MCFs. For an MCF with a length of 100 km, XT_b is around 18.6 dB lower than XT_f, achieving significant XT reduction by PDI.

Among the five core layout structures investigated above for 12-core fibers, namely, ORS, DRS, “circular ORS”, SLS and OPS, only a 12-core fiber with DRS was used in high-capacity transmission experiments adopting the PDI transmission scheme [62, 66]. Thus, it would be worthwhile to investigate the XT reduction benefits of PDI in the other four core layout structures. In the PDI transmission scheme, the signal propagation direction of each core is assigned in an interleaved manner [84] so that the XT reduction benefits of PDI are effectively utilized. For instance, ORS,

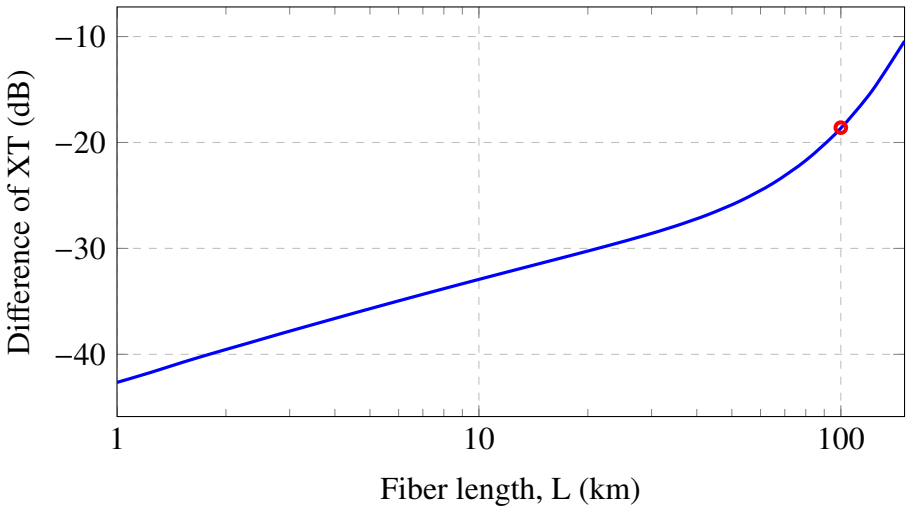

Figure 5.6: The difference of XT between the backward propagated XT and the forward propagated XT in PDI transmission scheme as a function of fiber length at 1550 nm.

"circular ORS" and SLS can adopt interleaved core assignments as shown in Fig. 5.7(a), Fig. 5.7(b) and Fig. 5.7(c), respectively, where the propagation direction in the cores with "×" is opposite to that in the cores without the mark.

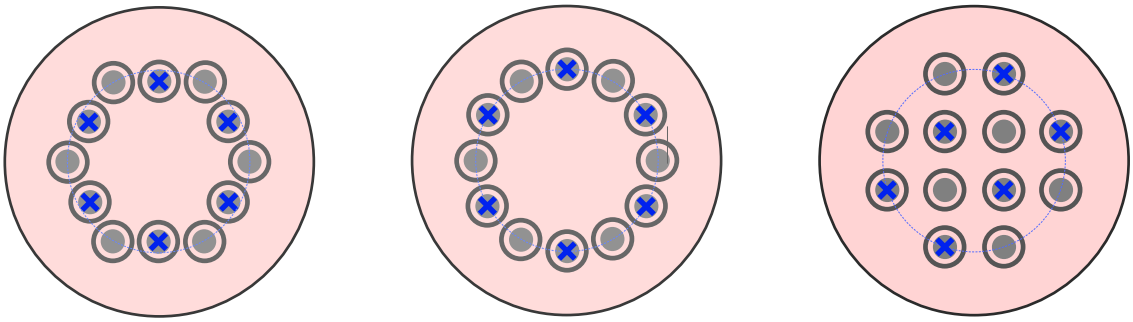

Figure 5.7: Interleaved core assignments for PDI transmission scheme in 12-core fibers with (a) ORS (b) circular ORS and (c) SLS. The propagation direction in the cores with "×" is opposite to that in the cores without the mark.

Under the unidirectional transmission scheme, the number of adjacent cores for all the cores in ORS, "circular ORS" and for the outer cores in SLS are 2 while for the inner cores in SLS, the number of adjacent cores is 4. As can be seen from the figure, by adopting the interleaved core assignments, the number of adjacent cores with the same propagation direction has been reduced

to zero for all the cores in these three core layout structures. Thus, large XT reduction can be expected. For some core layout structures, however, cores cannot be assigned in an interleaved manner. Such structures include DRS and OPS, in which the cores are assigned in such a way that the number of adjacent cores with the same propagation direction is reduced to one or two. The cross-sectional views of DRS and OPS with bidirectional core assignments are shown in Fig. 5.8(a) and Fig. 5.8(b), respectively.

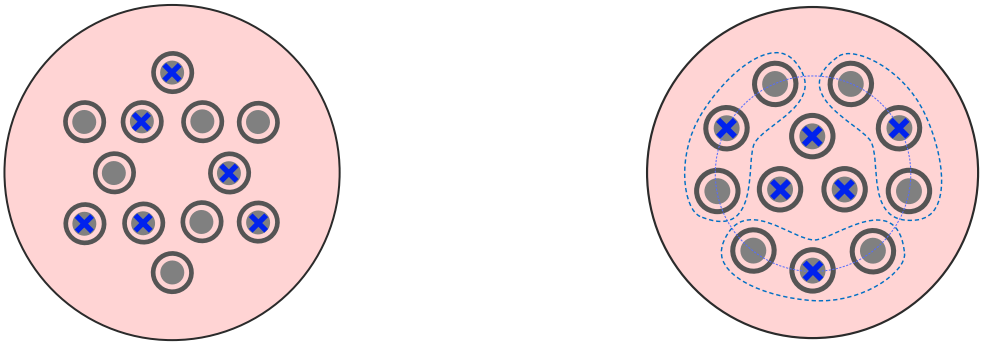

(a) (b)

Figure 5.8: Bidirectional core assignments in 12-core fibers with (a) DRS and (b) OPS. The propagation direction in the cores with "×" is opposite to that in the cores without the mark.

For DRS and OPS, the XT improvement is determined by the reduction of N_{adj} by adopting PDI. For ORS, "circular ORS" and SLS, N_{adj} can be reduced to zero using the interleaved core assignment as shown in Fig. 5.7, and thus, the XT is determined by the backward propagated XT in the adjacent cores and the forward propagated XT in the non-adjacent cores. It should be noted that for an MCF with more than 100 km, the forward propagated XT in the non-adjacent cores is much lower than the backward propagated XT in the adjacent cores. Thus, only the backward propagated XT in the adjacent cores should be taken into account for XT improvement estimation by PDI in comparison to unidirectional transmission scheme.

The XT improvements between the unidirectional and PDI transmission schemes, ΔXT, for these five different core layout structures are then calculated and listed in Table 5.3 at 1550 nm for a fiber length of 100 km where the worst XT scenario (cores with the maximum number of adjacent cores under the same propagation direction) is considered. It should be noted that the ΔXT in ORS, "circular ORS" and SLS depends on the fiber length, as the absolute value of the difference between backward propagated XT and forward propagated XT decreases with the fiber length, which is 18.6 dB for an MCF of 100 km as illustrated in Fig. 5.6. It should be noted that in

Table 5.3: XT improvement (ΔXT) by PDI in five different core layout structures at 1550 nm for a fiber length of 100 km

Structure Names	N_{adj}		ΔXT (dB)
	Unidirectional	PDI	
ORS	2	0	18.6
DRS	4	1	6
Circular ORS	2	0	18.6
SLS	4	0	18.6
OPS	4	2	3

all the five core layout structures, ΔXT does not depend on the core pitch nor the cladding diameter as it is a relative value while the absolute XT depends on the core pitch.

Using the same fiber structural parameters as in Table 5.1, the worst XT at 1550 nm for a fiber length of 100 km in five different core layout structures can be calculated and listed in Table 5.4.

Table 5.4: Worst XT in five different core layout structures with PDI transmission scheme at 1550 nm for a fiber length of 100 km

	ORS	DRS	Circular ORS	SLS	OPS
N_{adj} (no. of adjacent cores)	0	1	0	0	2
Λ (relative to b)	0.5b	0.5774b	0.5176b	0.6325b	0.6603b
Λ at b = 82.5 (μm)	41.25	47.6	42.7	52.2	54.5
Worst XT (dB)	– 65.6	– 70.1	– 70.2	– 97.1	– 88.7
XT Performance ranking	5	4	3	1	2

As can be seen from the table, SLS has the best the XT performance among all the five core layout structures for 12-core fibers under the PDI transmission scheme. The worst XT in SLS is even 8.4 dB lower than the one in OPS. The worst XT in DRS and "circular ORS" are very close to each other, while the worst XT in ORS is the highest among all the five core layout structures under PDI. It should be noted that the worst XT in ORS is always the highest among all the five core layout structures whether the PDI transmission scheme is adopted or not. In addition to the comparison table, the worst XT in five different core layout structures for 12-core fibers are also

plotted in Fig. 5.9 where the ones with ∘ circle mark are for the unidirectional transmission scheme and the ones with □ square mark are for the PDI transmission scheme.

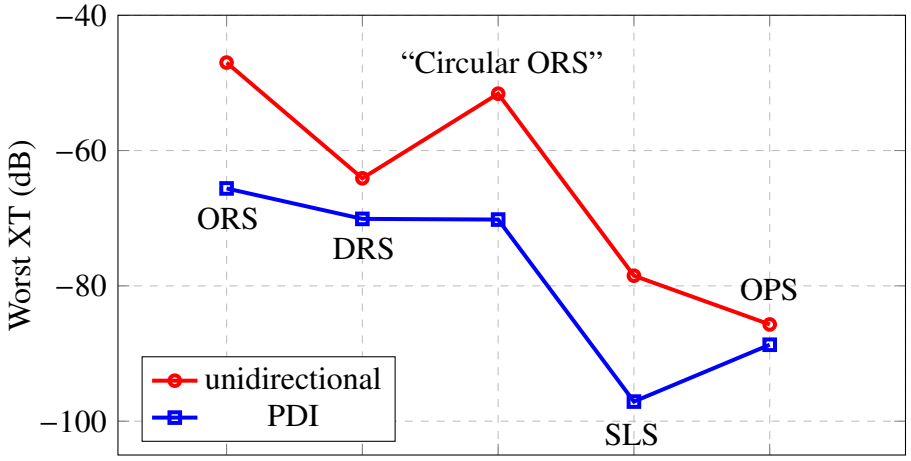

Figure 5.9: The worst XT in the five different core layout structures for 12-core fibers, under unidirectional and PDI transmission schemes at 1550 nm for a fiber length of 100 km. Open circle: unidirectional transmission scheme, open square: PDI transmission scheme.

As discussed previously, SLS has the advantage of being able to fully utilize the benefits of XT reduction by PDI but is also very flexible in adopting both unidirectional and PDI transmission schemes. Thus, it is concluded that SLS should be used for designing high-count MCFs in the following sections.

5.3 High-Count MCFs Design Examples

5.3.1 Homogeneous 24-core fiber

With the previous investigation on different core layout structures, SLS is the preferred core layout structure and it is adopted in this section for designing homogeneous 24-core fibers. The cross-sectional views of the homogeneous 24-core fiber with SLS under unidirectional and PDI transmission schemes are shown in Figs. 5.10(a) and 5.10(b), respectively. The cladding diameter and

cladding thickness are 230 μm and 30 μm with a core pitch of 33.3 μm. The fiber structural parameters used in here are the same as in Table 5.1 where the effective area A_{eff} is 78 μm^2 at 1550 nm.

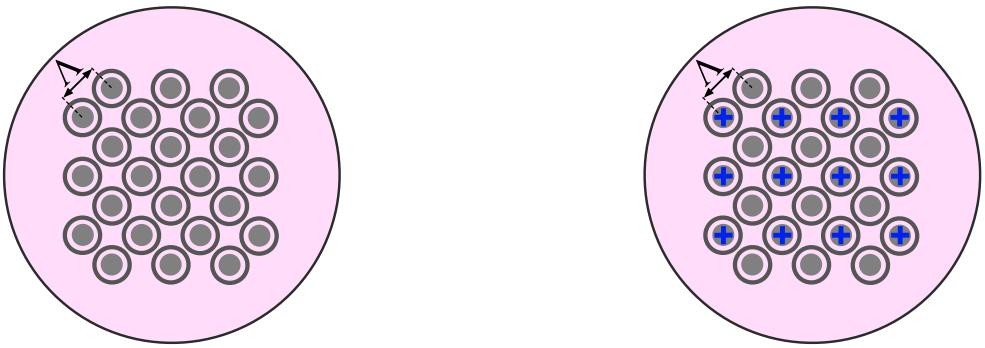

(a) (b)

Figure 5.10: Cross-sectional views of a square-lattice structured homogeneous 24-core fiber under (a) unidirectional and (b) PDI transmission schemes.

With these fiber structural parameters, the worst XT (for cores with 4 adjacent cores at a distance of Λ experiencing the highest XT) under unidirectional and with PDI transmission schemes over 100 km are plotted as a function of wavelength as shown in Fig. 5.11.

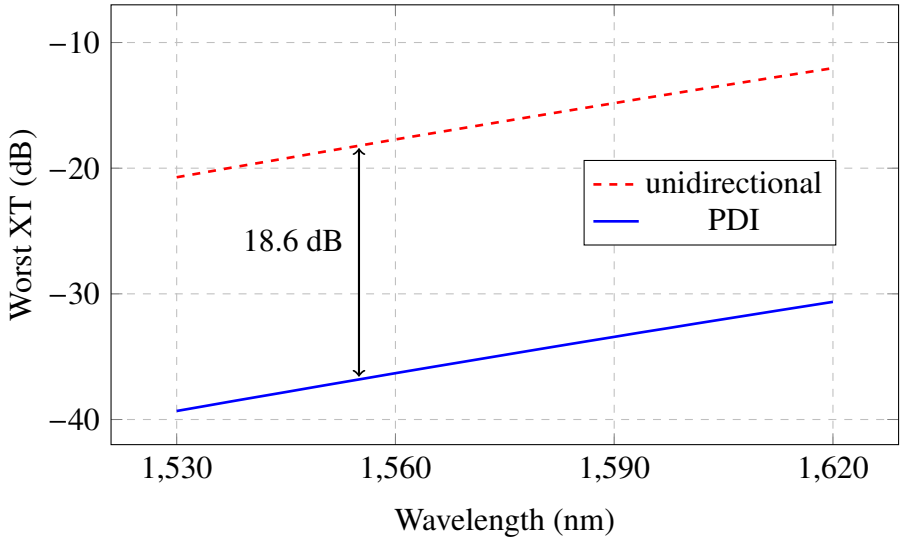

Figure 5.11: Worst XT over 100 km as a function of wavelength for a homogeneous 24-core fiber under unidirectional and PDI transmission schemes, with bending radius of 140 mm.

As can be seen from the figure, the worst XT without adopting PDI is around − 18.4 dB at 1550

nm over 100 km, which is too high for MCF transmission using advanced modulation formats such as 32QAM. By adopting PDI, the XT is dramatically reduced, resulting in the XT reduction of 18.6 dB as compared to the case without PDI. Thus, the worst XT with PDI can be reduces to − 37 dB at 1550 nm over 100 km so that the fiber can be used for MCF transmission with advanced modulation formats. It should be noted that for the case of PDI, the backward propagated XT from the adjacent cores at a distance of Λ is the much higher compared to the forward propagated XT from the cores at a distance of $\sqrt{2}\Lambda$.

5.3.2 Homogeneous 32-core fiber

In order to find out the maximum number of cores that can be packed in a homogeneous TA-MCF with low-XT at 1550 nm over 100 km under the limited cladding diameter and cladding thickness, a TA-MCF with the number of cores as high as 32 is then designed and described in this section. The cross-sectional views of the square-lattice structured homogeneous 32-core fibers under unidirectional and PDI transmission schemes are shown in Figs. 5.12(a) and 5.12(b), respectively. With the same cladding diameter and cladding thickness as for the 24-core fiber, the core pitch becomes 29.2 μm. The other fiber structural parameters are the same as the 24-core fiber.

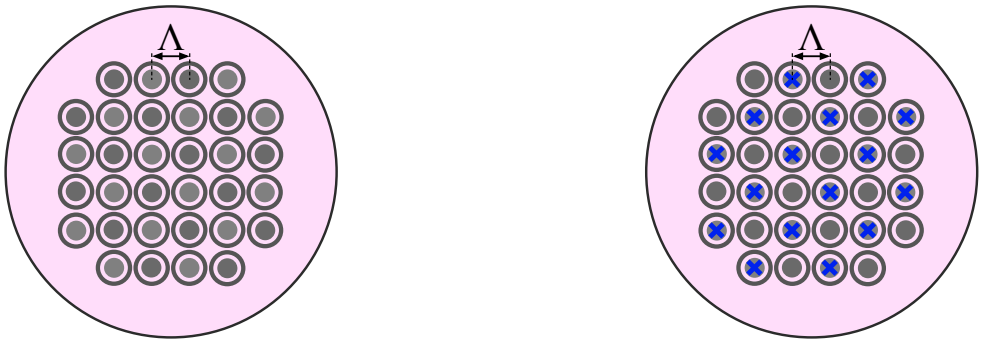

(a) (b)

Figure 5.12: Cross-sectional views of a homogeneous 32-core fiber under (a) unidirectional and (b) PDI transmission schemes.

The worst XT in the homogeneous 32-core fiber under unidirectional and PDI transmission schemes (adopting interleaved core assignment) over 100 km can also be plotted directly as a function of wavelength as shown in Fig. 5.13.

Due to the reduced core pitch as compared to the 24-core fiber (29.2 μm in 32-core fiber versus

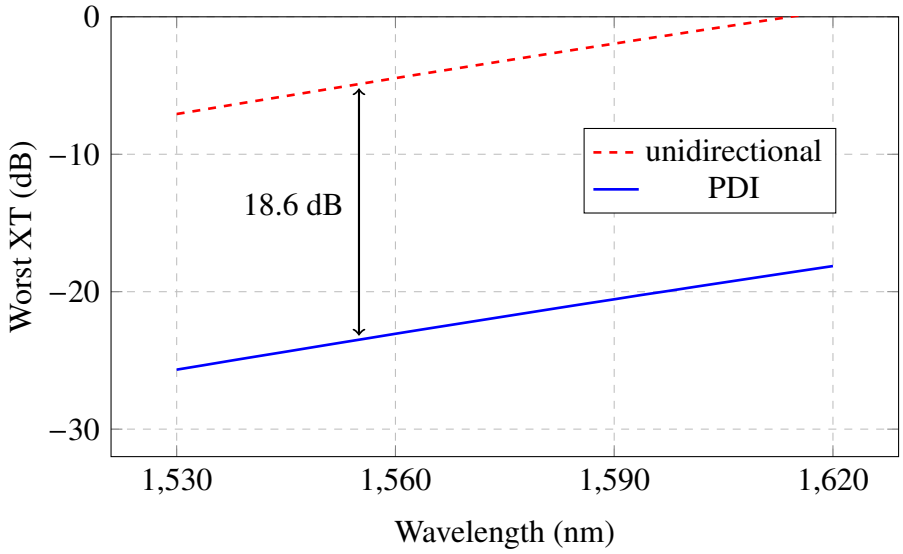

Figure 5.13: Worst XT over 100 km as a function of wavelength in a homogeneous 32-core fiber under unidirectional and PDI transmission schemes, with bending radius of 140 mm.

33.3 μm in 24-core fiber), the worst XT is increased by around 14 dB both for the case under unidirectional and PDI transmission schemes. As can be seen from the figure, the worst XT in the 32-core fiber under unidirectional and PDI transmission schemes are around − 4.4 dB and − 23 dB at 1550 nm over 100 km, respectively. Even with PDI, the XT in the homogeneous 32-core fiber is still too high for 32QAM to be used, and thus, it is concluded that heterogeneous core arrangements should be adopted for further XT reduction and will be described in the next section.

5.3.3 Heterogeneous 32-core fiber

A 32-core fiber with heterogeneous core arrangement is designed, where the core layout structure is also the same as the one in the homogeneous 32-core fiber. The cross-sectional view of the heterogeneous 32-core fiber is shown in Fig. 5.14(a). In order to simplify the design, only two types of heterogeneous cores are used in this work as compared to other work [80], where 4 types of non-identical cores are used.

As shown in Fig. 5.14(b), 2 types of non-identical TA cores (A and B) with slightly different fiber structural parameters are used for the heterogeneous core arrangement. The fiber parameters are chosen in such a way that both A and B have similar effective areas for similar fiber nonlinearity in all the cores. The fiber structural parameters are listed in Table 5.5 with corresponding effective

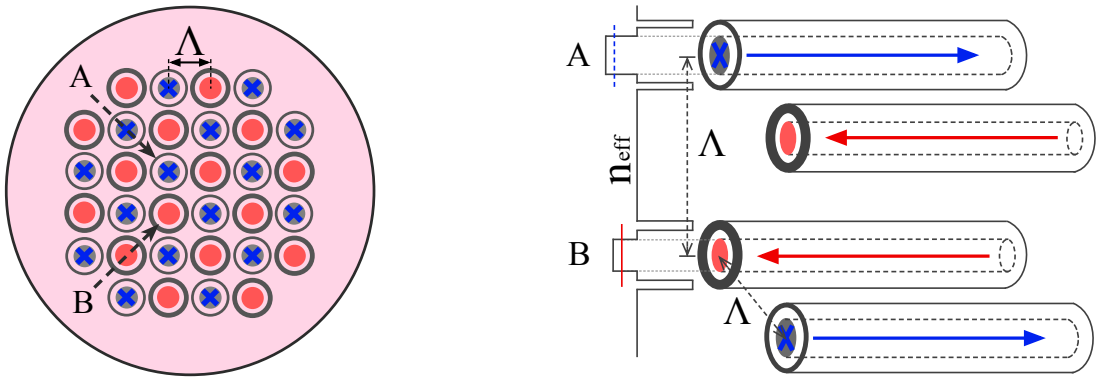

(a) (b)

Figure 5.14: (a) Cross-sectional view of a heterogeneous 32-core fiber with SLS and (b) side view of an interleaved core assignment under PDI transmission scheme.

area A_{eff} of 77 μm^2 and 80 μm^2 for core types A and B at 1550 nm, respectively. The core pitch is still 29.2 μm, which is the same as for homogeneous 32-core fibers with SLS. The correlation length d in the heterogeneous core arrangement and the bending radius R_{b} are assumed to be 50 mm [85] and 140 mm, respectively.

Table 5.5: Fiber structural parameters of a heterogeneous square-lattice structured 32-core fiber with 2 types of non-identical cores

Parameters	A	B	Units
a_1	4.6	4.3	μm
a_2/a_1	2	2	-
w_{tr}/a_1	0.35	1	-
Δ_1	0.38	0.30	%
Δ_2	−0.70	−0.70	%

It should be noted that the inner cores surrounded by adjacent cores would cause the cable cutoff wavelength lengthening. In order to minimize this effect, the trench width of a high-index core (type A) is chosen to be much less compared to that of a low-index core (type B) as the theoretical cutoff wavelength in A is much longer than the one in B. Simulated cable cutoff wavelengths in core A and core B are around 1525 nm and 1436 nm, respectively.

For estimating the worst case XT, all the adjacent cores should be taken into account. For

instance, core A is surrounded by 4 cores of both A and B types at a distance of $\sqrt{2}\Lambda$ and Λ, respectively; while core B is surrounded by 4 cores of both A and B types at a distance of Λ and $\sqrt{2}\Lambda$, respectively. The worst XT of these two cores under unidirectional and PDI transmission schemes in the heterogenous 32-core fiber are plotted in Fig. 5.15.

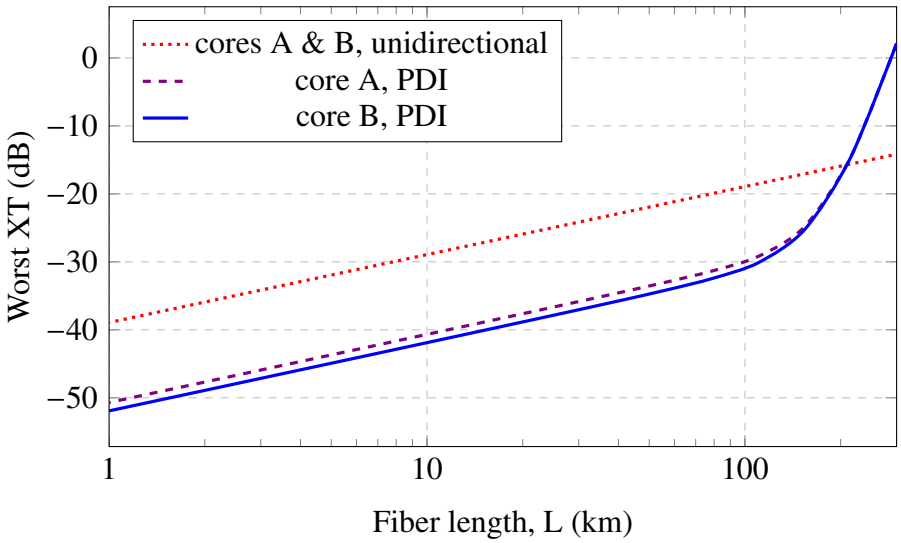

Figure 5.15: The worst XT of core A and core B in a heterogeneous 32-core fiber under two different transmission schemes as a function of fiber length at 1550 nm.

As can be seen from the figure, both core A and core B under unidirectional transmission scheme have the same XT performance as a function of fiber length. By adopting PDI, the XT can be further reduced compared to the case under unidirectional transmission scheme for fiber lengths less than 210 km where the XT increases almost linearly with fiber length up to 100 km. The increasing rate of backward propagated XT begins to grow rapidly after 100 km due to the Rayleigh scattering from PDI. The amount of XT reduction in PDI is thus limited by Rayleigh scattering, an intrinsic physical effect, which is difficult to eliminate. The worst XT in core A and core B under PDI transmission scheme are around − 30 dB and − 31 dB for a fiber length of 100 km at 1550 nm, respectively. Such low-XT and high-count MCFs are expected to increase the capacity per fiber well beyond one Pbit/s.

5.4 Summary

We investigated various core layout structures for designing low-XT and high-count MCFs under two different transmission schemes. Among the five different core layout structures, the XT performance of SLS is excellent both in the unidirectional and PDI transmission schemes and the structure is very flexible and therefore, SLS is the preferred core layout structure. By using the analytical model for XT in TA-MCFs and SLS as a core layout structure, a homogeneous 24-core fiber and a 32-core fiber are designed for both unidirectional and PDI transmission schemes. The worst XT in a homogeneous 32-core fiber is around -23 dB at 1550 nm over 100 km even by adopting PDI for XT reduction. In order to achieve lower XT MCF with more than 30 cores, a heterogeneous 32-core fiber for PDI with 2 types of non-identical cores is designed, resulting in the worst XT of -30 dB at 1550 nm over 100 km. It is concluded that a heterogeneous core arrangement with more than 2 types of cores, for instance, 3 or even 4 types of cores are needed if we are restricted to design low-XT MCFs without adopting PDI.

□ End of chapter.

Chapter 6

XT Measurement in MCF FI/FO Devices

6.1 Introduction

In the previous chapters, we have studied uncoupled MCFs for long-distance and high-capacity transmission systems. Theoretical models of XT in MCFs and their XT properties have been studied and well established [56, 75, 78, 79] including our work in this thesis. One of the essential components in uncoupled MCF transmission systems is the fan-in/fan-out (FI/FO) device which connects SMF-based devices and MCFs. Several techniques for constructing FI/FO devices have been proposed, such as free-space lens optics [86], polymer waveguide [87] and bundled fiber devices where bundled fiber devices based on physical-contact between MCFs and SMFs have been fabricated with a very low connection loss and high return loss [88].

The FI/FO devices play an important role for determining the overall system performance; if the XT in the FI/FO devices is higher than that in MCFs within the same fiber link, the former limits the overall system performance. However, the XT properties in FI/FO devices have not been well studied and there is no theoretical model to predict the XT behaviors in such devices. One way to analyze the XT properties in different FI/FO devices is by experimental measurements. Just as the XT in MCFs can be measured using a core-to-core coupling between SMFs and MCFs [89], the same method can also be used for the XT measurements in MCF FI/FO devices. As the name states, the method requires perfect coupling between each core of an MCF and an SMF, which is difficult and time-consuming unless advanced MCF-SMF coupling equipment is available. In addition, the

measured XT is also affected by the MCF-SMF coupling accuracy. For instance, if the coupling is not perfect, the SMF may pick up XT light from the cladding region instead of from the core in the MCF [90]. Due to these two main issues, measurement results obtained by the MCF-SMF coupling-based method can be unreliable and error-prone, and thus more robust and easy-to-adopt method has urgently been needed.

In this chapter, we propose a novel measurement method for XT in MCF FI/FO devices, which is based on Fresnel reflection at the MCF-to-air interface. In the new method, the MCF-SMF coupling is not needed and the measurement results are immune to the cleaving angle of the MCF if the cleaving angle is small enough. The XT values obtained by this new method are compared with those obtained by the traditional core-to-core coupling method, and it is found that they show very similar statistical properties, indicating that our method gives an alternative powerful method of XT measurements in MCF FI/FO devices.

6.2 XT Measurement Methods

6.2.1 MCF-SMF coupling-based method

The most straightforward method for XT measurement is based on MCF-SMF coupling and it is shown in Fig. 6.1, where a physical-contact-type FI/FO device connects an N ($N = 7$ in this case) small diameter fibers to the corresponding cores in an N-core fiber. The diameter of the small diameter fiber is the same as the core pitch of the N-core fiber.

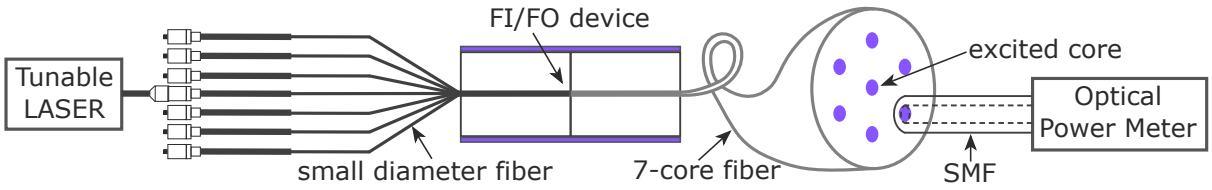

Figure 6.1: Principle of the MCF-SMF coupling-based XT measurement method.

Optical powers in each core of the MCF (both the excited core and the other cores) are monitored at the MCF end using MCF-SMF coupling as shown in the figure. The XT is defined as the power ratio of the other cores to the excited core. Since MCFs used in this setup are normally very short, i.e. around 1 m, and their XT is as low as -80 dB if we use MCFs with -30 dB of XT over

100 km at 1550 nm, the XT from the MCF can then be ignored as it is much lower than the typical value of XT in the MCF FI/FO devices.

6.2.2 Fresnel reflection-based method

Using the Fresnel reflection at the glass-air interface, a new XT measurement method for MCF FI/FO devices can be established. The principle of the Fresnel reflection-based method is shown in Fig. 6.2. The output end of the MCF is exposed to the air and thus the glass-air interface is formed.

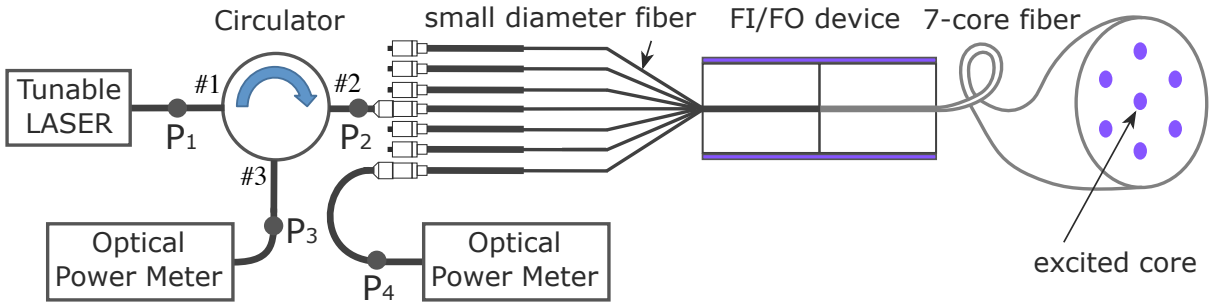

Figure 6.2: Proposed Fresnel reflection-based XT measurement method.

As can be seen from the figure, P_1, P_2, P_3 and P_4 are the locations where the optical powers are monitored. It should be noted that P_1 is only for power monitoring at the output of the laser, as P_2 is used for XT estimation instead of P_1, and these two power levels differ from each other due to the insertion loss from port 1 to port 2 of the circulator. The Fresnel reflected power from the excited core comes out from port 3 of the circulator and it is measured by the optical power meter at P_3. The Fresnel reflected power from a neighboring core goes directly to the optical power meter at P_4. The Fresnel reflection loss is related to the angle at the glass-air interface. If smooth cleaving (all the cores in MCF having the same cleaving angle) is achieved at the MCF end, the Fresnel reflection losses monitored at P_3 and P_4 will be the same. As the XT is directly related to the power (in dBm) difference between P_3 and P_4, the Fresnel reflection losses at P_3 and P_4 cancel out each other. Thus, it is not necessary to calculate the Fresnel reflection loss based on the cleaving angle of MCF at the glass-air interface. Even though the angle at the glass-air interface does not affect the XT measurements results as explained above, it should always be sensible to make the angle as close to 0^o as possible so that the reflected light at the MCF-air interface can still be guided in the core region instead of entering the cladding. In some extreme cases, if the angle is too large,

not all the reflected light is guided in the core, the reflected power at P_4 may be even lower than the minimum detectable powers of available optical power meters or optical spectrum analyzers, which makes obtaining the exact value of P_4 difficult.

The reflected power inside the excited core, P_{3_dBm}, is related to P_{2_dBm} by

$$P_{3\_dBm} = P_{2\_dBm} - 2\alpha_C - 2\alpha_F - \alpha_R - \alpha_{23}, \tag{6.1}$$

where α_C is the connection loss at the port 2 between the circulator and SMF, α_F is the insertion loss of the FI/FO device. α_R and α_{23} are the Fresnel reflection loss and the insertion loss from port 2 to port 3 of the circulator.

We then have

$$P_{2\_dBm} = 2(\alpha_C + \alpha_F) + \alpha_R + \alpha_{23} + P_{3\_dBm}. \tag{6.2}$$

The power at P_4 is composed of 2 parts, which are $P_4^{'}$ and $P_4^{''}$, as shown in Fig. 6.3, where the gap between the bundled fibers and the MCF in FI/FO device is for illustration purpose, and the dashed arrows represent the Fresnel reflected light. The light from one SMF of the bundled fibers goes to the corresponding core of the MCF at the ferrule interface, reflected at the glass-air interface and goes to the neighboring core of bundled fibers at the ferrule interface, resulting in $P_4^{'}$. The light can also go from the SMF of the bundled fibers to the neighboring core at the ferrule interface, reflected at the glass-air interface and then goes from the MCF to the corresponding SMF of the bundled fibers, resulting in $P_4^{''}$.

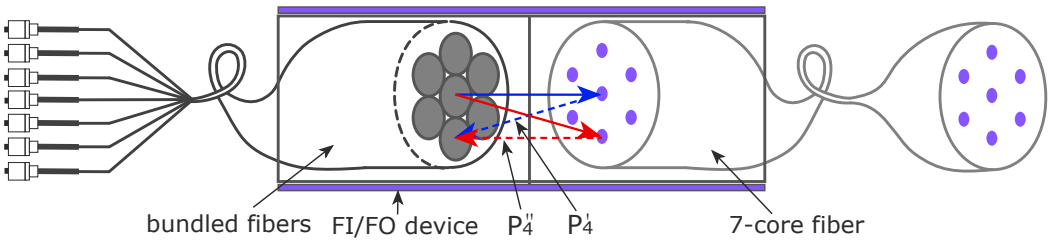

Figure 6.3: Formation of power P_4, composed of $P_4^{'}$ and $P_4^{''}$.

They are related to P_{2_dBm} by

$$\begin{aligned} P_{4\_dBm}^{'} &= P_{2\_dBm} - \alpha_C - \alpha_F - \alpha_R + \mathrm{XT}, \\ P_{4\_dBm}^{''} &= P_{2\_dBm} - \alpha_C + \mathrm{XT} - \alpha_R - \alpha_F. \end{aligned} \tag{6.3}$$

As can be seen from Eq. (6.3), the values of $P_4^{'}$ and $P_4^{''}$ are equal. Thus, P_{4_dBm} can be related to $P_{4\_dBm}^{'}$ by

$$P_{4\_dBm} = P_{4\_dBm}^{'} + 3.01 - \alpha_C, \tag{6.4}$$

where 3.01 is induced as $10\log_{10}2 = 3.01$, α_C is included due to the connection loss between the small diameter fiber and the optical power meter.

By substituting Eq. (6.2) into Eq. (6.3) and by using Eq. (6.4), the XT for each core in FI/FO devices can be calculated as

$$\mathrm{XT} = P_{4\_dBm} - P_{3\_dBm} - 3.01 - \alpha_F - \alpha_{23}. \tag{6.5}$$

6.3 Experimental Setup

The experimental setup for the Fresnel reflection-based XT characterization method is shown in Fig. 6.4. The linewidth of the external cavity tunable laser is in the range of several hundreds kHz to 1 MHz. The wavelength of the light from the tunable laser is set to 1550 nm in this experiment. The light from the tunable laser is firstly passed through a bandpass filter after amplified by an EDFA before it enters a polarization controller. The polarization controller generated 500 random polarization states per 10 seconds to emulate the polarization changes in real transmission systems. A circulator is added to enable the measurement of the reflected power in the excited core. Port 2 of the circulator is connected to one of the small diameter bundled SMFs during each measurement, while the remaining 6 bundled SMFs are left for XT power monitoring. A free space power meter is used to measure the total power at the output of the MCF.

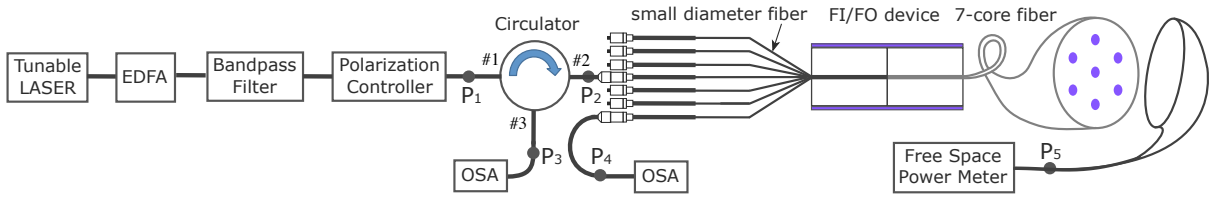

Figure 6.4: Experimental setup of Fresnel reflection-based XT characterization method, where a bandpass filter is placed after the EDFA to eliminate ASE (Amplified Spontaneous Emission) and a polarization controller is added to emulate the polarization changes in real transmission system. OSA: Optical Spectrum Analyzer.

In order to characterize the insertion loss of the FI/FO device for each core, optical powers at P_5 and P_2 are used, as they are related to each other by $P_{5\_dBm} = P_{2\_dBm} - \alpha_C - \alpha_F$, where α_C has been assumed to be 0.1 dB for all the 7 cores. Thus, the insertion loss of the FI/FO device for each core can be calculated by $\alpha_F = P_{2\_dBm} - P_{5\_dBm} - 0.1$ in dB.

6.4 Results and Discussions

(a) (b)

Figure 6.5: Cross-sectional views of (a) 7 bundled small diameter fibers and (b) a 7-core fiber with corresponding core numbers marked.

The cross-sectional views of the 7 bundled small diameter fibers and the 7-core fiber used in the experiment are shown in Fig. 6.5(a) and Fig. 6.5(b), respectively, where corresponding core numbers are indicated. The cladding diameter, cladding thickness and core pitch (Λ) for the 7-core fiber are 195 μm and 47.5 μm and 50 μm, respectively. The two FI/FO devices used in this experiment are marked as sample #1 and sample #2, with corresponding cladding diameters for the small diameter fibers of 50 μm and 49.5 μm, respectively, so as to match the core pitch of the 7-core fiber. The insertion losses of each core in the two FI/FO sample devices are listed in Table 6.1. They range from 0.25 dB to 0.52 dB and from 0.26 dB to 0.57 dB for different cores in sample #1 and #2, with core-averaged insertion losses of 0.38 dB and 0.41 dB, respectively.

The XT measurements were made by exciting one core at a time and measuring the power in the other cores at P_4. There are $7 \times 6 = 42$ different measurement combinations where 7 is the total number of cores and 6 is the number of other measured cores when one core is excited. Each measurement was repeated 10 times, and each time the measurement takes 10 seconds with 500 polarization states generated. As each measurement is repeated 10 times, there is one maximum

Table 6.1: Insertion loss for each core in FI/FO devices

Core number	Sample 1	Sample 2	Units
1	0.25	0.29	dB
2	0.50	0.57	dB
3	0.31	0.49	dB
4	0.27	0.26	dB
5	0.50	0.33	dB
6	0.30	0.47	dB
7	0.52	0.47	dB

power level out of 500 samples per measurement (both at P_3 and P_4), and thus there are 10 such power levels which are averaged and used for the XT estimation.

In order to calculate the XT using Eq. (6.5), the insertion loss from port #2 to port #3 of the circulator (α_{23}) is also needed in addition to α_F, and it is measured to be 0.90 dB. The inter-core XT in FI/FO devices can then be calculated by using the corresponding insertion loss of the FI/FO device (α_F) and the circulator (α_{23}). The measured XT in each core for sample #1 and sample #2 for different excited cores are shown in Figs. 6.6(a) and 6.6(b), respectively, where the x axis represents the core number of each XT value and y axis represents the XT value in dB. The first inset in the figure includes all the measured XT for 7 different excited cores. The XT measured with both the MCF-SMF coupling-based method (represented by blue curve with round shaped mark) and the Fresnel reflection-based method (represented by red curve with triangle shaped mark) are plotted in the same figure.

As can be seen from the the first inset of Figs. 6.6(a) and 6.6(b), the measured XT for both samples using these two different methods show very similar dynamic ranges (difference between the minimum and the maximum XT levels). The dynamic ranges of the measured XT with these two methods for sample #1 and #2 are listed in Table 6.2. The dynamic range is as high as 15 dB for both samples, measured by the two different methods.

As can be seen from the figures, the values of the measured XT in the same core under the same excited core with two different methods are not always close to each other. For instance, in sample #1, when core 1 is excited, the measured XT at core 5, 6 and 7 with these two different

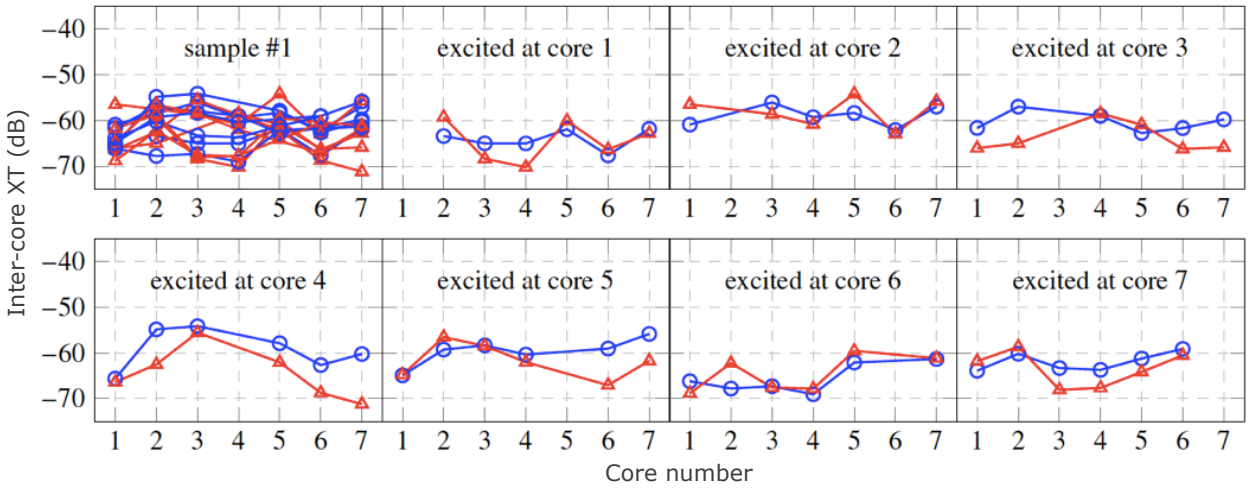

(a)

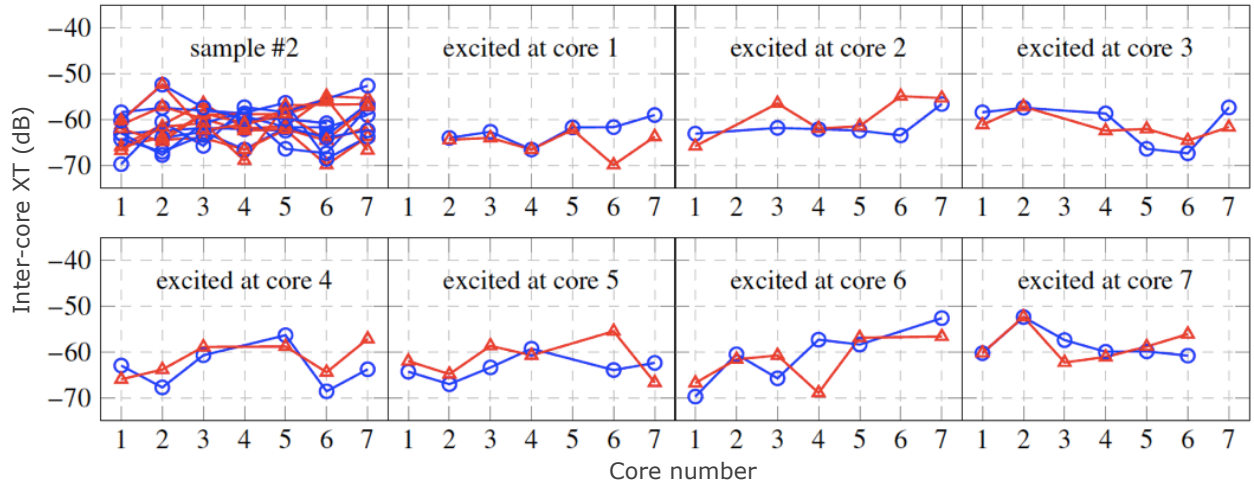

(b)

Figure 6.6: XT by MCF-SMF coupling-based method (blue curve with round shaped mark) and Fresnel reflection-based method (red curve with triangle shaped mark) under each excited core in (a) sample #1 and (b) sample #2.

Table 6.2: Dynamic ranges of measured inter-core XT in FI/FO devices

Sample no.	MCF-SMF	Fresnel reflection	Units
#1	– 69.04 to – 54.16	– 71.11 to – 54.10	dB
#2	– 69.72 to – 52.34	– 69.81 to – 52.21	dB

methods are very close to each other, while the one measured at other cores deviate by 3 to 5 dB as in Fig. 6.6(a). For the case when core 1 is excited, the changing trend of blue curve is very similar to that of red curve, which is also true for the cases under other excited cores.

For each FI/FO device, there are 42 measured XT points in total. As the worst XT among the 42 points determines the performance of the FI/FO device, it is necessary to treat the 42 XT points as a whole and investigate its statistical properties. The two groups of the 42 XT points measured with each method are then sorted and plotted in Figs. 6.7(a) and 6.7(b) for sample #1 and sample #2, respectively.

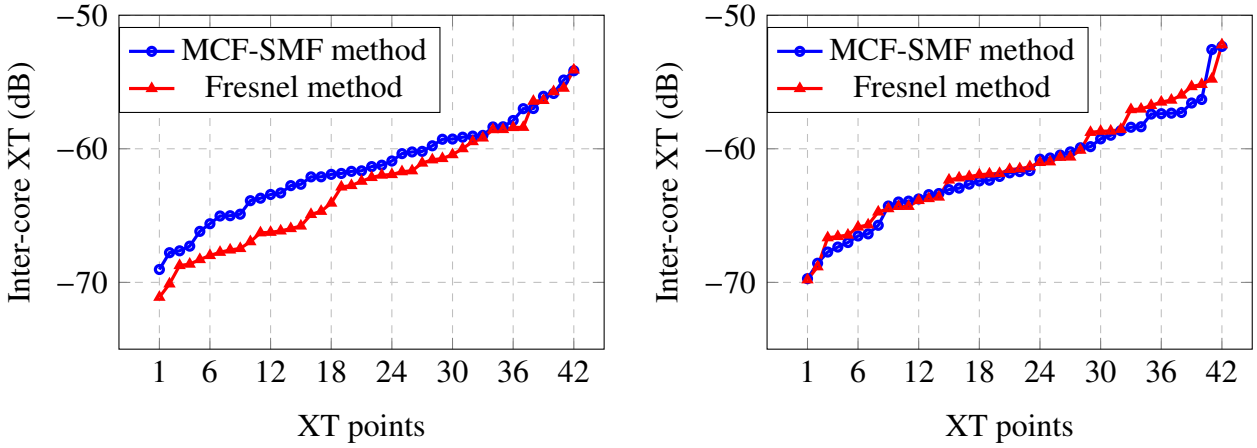

Figure 6.7: Sorted XT by the MCF-SMF coupling-based method and the Fresnel reflection-based method for (a) sample #1 and (b) sample #2.

As can be seen from the figures, the sorted XT obtained with these two methods shows very similar patterns for both samples. The correlation values between blue and red curves are 0.9852 and 0.9860 for sample #1 and #2, respectively. The corresponding box plots for results obtained by the two different methods are plotted in Figs. 6.8(a) and 6.8(b) for sample #1 and #2, respectively. For sample #1, the average XT is -61.40 dB and -62.86 dB with the MCF-SMF coupling-based method and the Fresnel reflection-based method, respectively. For sample #2, the corresponding XT is -61.55 dB and -61.21 dB with the MCF-SMF coupling-based method and the Fresnel reflection-based method, respectively.

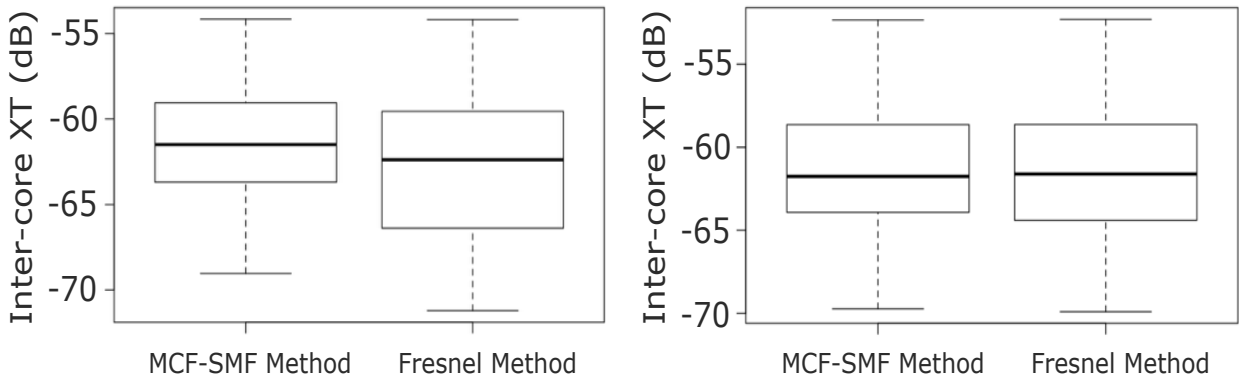

Figure 6.8: Box plots of XT in (a) sample #1 and (b) sample #2.

6.5 Summary

We have proposed a new method for XT characterization in MCF FI/FO devices based on Fresnel reflection at the glass-air interface. The new method has the advantages of being easier-to-adopt and much less time-consuming compared to the traditional core-to-core MCF-SMF coupling-based method. With this method, the XT in physical-contact-type MCF FI/FO devices were successfully measured. The XT results measured with the new method show similar statistical properties compared to the ones measured with the traditional MCF-SMF coupling method, confirming that the proposed method can be used reliably for XT measurements in MCF FI/FO devices.

□ End of chapter.

Chapter 7

Conclusion

7.1 Summary

Space-division multiplexing has been intensively researched in recent years to overcome the capacity limit of SMFs imposed by fiber nonlinearities, fiber fuse and the optical amplifier bandwidth. Among the different SDM schemes, we have investigated the one based on uncoupled MCFs, which is a simple and robust option compared to other schemes as it does not need any complex MIMO processing at the receiver side. In order to achieve uncoupled MCFs with low-XT, TA-MCFs are most widely used and they have been used in many state-of-the-art high-capacity transmission experiments. Although the traditional way of designing MCFs relies heavily on numerical simulations, it is desirable to develop an analytical model for XT in TA-MCFs in order to design low-XT, high-count MCFs more effectively by better understanding the relationships between XT and fiber structural parameters. In this direction, we successfully developed an analytical model for XT estimation in homogeneous TA-MCFs (Chapter 3), used the model for XT reduction by core positions movement (Chapter 4) and for high-count MCFs design with new core layout structures (Chapter 5), and finally proposed a novel method for XT measurements in MCF FI/FO devices (Chapter 6). The key results presented in the aforementioned chapters are summarized in the following sections and finally, an outlook on future research directions and issues in SDM systems are described.

7.1.1 Analytical model for XT in TA-MCFs

An analytical model for designing low-XT and high-count homogeneous TA-MCFs has been newly developed. The analytical model is beneficial not only for XT estimation but also for XT properties analysis. With this model, XT properties such as wavelength-dependent XT, XT reduction amount versus trench width, trench depth and XT dependence on core pitch in homogeneous TA-MCFs have been investigated. The possibility and practical limitations on further XT reduction in TA-MCFs were also studied. The developed model simplifies the designing of low-XT and high-count TA-MCFs for high-capacity and long-distance transmission.

7.1.2 Optimization of core positions

The analytical model for XT in TA-MCFs has been used successfully to search for new more optimum core layout structure for XT reduction in non close-packed core layout structures, achieving much lower XT without changing other fiber parameters. With the analytical model, we have found a new core layout structure with lower XT using core positions movement in homogeneous TA 12-core fibers with ORS and showed that DRS is a quasi-optimum core layout structure with its XT reduction of more than 14 dB compared to ORS.

7.1.3 High-count MCFs design

In order to achieve homogeneous TA-MCFs with high core density, it is also important to investigate core layout structures that can utilize the XT reduction benefits of PDI. It is found that square-lattice structure (SLS) is most suited for MCFs adopting PDI. We have designed square-lattice structured MCFs with a number of cores of 24 and 32 both in unidirectional and PDI transmission schemes. The worst XT at 1550 nm in the homogeneous 32-core fiber under PDI was higher than -30 dB over 100 km for 32QAM. Finally, we have designed a low-XT 32-core fiber by combining a heterogeneous core arrangement with two types of non-identical cores and PDI. We then concluded that if we are restricted to designing low-XT (-30 dB over 100 km) and high-count (more than 30 cores) MCFs adopting only unidirectional transmission scheme, heterogeneous core arrangements with 3 or even 4 types of cores are needed.

7.1.4 XT measurement method in MCF FI/FO devices

FI/FO devices are an essential component in MCF transmission systems, the their XT may limit the overall system performance. Thus, it is important that the XT properties in MCF FI/FO devices can be characterized precisely. We have investigated a novel XT measurement method in MCF FI/FO devices, which is based on Fresnel reflection at the MCF-to-air interface. The new method does not rely on the MCF-SMF coupling as opposed to the traditional method, and the measurement results are immune to the cleaving angle of the MCFs. Measurement results based on the traditional MCF-SMF coupling-based method and the Fresnel reflection-based method were compared, and it is found that they show very similar statistical properties. The new measurement method provides a simple and much less time-consuming platform for characterizing XT in MCF FI/FO devices.

7.2 Outlook

As a promising technology for overcoming the capacity limit of SMFs so as to meet the rapid Internet traffic growth, SDM has recently been investigated intensively. The ultimate goal of SDM is to achieve the highest capacity per fiber and network throughput in a cost-effective and energy-efficient manner. As described in this thesis, our approach of developing an analytical model for designing uncoupled MCFs is unique. Based on the model, we are able to calculate the XT in homogeneous TA-MCFs in a simple and accurate manner and to achieve high-count MCFs design both under unidirectional and PDI transmission schemes.

The number of cores needed for 10 Pbit/s per fiber transmission (100 times of the SMF capacity) should be at least 100. In order to achieve such high-count MCFs, further investigations should be needed. The maximum number of cores in a single-mode MCF is ultimately limited by such factors as the maximum cladding diameter due to mechanical reliability constraints, the minimum cladding thickness due to the bending loss on the outer cores, the minimum core pitch due to XT requirements for high order modulation formats, and the minimum effective area of each core to suppress the fiber nonlinear effects for long-distance transmission. Further improvements of core density or reduction in XT have to be achieved by some other techniques, for instance, adopting heterogeneous core arrangements instead of homogeneous ones at the cost of much more complex manufacturing processes, improving doping processes such that the trench depth in the TA structure can be further increased, or developing some other practical mode confinement methods.

□ End of chapter.

Bibliography

[1] R. W. Tkach, "Scaling Optical Communications for the Next Decade and Beyond," *Bell Labs Technical Journal*, vol. 14, no. 4, pp. 3–9, 2010.

[2] D. Qian, M.-F. Huang, E. Ip, Y.-K. Huang, Y. Shao, J. Hu, and T. Wang, "101.7-Tb/s (370×294-Gb/s) PDM-128QAM-OFDM Transmission over 3×55-km SSMF using Pilot-based Phase Noise Mitigation," in *Proc. OFC*, LA, California, USA, March 2011, paper PDPB5.

[3] A. Sano, T. Kobayashi, S. Yamanaka, A. Matsuura, H. Kawakami, Y. Miyamoto, K. Ishihara, and H. Masuda, "102.3-Tb/s (224×548-Gb/s) C- and Extended L-band All-Raman Transmission over 240 km using PDM-64QAM Single Carrier FDM with Digital Pilot Tone," in *Proc. OFC*, LA, California, USA, March 2012, paper PDP5C.3.

[4] A. D. Ellis, J. Zhao, and D. Cotter, "Approaching the Non-Linear Shannon Limit," *J. Lightwave Technol.*, vol. 28, no. 4, pp. 423–433, Feb. 2010.

[5] R. Essiambre, G. Kramer, P. Winzer, G. Foschini, and B. Goebel, "Capacity Limits of Optical Fiber Networks," *J. Lightwave Technol.*, vol. 28, no. 4, pp. 662–701, Feb. 2010.

[6] R. Essiambre and R. W. Tkach, "Capacity Trends and Limits of Optical Communication Networks," *Proc. IEEE*, vol. 100, no. 5, pp. 1035–1055, May 2012.

[7] R. Essiambre and A. Mecozzi, "Capacity Limits in Single-Mode Fiber and Scaling for Spatial Multiplexing," in *Proc. OFC*, LA, California, USA, March 2012, paper OW3D.1.

[8] K. Seo, N. Nishimura, M. Shiino, R. Yuguchi, and H. Sasaki, "Evaluation of High-power Endurance in Optical Fiber Links," *Furukawa Review*, no. 24, pp. 17–22, 2003.

[9] R. Kashyap, "History and Progress of the Fiber Fuse," in *Proc. OECC*, Busan, South Korea, July 2012, paper 6C4-1.

[10] K. Kurokawa, "Optical Fiber for High-Power Optical Communication," *Crystals*, vol. 2, no. 4, pp. 1382–1392, Sept. 2012.

[11] T. Morioka, "New Generation Optical Infrastructure Technologies: "EXAT Initiative" Towards 2020 and Beyond," in *Proc. OECC*, Hong Kong, July 2009, paper FT4.

[12] T. Morioka, Y. Awaji, R. Ryf, P. Winzer, D. Richardson, and F. Poletti, "Enhancing Optical Communications with Brand New Fibers," *IEEE Commun. Mag.*, vol. 50, no. 2, pp. S31–S42, Feb. 2012.

[13] F. Yaman, N. Bai, B. Zhu, T. Wang, and G. Li, "Long Distance Transmission in Few-mode Fibers," *Opt. Express*, vol. 18, no. 12, pp. 13 250–13 257, June 2010.

[14] F. Yaman, N. Bai, Y. K. Huang, M. F. Huang, B. Zhu, T. Wang, and G. Li, "10×112Gb/s PDM-QPSK Transmission over 5032 km in Few-Mode Fibers," *Opt. Express*, vol. 18, no. 20, pp. 21 342–21 349, Sept. 2010.

[15] H.-S. Chen, A. Koonen, B. Corbett, R. Winfield, and H. van den Boom, "20 Gbit/s Two LP11 Modes Transmission over 10 km Two-moded Fiber without Crosstalk Compensation," in *Proc. OECC*, Busan, South Korea, July 2012, paper 6B2-1.

[16] N. Hanzawa, K. Saitoh, T. Sakamoto, T. Matsui, S. Tomita, and M. Koshiba, "Demonstration of Mode-Division Multiplexing Transmission over 10 km Two-mode Fiber with Mode Coupler," in *Proc. OFC*, LA, California, USA, March 2011, paper OWA4.

[17] P. Sillard, M. Bigot-Astruc, D. Boivin, H. Maerten, and L. Provost, "Few-mode Fiber for Uncoupled Mode-Division Multiplexing Transmissions," in *Proc. ECOC*, Geneva, Switzerland, Sept. 2011, paper Tu.5.LeCervin.7.

[18] R. Ryf, S. Randel, A. H. Gnauck, C. Bolle, A. Sierra, S. Mumtaz, M. Esmaeelpour, E. C. Burrows, R.-J. Essiambre, P. J. Winzer, D. W. Peckham, A. H. McCurdy, and R. Lingle, "Mode-Division Multiplexing over 96 km of Few-Mode Fiber using Coherent 6×6 MIMO Processing," *J. Lightwave Technol.*, vol. 30, no. 4, pp. 521–531, Feb. 2012.

[19] E. Ip, N. Bai, Y.-K. Huang, E. Mateo, F. Yaman, M.-J. Li, S. Bickham, S. Ten, J. Linares, C. Montero, V. Moreno, X. Prieto, Y. Luo, G.-D. Peng, G. Li, and T. Wang, "6 × 6 MIMO Transmission over 50+25+10 km Heterogeneous Spans of Few-Mode Fiber with Inline Erbium-doped Fiber Amplifier," in *Proc. OFC*, LA, California, USA, March 2012, paper OTu2C.4.

[20] V. Sleiffer, Y. Jung, B. Inan, H. Chen, R. van Uden, M. Kuschnerov, D. van den Borne, S. Jansen, V. Veljanovski, T. Koonen, D. Richardson, S. ul Alam, F. Poletti, J. Sahu, A. Dhar, B. Corbett, R. Winfield, A. Ellis, and H. D. Waardt, "Mode-Division-Multiplexed 3 × 112-Gb/s DP-QPSK Transmission over 80 km Few-mode Fiber with Inline MM-EDFA and Blind DSP," in *Proc. ECOC*, Amsterdam, Netherlands, Sept. 2012, paper Tu.1.C.2.

[21] C. Koebele, M. Salsi, L. Milord, R. Ryf, C. Bolle, P. Sillard, S. Bigo, and G. Charlet, "40 km Transmission of Five Mode Division Multiplexed Data Streams at 100 Gb/s with low MIMO-DSP Complexity," in *Proc. ECOC*, Geneva, Switzerland, Sept. 2011, paper Th.13.C.3.

[22] N. K. Fontaine, R. Ryf, H. Chen, A. V. Benitez, B. Guan, R. Scott, B. Ercan, S. J. B. Yoo, L. E. Grüner-Nielsen, Y. Sun, R. Lingle, E. Antonio-Lopez, and R. Amezcua-Correa, "30×30 MIMO Transmission over 15 Spatial Modes," in *Proc. OFC*, LA, California, USA, March 2015, paper Th5C.1.

[23] R. Ryf, H. Chen, N. K. Fontaine, A. M. V. azquez Bentez, J. Antonio-Lopez, C. Jin, B. Huang, M. Bigot-Astruc, D. Molin, F. Achten, P. Sillard, and R. Amezcua-Correa, "10-Mode Mode-Multiplexed Transmission over 125-km Single-Span Multimode Fiber," in *Proc. ECOC*, Valencia, Spain, Sept. 2015, paper PDP.3.3.

[24] C. Xia, N. Bai, I. Ozdur, X. Zhou, and G. Li, "Supermodes for Optical Transmission," *Opt. Express*, vol. 19, no. 17, pp. 16 653–16 664, Aug. 2011.

[25] R. Ryf, A. Sierra, R.-J. Essiambre, A. Gnauck, S. Randel, M. Esmaeelpour, S. Mumtaz, P. J. Winzer, R. Delbue, P. Pupalaikis, A. Sureka, T. Hayashi, T. Taru, and T. Sasaki, "Coherent 1200-km 6 × 6 MIMO Mode-Multiplexed Transmission over 3-core Microstructured Fiber," in *Proc. ECOC*, Geneva, Switzerland, Sept. 2011, paper Th.13.C.1.

[26] R. Ryf, R. Essiambre, S. Randel, A. Gnauck, P. Winzer, T. Hayashi, T. Taru, and T. Sasaki, "MIMO-Based Crosstalk Suppression in Spatially Multiplexed 3×56-Gb/s PDM-QPSK Sig-

nals for Strongly Coupled Three-Core Fiber," *IEEE Photon. Technol. Lett.*, vol. 23, no. 20, pp. 1469 –1471, Oct. 2011.

[27] T. Hayashi, R. Ryf, N. K. Fontaine, C. Xia, S. Randel, R.-J. Essiambre, P. J. Winzer, and T. Sasaki, "Coupled-Core Multi-Core Fibers: High-Spatial-Density Optical Transmission Fibers with Low Differential Modal Properties," in *Proc. ECOC*, Valencia, Spain, Sept. 2015, paper We.1.4.1.

[28] M. Koshiba, K. Saitoh, and Y. Kokubun, "Heterogeneous Multi-Core Fibers: Proposal and Design Principle," *IEICE Electron. Express.*, vol. 6, no. 2, pp. 98–103, 2009.

[29] K. Imamura, K. Mukasa, and T. Yagi, "Effective Space Division Multiplexing by Multi-Core Fibers," in *Proc. ECOC*, Torino, Italy, Sept. 2010, paper P1.09.

[30] M. Koshiba, "Recent Progress in Multi-Core Fibers for Ultralarge-Capacity Transmission," in *Proc. OECC*, Sapporo, Japan, July 2010, paper 6B1-3.

[31] K. Takenaga, Y. Arakawa, S. Tanigawa, N. Guan, S. Matsuo, K. Saitoh, and M. Koshiba, "Reduction of Crosstalk by Trench-Assisted Multi-Core Fiber," in *Proc. OFC*, LA, California, USA, March 2011, paper OWJ4.

[32] B. Zhu, T. Taunay, M. Fishteyn, X. Liu, S. Chandrasekhar, M. F. Yan, J. M. Fini, E. M. Monberg, and F. V. Dimarcello, "112-Tb/s Space-Division Multiplexed DWDM Transmission with 14-b/s/Hz Aggregate Spectral Efficiency over a 76.8-km Seven-core Fiber," *Opt. Express*, vol. 19, no. 17, pp. 16 665–16 671, Aug. 2011.

[33] S. Matsuo, K. Takenaga, Y. Arakawa, Y. Sasaki, S. Taniagwa, K. Saitoh, and M. Koshiba, "Large-effective-area Ten-core Fiber with Cladding Diameter of about 200μm," *Opt. Lett.*, vol. 36, no. 23, pp. 4626–4628, Dec. 2011.

[34] K. Takenaga, Y. Arakawa, Y. Sasaki, S. Tanigawa, S. Matsuo, K. Saitoh, and M. Koshiba, "A Large Effective Area Multi-Core Fibre with an Optimised Cladding Thickness," in *Proc. ECOC*, Geneva, Switzerland, Sept. 2011, paper Mo.1.LeCervin.2.

[35] S. Yamamoto, M. Ohashi, and Y. Miyoshi, "Crosstalk in Multi-Core Fibers with α-Index Single-Mode Cores," in *Proc. OECC*, Busan, South Korea, July 2012, paper P1-24.

[36] T. Hayashi, T. Taru, O. Shimakawa, T. Sasaki, and E. Sasaoka, "Low-Loss and Large-A_{eff} Multi-Core Fiber for SNR Enhancement," in *Proc. ECOC*, Amsterdam, Netherlands, Sept. 2012, paper Mo.1.F.3.

[37] J. Tu, K. Saitoh, M. Koshiba, K. Takenaga, and S. Matsuo, "Large-effective-area Heterogeneous Trench-Assisted Twelve-core Fiber under Bending Condition," in *Proc. OECC*, Busan, South Korea, July 2012, paper 5C1-3.

[38] K. Imamura and R. Sugizaki, "Recent Advances in Multi-Core Transmission Fibers," in *Proc. OECC*, Busan, South Korea, July 2012, paper 5E3-2.

[39] M. Nakazawa, "Extremely Advanced Transmission with 3M Technologies (Multi-level Modulation, Multi-core & Multi-mode)," in *Proc. OFC*, LA, California, USA, March 2012, paper OTu1D.1.

[40] J. Sakaguchi, B. J. Puttnam, W. Klaus, Y. Awaji, N. Wada, A. Kanno, T. Kawanishi, K. Imamura, H. Inaba, K. Mukasa, R. Sugizaki, T. Kobayashi, and M. Watanabe, "19-core Fiber Transmission of $19\times100\times172$-Gb/s SDM-WDM-PDM-QPSK Signals at 305 Tb/s," in *Proc. OFC*, LA, California, USA, March 2012, paper PDP5C.1.

[41] S. Matsuo, Y. Sasaki, I. Ishida, K. Takenaga, K. Saitoh, and M. Koshiba, "Recent Progress on Multi-Core Fiber and Few-Mode Fiber," in *Proc. OFC*, Anaheim, California, USA, March 2013, paper OM3I.3.

[42] J. Sakaguchi, B. J. Puttnam, W. Klaus, Y. Awaji, N. Wada, A. Kanno, T. Kawanishi, K. Imamura, H. Inaba, K. Mukasa, R. Sugizaki, T. Kobayashi, and M. Watanabe, "305 Tb/s Space Division Multiplexed Transmission using Homogeneous 19-Core Fiber," *J. Lightwave Technol.*, vol. 31, no. 4, pp. 554–562, Feb. 2013.

[43] S. Matsuo, Y. Sasaki, T. Akamatsu, I. Ishida, K. Takenaga, K. Okuyama, K. Saitoh, and M. Kosihba, "12-core Fiber with One Ring Structure for Extremely Large Capacity Transmission," *Opt. Express*, vol. 20, no. 27, pp. 28 398–28 408, Dec. 2012.

[44] H. Takara, A. Sano, T. Kobayashi, H. Kubota, H. Kawakami, A. Matsuura, Y. Miyamoto, Y. Abe, H. Ono, K. Shikama, Y. Goto, K. Tsujikawa, Y. Sasaki, I. Ishida, K. Takenaga, S. Matsuo, K. Saitoh, M. Koshiba, and T. Morioka, "1.01-Pb/s (12 SDM/222 WDM/456

Gb/s) Crosstalk-managed Transmission with 91.4-b/s/Hz Aggregate Spectral Efficiency," in *Proc. ECOC*, Amsterdam, Netherlands, Sept. 2012, paper Th.3.C.1.

[45] T. Hayashi, T. Sasaki, and E. Sasaoka, "Multi-Core Fibers for High Capacity Transmission," in *Proc. OFC*, LA, California, USA, March 2012, paper OTu1D.4.

[46] F. Ye, C. Peucheret, and T. Morioka, "Capacity of Space-Division Multiplexing with Heterogeneous Multi-Core Fibers," in *Proc. OECC/PS*, Kyoto, Japan, July 2013, paper WR2-3.

[47] B. J. Puttnam, R. S. Luís, W. Klaus, J. Sakaguchi, J.-M. D. Mendinueta, Y. Awaji, N. Wada, Y. Tamura, T. Hayashi, M. Hirano, and J. Marciante, "2.15 Pb/s Transmission Using a 22 Core Homogeneous Single-Mode Multi-Core Fiber and Wideband Optical Comb," in *Proc. ECOC*, Valencia, Spain, Sept. 2015, paper PDP.3.1.

[48] C. E. Shannon, "A Mathematical Theory of Communication," *Bell System Technical Journal*, vol. 27, pp. 379–423 & 623–656, July & October 1948.

[49] F. Ye, S. Warm, and K. Petermann, "Differential Mode Delay Management in Spliced Multimode Fiber Transmission Systems," in *Proc. OFC*, Anaheim, California, USA, March 2013, paper OM3B.3.

[50] T. Sakamoto, T. Mori, T. Yamamoto, and S. Tomita, "Differential Mode Delay Managed Transmission Line for WDM-MIMO System using Multi-Step Index Fiber," *J. Lightwave Technol.*, vol. 30, no. 17, pp. 2783–2787, Sept. 2012.

[51] P. J. Winzer, A. H. Gnauck, A. Konczykowska, F. Jorge, and J.-Y. Dupuy, "Penalties from In-Band Crosstalk for Advanced Optical Modulation Formats," in *Proc. ECOC*, Geneva, Switzerland, Sept. 2011, paper Tu.5.B.7.

[52] Y. Sasaki, S. Saitoh, Y. Amma, K. Takenaga, S. Matsuo, K. Saitoh, T. Morioka, and Y. Miyamoto, "Quasi-Single-Mode Homogeneous 31-Core Fibre," in *Proc. ECOC*, Valencia, Spain, Sept. 2015, paper We.1.4.4.

[53] J. Sakaguchi, W. Klaus, J.-M. D. Mendinueta, B. Puttnam, R. Luis, Y. Awaji, N. Wada, T. Hayashi, T. Nakanishi, T. Watanabe, Y. Kokubun, T. Takahata, and T. Kobayashi, "Realizing a 36-core, 3-mode Fiber with 108 Spatial Channels," in *Proc. OFC*, LA, California, USA, March 2015, paper Th5C.2.

[54] K. Igarashi, D. Souma, Y. Wakayama, K. Takeshima, Y. Kawaguchi, T. Tsuritani, I. Morita, and M. Suzuki, "114 Space-Division-Multiplexed Transmission over 9.8-km Weakly-Coupled-6-Mode Uncoupled-19-Core Fibers," in *Proc. OFC*, LA, California, USA, March 2015, paper Th5C.4.

[55] K. Okamoto, *Fundamentals of Optical Waveguides*, 2nd ed. Academic Press, 2006.

[56] M. Koshiba, K. Saitoh, K. Takenaga, and S. Matsuo, "Analytical Expression of Average Power-Coupling Coefficients for Estimating Intercore Crosstalk in Multicore Fibers," *IEEE Photonics Journal*, vol. 4, no. 5, pp. 1987–1995, Oct. 2012.

[57] K. Saitoh, T. Matsui, T. Sakamoto, M. Koshiba, and S. Tomita, "Multi-Core Hole-Assisted Fibers for High Core Density Space Division Multiplexing," in *Proc. OECC*, Sapporo, Japan, July 2010, paper 7C2-1.

[58] K. Imamura, K. Mukasa, R. Sugizaki, Y. Mimura, and T. Yagi, "Multi-Core Holey Fibers for Ultra Large Capacity Wide-band Transmission," in *Proc. ECOC*, Brussels, Belgium, Sept. 2008, paper P.1.17.

[59] B. Yao, K. Ohsono, N. Shiina, K. Fukuzato, A. Hongo, E. H. Sekiya, and K. Saito, "Reduction of Crosstalk by Hole-Walled Multi-Core Fibers," in *Proc. OFC*, LA, California, USA, March 2012, paper OM2D.5.

[60] S. Matsuo, M. Ikeda, and K. Himeno, "Bend-insensitive and Low-splice-loss Optical Fiber for Indoor Wiring in FTTH," in *Proc. OFC*, LA, California, USA, March 2004, paper ThI3.

[61] T. Ito, E. L. T. de Gabory, M. Arikawa, Y. Hashimoto, and K. Fukuchi, "Reduction of Influence of Inter-core Cross-talk in MCF with Bidirectional Assignment between Neighboring Cores," in *Proc. OFC*, Anaheim, California, USA, March 2013, paper OTh3K.2.

[62] A. Sano, H. Takara, T. Kobayashi, H. Kawakami, H. Kishikawa, T. Nakagawa, Y. Miyamoto, Y. Abe, H. Ono, K. Shikama, M. Nagatani, T. Mori, Y. Sasaki, I. Ishida, K. Takenaga, S. Matsuo, K. Saitoh, M. Koshiba, M. Yamada, H. Masuda, and T. Morioka, "409-Tb/s + 409-Tb/s Crosstalk Suppressed Bidirectional MCF Transmission over 450 km using Propagation-direction Interleaving," *Opt. Express*, vol. 21, no. 14, pp. 16 777–16 783, July 2013.

[63] A.Sano, H.Takara, T.Kobayashi, and Y.Miyamoto, "Crosstalk-managed High Capacity Long Haul Multicore Fiber Transmission with Propagation-Direction Interleaving," *J. Lightwave Technol.*, vol. 32, no. 16, pp. 2771–2779, 2014.

[64] P. Gysel and R. K. Staubli, "Statistical Properties of Rayleigh Backscattering in Single-Mode Fibers," *J. Lightwave Technol.*, vol. 8, no. 4, pp. 561–567, April 1990.

[65] E. Brinkmeyer, "Backscattering in Single-Mode Fibres," *Electron. Lett.*, vol. 16, no. 9, pp. 329–330, April 1980.

[66] T. Kobayashi, H. Takara, A. Sano, T. Mizuno, H. Kawakami, Y. Miyamoto, K. Hiraga, Y. Abe, H. Ono, M. Wada, Y. Sasaki, I. Ishida, K. Takenaga, S. Matsuo, K. Saitoh, M. Yamada, H. Masuda, and T. Morioka, "2 × 344 Tb/s Propagation-direction Interleaved Transmission over 1500-km MCF Enhanced by Multicarrier Full Electric-field Digital Back-propagation," in *Proc. ECOC*, London, UK, Sept. 2013, paper PD3.E.4.

[67] J. Tu, K. Saitoh, M. Koshiba, K. Takenaga, and S. Matsuo, "Design and Analysis of Large-effective-area Heterogeneous Trench-Assisted Multi-Core Fiber," *Opt. Express*, vol. 20, no. 14, pp. 15 157–15 170, July 2012.

[68] ——, "Optimized Design Method for Bend-insensitive Heterogeneous Trench-Assisted Multi-Core Fiber with Ultra-low Crosstalk and High Core Density," *J. Lightwave Technol.*, vol. 31, no. 15, pp. 2590–2598, Aug. 2013.

[69] ——, "Optimized Design Method for Heterogeneous Trench-Assisted Multi-Core Fiber," in *Proc. OECC*, Kyoto, Japan, July 2013, paper MS1-5.

[70] A. Snyder and J. D. Love, *Optical Waveguide Theory*, 1st ed. Springer, 1983, no. P. 317.

[71] F. Ye, J. Tu, K. Saitoh, K. Takenaga, S. Matsuo, and T. Morioka, "A New and Simple Method for Crosstalk Estimation in Homogeneous Trench-Assisted Multi-Core Fibers," in *Proc. ACP*, Shanghai, China, Nov. 2014, paper AW4C.3.

[72] T. Hayashi, T. Nagashima, O. Shimakawa, T. Sasaki, and E. Sasaoka, "Crosstalk Variation of Multi-Core Fibre due to Fibre Bend," in *Proc. ECOC*, Torino, Italy, Sept. 2010, paper We.8.F.6.

[73] F. Ye, J. Tu, K. Saitoh, H. Takara, and T. Morioka, "Wavelength-dependent Crosstalk in Trench-Assisted Multi-Core Fibers," in *Proc. OECC/ACOFT*, Melbourne, Australia, July 2014, paper TU5C-1.

[74] F. Ye, J. Tu, K. Saitoh, K. Takenaga, S. Matsuo, H. Takara, and T. Morioka, "Wavelength-dependence of Inter-core Crosstalk in Homogeneous Multi-Core Fibers," *IEEE Photon. Technol. Lett.*, vol. 28, no. 1, pp. 27–30, Jan. 2016.

[75] F. Ye, J. Tu, K. Saitoh, and T. Morioka, "Simple Analytical Expression for Crosstalk Estimation in Homogeneous Trench-Assisted Multi-Core Fibers," *Opt. Express*, vol. 22, no. 19, pp. 23 007–23 018, Sept. 2014.

[76] M.-J. Li, P. Tandon, D. C. Bookbinder, S. R. Bickham, M. A. McDermott, R. B. Desorcie, D. A. Nolan, J. J. Johnson, K. A. Lewis, and J. J. Englebert, "Ultra-low Bending Loss Single-Mode Fiber for FTTH," in *Proc. OFC*, March 2008, paper PDP10.

[77] F. Ye, J. Tu, K. Saitoh, and T. Morioka, "Theoretical Investigation of Inter-core Crosstalk Properties in Homogeneous Trench-Assisted Multi-Core Fibers," in *IEEE Photonics Society Summer Topicals Meeting Series*, Montreal, Canada, July 2014, paper TuE4.2.

[78] T. Hayashi, T. Taru, O. Shimakawa, T. Sasaki, and E. Sasaoka, "Low-crosstalk and Low-loss Multi-Core Fiber utilizing Fiber Bend," in *Proc. OFC*, LA, California, USA, March 2011, paper OWJ3.

[79] ——, "Design and Fabrication of Ultra-low Crosstalk and Low-loss Multi-Core Fiber," *Opt. Express*, vol. 19, no. 17, pp. 16 576–16 592, Aug. 2011.

[80] Y. Amma, Y. Sasaki, K. Takenaga, S. Matsuo, J. Tu, K. Saitoh, M. Koshiba, T. Morioka, and Y. Miyamoto, "High-density Multicore Fiber with Heterogeneous Core Arrangement," in *Proc. OFC*, LA, California, USA, March 2015, paper Th4C.4.

[81] R. Graham, B. Lubachevsky, K. Nurmela, and P. Ostergard, "Dense Packings of Congruent Circles in a Circle," *Discrete Mathematics*, vol. 181, pp. 139–154, 1998.

[82] F. Fodor, "The Densest Packing of 12 Congruent Circles in a Circle," *Contributions to Algebra and Geometry*, vol. 41, no. 2, pp. 401–409, 2000.

[83] S. Kravitz, "Packing Cylinders into Cylindrical Containers," *Mathematics Magazine*, vol. 40, no. 2, pp. 65–71, 1967.

[84] F. Ye and T. Morioka, "Interleaved Core Assignment for Bidirectional Transmission in Multi-Core Fibers," in *Proc. ECOC*, London, UK, Sept. 2013, paper We.2.D.5.

[85] M. Koshiba, K. Saitoh, K. Takenaga, and S. Matsuo, "Multi-Core Fiber Design and Analysis: Coupled-Mode Theory and Coupled-Power Theory," *Opt. Express*, vol. 19, no. 26, pp. B102–B111, Dec. 2011.

[86] W. Klaus, J. Sakaguchi, B. Puttnam, Y. Awaji, N. Wada, T. Kobayashi, and M. Watanabe, "Free-Space Coupling Optics for Multicore Fibers," *IEEE Photon. Technol. Lett.*, vol. 24, no. 21, pp. 1902–1905, Nov. 2012.

[87] T. Watanabe, M. Hikita, and Y. Kokubun, "Laminated Polymer Waveguide Fan-Out Device for Uncoupled Multi-Core Fibers," *Opt. Express*, vol. 20, no. 24, pp. 26 317–26 325, Nov. 2012.

[88] Y. Abe, K. Shikama, S. Yanagi, and T. Takahashi, "Physical-contact-type Fan-Out Device for Multicore Fibre," *Electron. Lett.*, vol. 49, no. 11, pp. 711–712, 2013.

[89] K. Takenaga, Y. Arakawa, S. Tanigawa, N. Guan, S. Matsuo, K. Saitoh, and M. Koshiba, "An Investigation on Crosstalk in Multi-Core Fibers by Introducing Random Fluctuation along Longitudinal Direction," *IEICE TRANSACTIONS on Communications*, vol. E94-B, no. 2, pp. 409–416, 2011.

[90] T. Hayashi, T. Taru, O. Shimakawa, T. Sasaki, and E. Sasaoka, "Characterization of Crosstalk in Ultra-Low-Crosstalk Multi-Core Fiber," *J. Lightwave Technol.*, vol. 30, no. 4, pp. 583–589, Feb 2012.